Imaging of vertical seismic profiling data using the common-reflection-surface stack

---

Abbildungsverfahren für seismische Daten aus Bohrlochmessungen mit der Common-Reflection-Surface Stapelung

Zur Erlangung des akademischen Grades eines

DOKTORS DER NATURWISSENSCHAFTEN

von der Fakultät für Physik der Universität(TH) Karlsruhe

genehmigte

DISSERTATION

von

Dipl.-Geophys. Markus von Steht

aus Rastatt

Tag der mündlichen Prüfung:	15. Februar 2008
Referent:	Prof. Dr. Peter Hubral
Korreferent:	Prof. Dr. Dirk Gajewski

Zusammenfassung

Vorbemerkung

Diese Dissertation wurde bis auf die folgende Zusammenfassung in Englisch verfasst. Da auch in der deutschen Sprache einige englische Fachausdrücke gebräuchlich sind, wurde bei diesen Ausdrücken auf eine Übersetzung verzichtet. Sie werden, mit Ausnahme ihrer groß geschriebenen Abkürzungen, *kursiv* dargestellt. Für die deutschsprachige Zusammenfassung wurde der gleiche Aufbau gewählt, wie er auch im Hauptteil der Arbeit verwendet wird.

Einleitung

Die Zielsetzungen bei der Aufzeichnung von seismischen Daten sind das Erstellen von strukturellen Abbildern des Untergrundes und die Bestimmung von zugehörigen Materialparametern, um damit Rückschlüsse auf seine geologische Zusammensetzung ziehen zu können. Wenn man die Problemstellung der Bilderzeugung hinsichtlich ihrer Herausforderungen betrachtet, sieht man sich mit zum Teil komplizierten und umfangreichen Berechnungen konfrontiert. Darüber hinaus sorgt die weitgehend-eingeschränkte Messkonfiguration häufig dafür, dass eine inverse, mathematisch-inkorrekte Problemstellung (*Ill-Posed Problem*) vorliegt. Deshalb haben sich Wissenschaftler schon immer um neue Möglichkeiten zur Beschleunigung und Stabilisierung von Abbildungsverfahrens bemüht.

In meiner Dissertation beschäftige ich mich mit der Entwicklung eines automatisierten, datenorientierten Abbildungsverfahrens, das auf der sogenannten *Common-Reflection-Surface* (CRS) Stapelung basiert. Ein prinzipieller Vorteil, den die CRS Stapelung gegenüber anderen Methoden hat, liegt in der Ausnutzung der Redundanz welche sich in den Messdaten findet. Durch die Miteinbeziehung von benachbarten Experimenten bei der Simulation eines Einzelexperiments während der Kohärenzanalyse und dem anschließenden Stapelvorgang kommt dies zum tragen. Dadurch besitzen Ergebnisse, die mit dieser Methode synthetisiert wurden, ein stark verbessertes Signal-zu-Rauschen Verhältnis und sind in der Regel deutlich von Mehrdeutigkeiten bereinigt.

Ein weiterer Hauptaugenmerk der Arbeit liegt bei der Anpassung des Verfahrens an die Verarbeitung von Messdaten, wie sie gewöhnlich in Bohrlöchern akquiriert werden, wobei seismischen Quellen an der Oberfläche verbleiben. Solche *Vertical Seismic Profiling* (VSP) Messungen sind ein recht altes Verfahren, das im Laufe der letzten Jahre - begünstigt durch erhebliche Fortschritte in der Instrumententechnik - ein Wiederaufleben erfahren hat. Daten aus VSP Messungen besitzen eine sehr viel höhere Auflösung und Qualität als jene, die man durch konventionellen Oberflächenseismik erhält. Zusätzlich werden bei VSP Messungen, durch die ausgezeichnete Koppelung der Geophone an die Bohrlochwand, in der Regel alle drei Komponenten der Bodenbewegung aufgezeichnet. Somit können unterschiedliche Typen von seismischen Wellen

verhältnismäßig einfach identifiziert und extrahiert werden. Die Erzeugung von individuellen Abbildern des Untergrundes basierend auf Kompressions- und Scherwellen wird vereinfacht.

Theorie

Nach kurzen Einführungen in Kontinuumsmechanik und Wellentheorie leite ich in die Eikonal- und Transportgleichung her, die auf den Annahmen getroffen in der *Zero-Order Ray-Theory* basieren. Daran anknüpfend wird das paraxiale *Raytracing* System, welches eine mögliche Lösung der Eikonalgleichung darstellt, in verschiedenen Koordinatensystemen aufgestellt. Nachdem ich die *Ray-Propagator Matrix* und das Zwei-Punkt Eikonal eingeführt habe, werde ich eine allgemeine Laufzeitapproximation zweiter Ordnung für die Wellenausbreitung in drei Dimensionen aufstellen. Deren Parametrisierung durch eine *Common-Offset* CRS Summationsfläche gründet sich auf die Annahme eines isotropen, lateral-inhomogenen Modells mit gekrümmten Schichtgrenzen. Ferner bleibt die Quell-Empfängerkonfiguration hinsichtlich der simulierten Zentralstrahlen in diesem Fall frei wählbar, damit bistatische Experimente - wie es beispielsweise VSP Messung sind - überhaupt handhabbar werden.
Zur theoretischen Grundlage der Strahlentheorie verweise ich auf das Buch von Červený (2001). Bezüglich einiger Grundlagen zur CRS Stapelung verweise ich auf die Arbeiten von Mann (2002), Zhang (2003) und Boelsen (2005).

CRS Operatoren und Implementation

Es schließt sich eine Dikussion einiger angepasster Formen von CRS Operatoren für einige VSP Messgeometrien an. Zusätzlich werden die sogenannten kinematischen Wellenfeldattribute eingeführt, die für die Extrapolation des paraxialen *Slowness* Vektors während der Wellenfeldseparation benötigt werden. Nach einer Beschränkung auf ein 2.5-dimensionales Modell des Untergrundes, wird der von mir entwickelte Arbeitsablauf zur Bestimmung von CRS Laufzeitflächen aus Messdaten vorgestellt. Außerdem wird auf die Vorgehensweise zur Auftrennung in individuelle Wellenfelder im Fall von Mehrkomponentendaten eingegangen.

Datenbeispiele

Anhand dreier Datenbeispiele werden verschiedene Aspekte der Methode vorgestellt und das Zusammenspiel der zahlreichen Einzelschritte bis zum fertigen Tiefenabbild illustriert. Ein verhältnismäßig einfaches synthetisches Beispiel für ein senkrechtes Bohrloch verifiziert die Verlässlichkeit und Stabilität der Methode bereits ausgezeichnet. Ein Realdatensatz, auf dem das erste Beispiel aufbaute, liefert ebenso bestätigende Ergebnisse unter realistischen Bedingungen. Ein dritter synthetischer Datensatz für ein - mit zunehmender Tiefe - abgelenktes Bohrloch weist auf die Anpassungsfähigkeit der Methode hin.

Neue Forschungsrichtungen

In einem weiterführenden Kapitel möchte ich auf vielversprechende Erkenntnisse und mögliche neue Forschungsschwerpunkte hinweisen, die sich im Laufe der Arbeit hauptsächlich aus Zeitgründen nicht genauer verfolgen ließen. Unter anderem liefert das entwickelte Abbildungsverfahren für konventionelle Messdaten der Landseismik, die unter dem Einfluss einer irregulären oder unebenen Messoberfläche akquiriert wurden, sehr brauchbare erste Ergebnisse. Ein weiterer, künftiger Ansatzpunkt könnte die Konversion von VSP Daten in Oberflächendaten mithilfe von Wellenfeldattributen sein.

Schlussfolgerungen

Insgesamt kann die Arbeit als erfolgreicher erster Schritt in ein Spezialgebiet der angewandten Seismik gewertet werden. Der große Umfang der angeschnittenen Themengebiete ließ eine systematische Untersuchung einiger Aspekte - u.a. physikalische Normierung der Aperturgröße, Suchbereichskontrolle, neue Einsatzgebiete der Wellenfeldattribute - leider nicht zu.
Die entwickelte Methode ist sehr anpassungsfähig und liefert im Vergleich mit konventionellen Abbildungsverfahren Ergebnisse von ähnlicher Qualität und Aussagekraft. Darüber hinaus ist sie weniger anfällig für Mehrdeutigkeiten, wie sie sich gewöhnlich aus Fehlern in *a priori* angenommenen Geschwindigkeitsmodellen ergeben, und kann bei Mehrkomponentendaten als unterstützendes Hilfsmittel zur Auftrennung in individuelle Wellenfelder eingesetzt werden.

Contents

1 Introduction **1**

1.1 Seismic data acquisition 1

1.2 Kirchhoff depth migration 2

1.3 Vertical seismic profiling geometries 4

1.4 Structure of the thesis 7

2 Theory **9**

2.1 Linear elastodynamics 10

2.2 The elastodynamic equation for heterogeneous isotropic media 11

2.2.1 High-frequency ansatz for wave propagation 11

2.2.2 The eikonal equation and its eigenvalue problem 13

2.2.3 The Hamiltonian and its characteristic equations 14

2.3 Dynamic ray tracing by means of paraxial rays 14

2.3.1 Paraxial ray tracing 15

2.3.2 The ray propagator matrix 16

2.3.3 Dynamic ray tracing 17

2.4 Ray tracing in ray-centered coordinates 17

2.4.1 Definition of ray-centered coordinates 18

2.4.2 Ray tracing system in ray-centered coordinates 19
2.4.3 Paraxial ray tracing in ray-centered coordinates 19
2.4.4 Dynamic ray tracing in ray-centered coordinates 20
2.4.5 Ray propagator matrix in ray-centered coordinates 20
2.4.6 The second derivative of traveltime in ray-centered coordinates 22
2.4.7 Continuation relations and wavefront experiments 22
2.5 Calculation of paraxial traveltimes 24
2.5.1 Paraxial traveltimes in ray-centered coordinates 25
2.5.2 Transformation to local ray-centered Cartesian coordinates 26
2.5.3 Paraxial traveltimes in local ray-centered Cartesian coordinates 28
2.5.4 Paraxial slowness vector 28
2.5.5 Two-point eikonal equation 29
2.6 Transformation to general Cartesian coordinates 31

3 Implementation 35

3.1 Introduction 35
3.2 Examples of CRS operators for VSP surveys 38
3.2.1 3D CO CRS operator for deviated wells 39
3.2.2 3D CO CRS operator for straight wells 41
3.2.3 2D CO CRS operator for arbitrary geometries 42
3.3 Performing coherence analysis in the data-domain 43
3.4 Poststack imaging using the CO CRS stack 46
3.4.1 Technical issues 47
3.4.2 Resulting imaging space 48
3.5 Wavefield separation using CRS attributes 52

4 Three VSP data examples **55**

4.1 A: Synthetic seismic data—straight vertical well 55

4.1.1 Data description 56

4.1.2 Velocity calibration and wavefield decomposition 57

4.1.3 CRS-processing and depth migration 62

4.1.4 Summary and conclusions 69

4.2 B: Real field data—straight vertical well 72

4.2.1 Data description 72

4.2.2 CRS-based wavefield decomposition 73

4.2.3 CO CRS-processing 74

4.2.4 Depth migration and conclusions 76

4.3 C: Synthetic seismic data—deviated well 81

4.3.1 Data description 81

4.3.2 CRS-processing 84

4.3.3 Conclusions 86

5 Promising new directions **89**

5.1 Surface seismics revisited 89

5.2 CRS stack as a kinematic filter 97

5.3 Multicomponent data: Out-of-plane indicator 99

5.4 Mapping VSP data to surface seismic data 103

6 Conclusions and outlook **107**

A Examples for promising CRS operators **111**

A.1 Common offset CRS operator for 3D wave propagation 111

A.2 CO CRS operator for 2D using the vertical velocity gradient at G 112

B An alternative CO CRS processing strategy **113**

C Description of used hard- and software **115**

List of figures **116**

Bibliography **121**

Acknowledgments **125**

Chapter 1

Introduction

The motivation of recording seismic data is to recover an image of the geologic structure in the subsurface and to learn about the material properties of which it is composed. Looking at *imaging* alone one has to overcome a significantly computer-intensive challenge. That is the reason, why scientists for decades have sought out processing strategies that remain computationally effective, yet, provide accurate subsurface images. The best means to treat seismic data is by using *prestack migration* but the method is generally time-consuming and requires an accurate velocity function, underlying the calculations.
Just to provide another connection, the estimation of a velocity function from seismic data is an *ill-posed* inverse problem. This means that from the little amount of information provided by seismic measurements an infinite number of unique solutions for a velocity model can be constructed. As a consequence the most accurate imaging method, i.e., full prestack migration, cannot be employed if only little is know about the area under investigation. Therefore, choosing an approximation of latter method—introducing reliability and robustness with a tradeoff in accuracy—can be a true alternative. In this thesis such an approximation in form of a sophisticated traveltime expression is investigated.

1.1 Seismic data acquisition

Concepts like *homogeneity*, *heterogeneity*, *acousticity*, and *elasticity* control the types of seismic waves which can be generated and for which I can expect to measure associated physical quantities. Generally, seismic experiments are divided into the categories of marine and land acquisition, the former being conducted in water (acoustic, homogeneous), the latter in elastic, heterogeneous solids. Fluids will only support the propagation of compressional waves (P-waves)

and usually pressure variations will be recorded. Solid media additionally support shearwaves propagation (S-waves) and the three components of particle velocity can be recorded.
There exists some variety in the selection of source and receiver distributions tied to the restrictions which marine- and land-based acquisition impose:

- Marine acquisition is dominated by *towed-streamer* experiments for which considerably few sources and many receivers placed horizontally are dragged like a carpet through the shallow part of the water column. *Ocean-bottom-seismic* (OBS) or *-cable* (OBC) experiments place a comparably sparse number of receivers on the ocean floor while the seismic sources remains at sea level.

- In land data-acquisition the *surface seismic* experiment is the commonly used method in which sources and receivers are either placed directly on the surface or buried up to a few meters in the earth in order to achieve a better coupling.

- In both regimes, *vertical-seismic-profile* (VSP) measurements can be carried out for which an array of receivers is lowered down an existing borehole—reaching approximately the depth of a targeted reservoir—while the seismic sources remain at either surface or sea-level. Figure 1.2(a) displays a sketch of the prominent features. A close relationship to the more exotic *vertical-cable* experiments exists for which a string of receivers remains either hanging in the water-column or in a shallow borehole less than 500 m deep.

1.2 Kirchhoff depth migration

The imaging of reflectors characterizing the subsurface requires the removal of the effects which wave propagation—going from a source to a reflector and back to the receivers—introduces. The way to achieve this, is by using migration methods, originating from *wave propagation-theory*. There exist many types of migration methods involving themself in different ways to solve the wave equation (see, e.g., Biondi, 2007). One particular method is called *Kirchhoff migration* which is an integral solution of the problem being based on *Green's function* theory.
In more detail, Kirchhoff migration focuses reflections by summation over the multidimensional data volume which was recorded previously. If I discretize the initial integral expression, I am left with the following finite sum as an approximative solution for the image I of one spatial point ξ:

$$I(\xi) \approx \sum_{i \in \Omega_\xi} W_i(\xi, s_i, g_i)\, D\left[t = t_D(\xi, s_i, g_i), s_i, g_i\right] . \tag{1.1}$$

The above expression is the sum of the data values $D(t,s,g)$ evaluated at the time $t_D(\xi,s,g)$ and weighted by an appropriate factor $W(\xi,s,g)$ not being further explained here (see, e.g.,

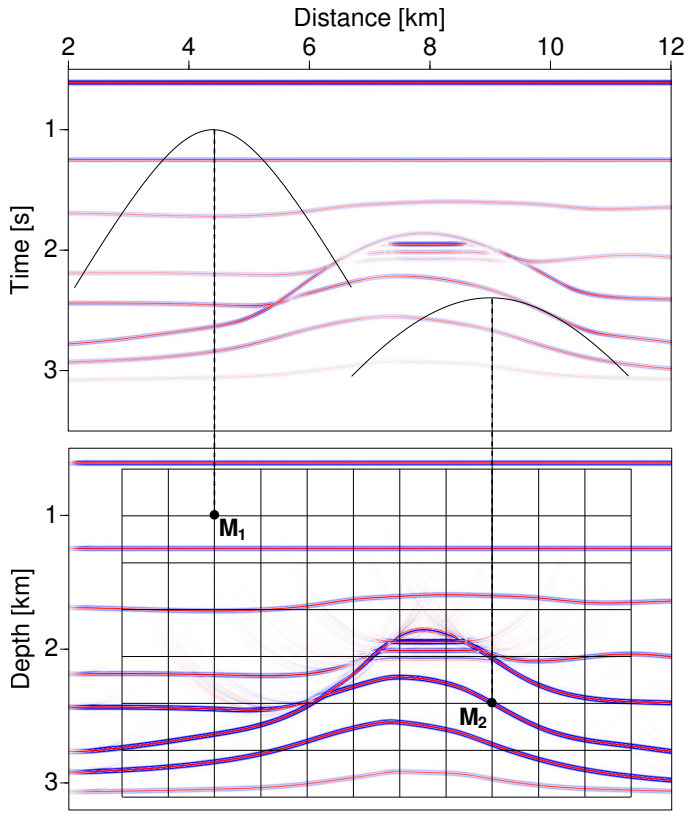

Figure 1.1: *Illustration of Kirchhoff depth migration. (Image kindly provided by Miriam Spinner, Karlsruhe University.)*

Schleicher et al. (2007)). Variables s (source) and g (geophone) denote the positions at which the data were measured and stand in close relationship to the migration *aperture* Ω_ξ. The aperture is important for limiting the visual perspective of the migration and the computational costs of the whole procedure.

The time $t_D(\xi, s, g)$ is the accumulated total delay of a reflection event propagating from source to receiver via image point $I(\xi)$. The full set of time delays for all source-receiver pairs contained in the aperture defines a *summation surface*, which has the fundamental physical interpretation of being a *diffraction surface* for a scatterpoint within the medium. To put it differently, diffractions from scatterers placed inside the subsurface will produce seismic events having the same shape as the summation surfaces.

The top image shown in Figure 1.2 is a near-offset section of recorded reflection events generated from a synthetic 2D model. Two diffraction curves are placed as an overlay on the time section being related to points M_1 and M_2 in the bottom depth image. After a summation of the amplitude information found along these curves—as well as all the other curves not shown, yet, related to the remaining depth points—the depth image is reconstructed.

1.3 Vertical seismic profiling geometries

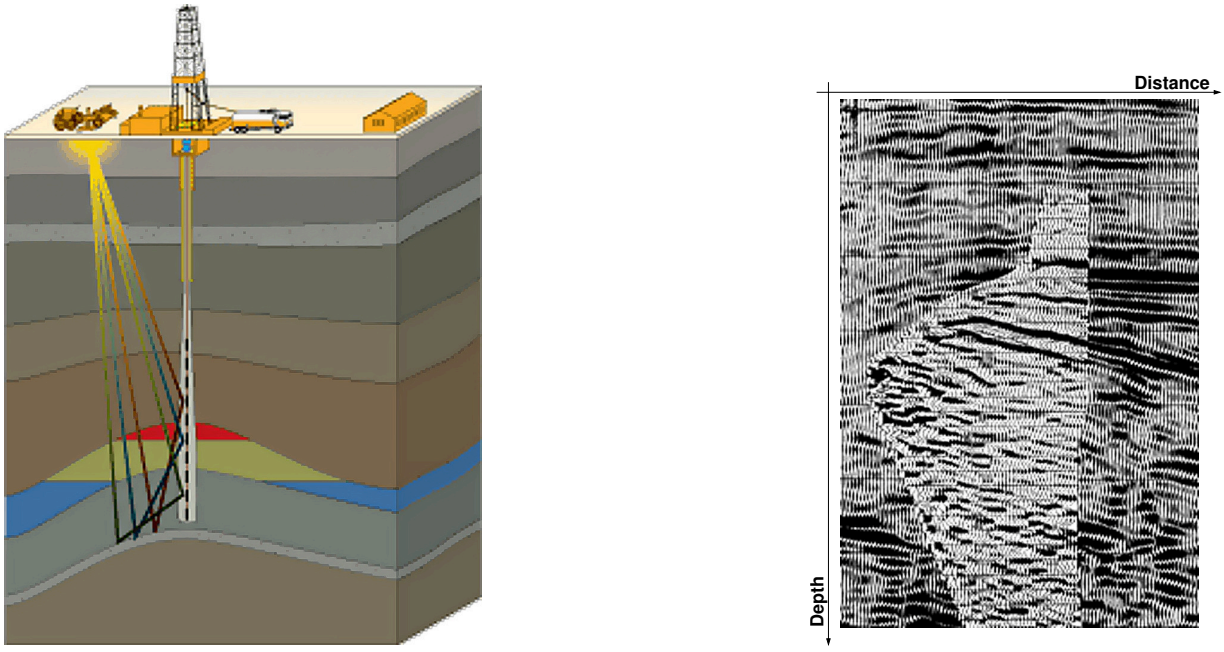

(a) Sketch of onshore VSP acquisition.

(b) Comparison of depth migration results.

Figure 1.2: *Motivation for seismic recordings in boreholes. (Figures courtesy of Baker Hughes Incorporated. All rights reserved.)*

The idea of lowering a geophone down a borehole to get a better handle on rock velocity is an old concept. Geophysicists have practiced it since the 1930's with increasing precision. The presence of a drilled well presents a truly unique opportunity to:

- Investigate a target formation more closely with acoustic measurements.
- Minimize subsurface attenuation phenomena.
- Measure depth and local material properties, accurately.

With the development of a multi-level array tool the vertical seismic profile technology has evolved significantly over the last two decades (Doherty, 2004). In earlier times, each desired receiver position required that the tool be moved up or down the hole, clamped to the borehole wall at some discrete depth, and after the recording being registered, being moved again. This time-consuming process has become deprecated with array-sizes increasing beyond 40 levels, today.

It has been widely accepted that the downhole measurement of seismic signals is effective for data acquisition with higher bandwidth and higher signal to noise ratio. An example for the enhanced quality of a VSP image over a surface seismic image is provided in Figure 1.2(b). Seismic data that are recorded on geophones that are deployed in boreholes contain upgoing and downgoing P- and S-wave arrivals. Most imaging tools used currently require the downgoing portion of the energy to be attenuated. In Figure 1.3 a multicomponent common-shot gather can be observed which includes the most common, different arrivals. The source which was able to achieve such a clear distinction between downgoing P- and S-waves was a detonating cord while in conventional acquisition mobile vibrators or small charges will be used. The established means to decompose the upgoing wavefields prior to an individual imaging is called *hodogram analysis* firstly introduced by DiSiena et al. (1984). An illustration of this method, without a further explanation is given in Figure 1.4. The main problem of hodogram analysis is to maintain the stability of recovered polarization angles along reflection events.
For a more recent coverage of processing methods of different types of VSP data I recommend the book by Hinds et al. (1996) which includes a large number of interesting examples. Hardage (1983) not only offers a broad overview respective the "classic" acquisition and processing of VSP measurements but also has a good tutorial character which helps to overcome the initial unfamiliarity of this geometry. Figure 1.5 gives a first impression of how a whole volume of synthetic VSP data for an acoustic medium with two reflectors will typically look like.

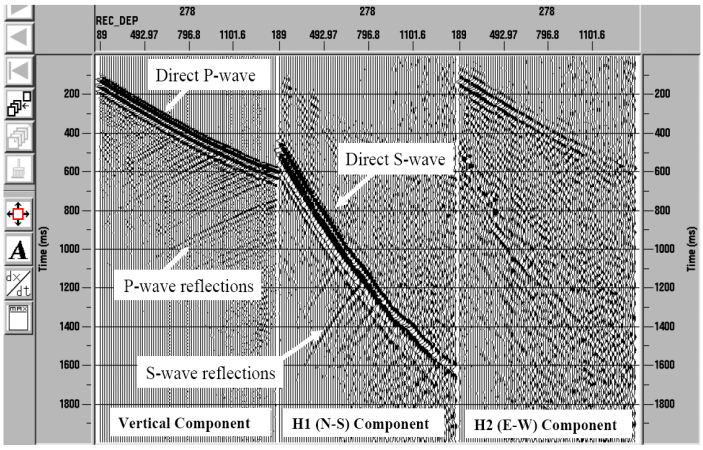

Figure 1.3: *Common shot gather - checkshot. (Image courtesy of P/GSI. All rights reserved.)*

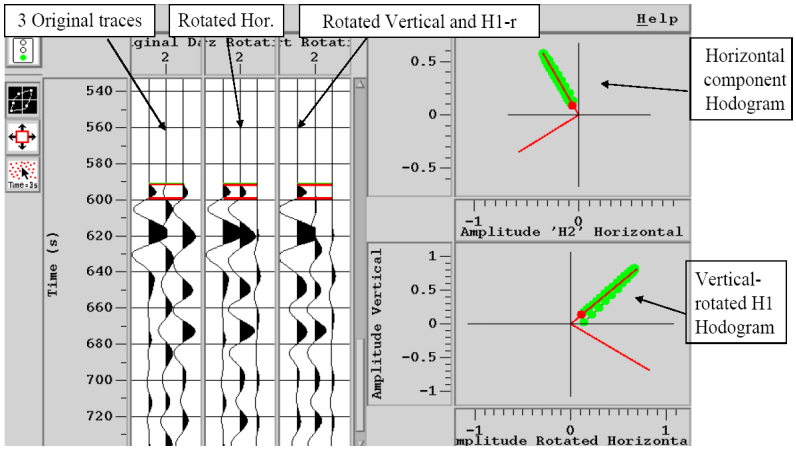

Figure 1.4: *VSP data: Hodogram analysis. (Image courtesy of P/GSI. All rights reserved.)*

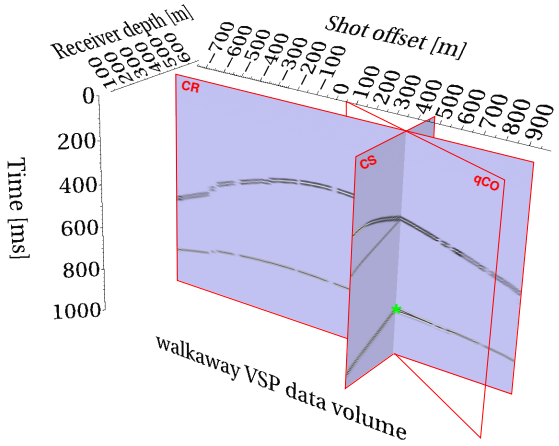

Figure 1.5: *Data volume obtained by a synthetic walkover VSP survey.*

1.4 Structure of the thesis

The thesis is divided into four main parts:

Theory (Chapter 2):
Firstly, I will introduce the most prominent foundations on which the description of seismic waves in the subsurface is based. On arriving at the solution of the so-called *eikonal equation* by the means of *ray-tracing systems*, I will generalize the approach to *dynamic* ray-tracing in coordinate systems which are particularly suited for this treatment. Finally, with the help of the *ray-propagator matrix* and the *two-point eikonal*, I will derive how the deviation of traveltime for two points on a paraxial ray can be expressed by the respective displacement to two points on a central ray.

CRS Operators and Implementation (Chapter 3):
The association of the ray-propagator matrix with physically interpretable *kinematic wavefield attributes* leads me to a *common-offset common-refection-surface* (CO CRS) traveltime operator for arbitrary acquisition geometries in 3D media.
Furthermore, I will limit this very general operator to the VSP acquisition geometry as the complete version would consist of too many terms to be of any educative value for the scope of this thesis. One particular description will be formulated by restricting the receiver side to a local approximation using one monotonous variable which parameterizes the space curve of the well. For wave propagation assumed to occur in 2.5D media the associated CRS operator will remain in its general form as its utilization has proven to be computationally feasible.
The remainder of this chapter covers the discussion of the search strategy to obtain a stable quintet of CRS attributes for every sample of a simulated time series. There will also be a discussion of the handling of multicomponent seismic data in the context of CO CRS-based imaging.

Three VSP data examples (Chapter 4):
In the third part of my thesis, the implementation of one of the search strategies is put to the test on three different seismic data sets:

- The first example consists of two multicomponent walkover data sets obtained by elastic raytracing from an isotropic, inhomogeneous 3D model with two reflectors. This data was the most fruitful to experiment with as it was considered to be simple but yet contained several challenging features.
- The second example is one set of multicomponent walkover field data provided by **Vaquero Energy** on which the synthetic data of the first example was roughly based. The challenge here was mainly the search for a suitable preprocessing prior to delivering the imaging strategy. As the subsequent Kirchhoff depth migrations of both prestack data and

the stacked traces showed great similarity — with even more continuity visible on the CRS stacked image — I consider this result an excellent confirmation of the method.

- The final example has again more of a research character as it is based on a synthetic finite-differences modeling result of a survey for a deviated well. The results are on display here mainly to further emphasize the versatility of the approach.

As will be seen, all of the examples produced very interesting results as I was able to extract substantial information from each data. In conclusion I can declare the work conducted with the new method a promising achievement.

New directions beyond scope (Chapter 5):
The final discussions of the thesis center around the question of useful by-products accumulated while working and contemplating on the CO CRS method for VSP. As I refuse to waste ideas which were just improper for the scope of my thesis, I will briefly introduce several observations I made which could serve as initial stepping stones into fruitful research. This chapter, serving as a "legacy" will hopefully encourage even more fellow researchers to join into the subject.

In the end I wish to summarize some key aspects I wanted to see investigated by an alternative CO CRS imaging scheme:

- Can five stacking parameters be safely determined in synthetic VSP data?
  - If yes, how is the performance for VSP field data?
- Is the lateral resolution for a CO CRS stacked set of seismic traces comparable to the one obtained by conventional processing?
- Is there any further application for the CO-CRS attributes apart from stacking? Can any new attributes be derived from the existing set?
- Do phase-shifts in seismic wavelets due to overcritical reflection-angles impact on the imaging at all?
- Can the assumption of planar wave propagation be maintained in 3D inhomogeneous media? How are multicomponent data affected by this?
- Is it possible to safely distinguish P- and S-wave reflection events in seismic data with yet no wavefield decomposition applied?

Fortunately, after the time invested in this wide scope of subjects, I am able to give an explanation to most of these questions.

Chapter 2

Theory

In the following, I summarize the most significant steps necessary to derive a traveltime approximation which is asymptotically valid for high frequency wave propagation in isotropic, inhomogeneous media. For that purpose I shall introduce the concept of *characteristic rays* which solve the underlying differential equation in a similar way as in geometrical optics. The intention behind my derivations lies in the quantification of an *inverse problem* for the domain where seismic data is usually measured, i.e., the *time domain*.
Additional emphasis lies on the description of the *ray-propagator* formalism because it simplifies relating the traveltime approximation to the propagation of wavefronts in the subsurface. Introducing initial conditions for these propagating wavefronts but also considering symmetry conditions leads me to the expression of a so-called *two-point eikonal*. It can be regarded the most general form of traveltime approximation as it is not tied to a particular geometry for the vicinity at either end-point and also is able to consider the gradient of the velocity field.
Finally, I will discuss the relationship between paraxial slowness vectors and their respective traveltimes, because they are essential for a stable wavefield decomposition of multicompont seismic data.

The necessary derivations will be based on the paraxial ray theory (see, e.g., Červený et al. (1984) or Chapman (2004)), which on the one hand may be considered less descriptive but, on the other hand, is much more elegant than other methods, e.g., ray perturbation theory (see, Bortfeld, 1989; Farra, 1999).

2.1 Linear elastodynamics

The discussion of linear elastodynamics has been a topic in numerous textbooks and papers from which the most popular nowadays is the one carried out by Aki and Richards (1980). Another excellent treatment by Ikelle and Amundsen (2005) is highly recommended as well. I shall use an analog notation to give a brief outline of the first steps necessary to establish the laws of particle motion.

A particle under observation is characterized by its original position $\vec{\mathsf{x}}$ at a reference time and its displacement vector from that position $\vec{\mathsf{u}}(\vec{\mathsf{x}},t)$ at a given time t. The introduction of stress tensor $\tau_{ij}(\vec{\mathsf{x}},t)$ generalizes the concept of a force acting on a single particle to a continuum, making it possible to quantify traction $\vec{\mathsf{T}}$ across the faces of an infinitesimal volume.
The deformation of a medium on the other hand is described by the strain tensor $e_{ij}(\vec{\mathsf{x}},t)$, which accounts for the particle motion of two neighboring points respective of their original positions after subtracting their uniform translation:

$$e_{ij} = \frac{1}{2}\left(\frac{\partial \mathsf{u}_i}{\partial \mathsf{x}_j} + \frac{\partial \mathsf{u}_j}{\partial \mathsf{x}_i}\right) \tag{2.1}$$

The elastodynamic equation establishes the relationship between spatial variation in the stress field and the temporal variations of the displacement vector according to Newton's second law of motion. For the sake of simplicity I demand that effects like energy dissipation and material transport play an insignificant role thus being excluded from the derivations. Additionally, adiabatic conditions for the particle displacement are assumed to apply:

$$\frac{\partial \tau_{ij}}{\partial \mathsf{x}_j} + \mathsf{f}_i = \rho\, \ddot{\mathsf{u}}_i\,. \tag{2.2}$$

The vector $\vec{\mathsf{f}}$ denotes the contribution of internal body forces acting on the medium, e.g., gravity. The simplest way to connect the stress and the strain tensor is a linear relationship, i.e., the generalized Hooke's law, under the assumption of a perfectly elastic solid,

$$\tau_{ij} = c_{ijkl}\, e_{kl}\,, \tag{2.3}$$

with the elastic tensor c_{ijkl} being symmetric and comprised of a total of 21 independent elastic moduli for an arbitrarily anisotropic medium. In the subsurface structures encountered in reality, elastic moduli are generally spatially-varying, while they remain constant for the homogeneous layering of simple synthetic models.

2.2 The elastodynamic equation for heterogeneous isotropic media

If I now express the stress-strain relation (2.3) in terms of the dislocation vector using (2.1)—taking into account the symmetry relations—and insert the result into (2.2), I obtain

$$\frac{\partial}{\partial \mathsf{x}_j}\left(c_{ijkl}\,\frac{\partial\,\mathsf{u}_k}{\partial\,\mathsf{x}_l}\right)+\mathsf{f}_i=\rho\,\ddot{\mathsf{u}}_i\,. \tag{2.4}$$

This equation is categorized as a system of three coupled partial differential equations of second order for the dislocation vector and its derivatives. For the desired case of an isotropic solid I can express the elastic tensor by means of only two elastic parameters, the so-called Lamé parameters, λ and μ and the Kronecker symbol δ_{ij}:

$$c_{ijkl}=\lambda\,\delta_{ij}\,\delta_{kl}+\mu\,(\delta_{ik}\,\delta_{jl}+\delta_{il}\,\delta_{jk})\,. \tag{2.5}$$

The physical explanation of the elastic parameters can be found comprehensively in many textbooks (see, Bullen and Bolt, 1985) and is of no further concern here.
If I now apply expression (2.5) to (2.4) the elastodynamic equation can be written in vectorial form with only three material parameters altogether:

$$\begin{aligned}(\lambda+\mu)\,\vec{\nabla}\left(\vec{\nabla}\cdot\vec{\mathsf{u}}\right)+\mu\left(\vec{\nabla}\cdot\vec{\nabla}\right)\vec{\mathsf{u}}+\vec{\nabla}\lambda\left(\vec{\nabla}\cdot\vec{\mathsf{u}}\right)\\ +\vec{\nabla}\mu\times\left(\vec{\nabla}\times\vec{\mathsf{u}}\right)+2\left(\vec{\nabla}\mu\cdot\vec{\nabla}\right)\vec{\mathsf{u}}+\vec{\mathsf{f}}=\rho\ddot{\vec{\mathsf{u}}}\,.\end{aligned} \tag{2.6}$$

The most common approaches to investigate the seismic wavefield in complex media are based either on the appropriate numerical solution of the elastodynamic equation or on approximate asymptotic solutions of this equation valid only for high frequencies. One of the latter is the so-called ray-series method, which is today highly developed and widely used.

If one studies the propagation of elastic plane waves in homogeneous media assuming acoustic, isotropic, or anisotropic material properties he will observe an increasing number of separated wavemodes. It is possible not only to determine the velocities of propagation of each wavemode but also the polarization of plane waves of vectorial character. In an inhomogeneous medium wave propagation is much more complex—the wavemodes only separate approximately—thus being only similar to wavemodes in a homogenous medium within a local vicinity.

2.2.1 High-frequency ansatz for wave propagation

Starting from a measured signal $x(t)$, an analytical signal $F(t)=x(t)+i\,g(t)$ with the two functions $x(t)$ and $g(t)$ forming a Hilbert transform pair is defined as a *high-frequency analytical*

signal, if its Fourier spectrum vanishes for low frequencies,

$$|F(\omega)| = 0\,, \qquad \text{for} \quad 0 \leq \omega \leq \omega_0\,, \tag{2.7}$$

with ω_0 specifying a high frequency. This assumption results in the progressive increase of the absolute value of $F(t)$ with each time-derivative:

$$|F(t)| \ll \left|\dot{F}(t)\right| \ll \left|\ddot{F}(t)\right|. \tag{2.8}$$

The solution of the elastodynamic equation will be enforced by the seismic signal posessing the previously described property. In a physical sense the high-frequency assumption can only be considered valid if the relevant material properties of a medium do not vary too much over distances of the order of a wavelength. This wavelength is tied to the prevailing frequency of the seismic signal for an average propagation velocity at a given point.
Basically, I am left with the choice of either solving the elastodynamic equation for vectorial or scalar quantities, depending on the measured quantity in a seismic experiment and the character of an investigated medium.

The ansatz for the displacement vector reads

$$\vec{u}(\vec{x},t) = \vec{U}(\vec{x})\,F\left(\zeta\right)), \tag{2.9}$$

with $F(\zeta)$ representing a high-frequency analytical signal of the form $\zeta = t - T(\vec{x})$. The relevant temporal and spatial derivatives of displacement vector (2.9) compute to:

$$\begin{aligned}
\vec{\nabla}\vec{u} &= \vec{\nabla}\vec{U}\,F - (\vec{U}\,\vec{\nabla}T)\,\dot{F}\,,\\
\vec{\nabla}(\vec{\nabla}\vec{u}) &= \vec{\nabla}(\vec{\nabla}\vec{U})\,F - \vec{\nabla}\vec{U}\,\vec{\nabla}T\,\dot{F} - \vec{\nabla}(\vec{U}\,\vec{\nabla}T)\,\dot{F} + (\vec{U}\,\vec{\nabla}T)\,\ddot{F}\,\vec{\nabla}T\,,\\
\nabla^2\vec{u} &= \nabla^2\vec{U}\,F - \vec{U}\,\nabla^2T\,\ddot{F}\,,\\
\vec{\nabla}\times\vec{u} &= \vec{\nabla}\times\vec{U}\,F - \vec{\nabla}T\times\vec{U}\,\dot{F}\,,\\
\ddot{\vec{u}} &= \vec{U}\,\ddot{F}\,.
\end{aligned} \tag{2.10}$$

After inserting expression (2.9) into equation (2.6) while setting the external forces $\vec{f} \equiv 0$, I can separate all contributing terms by the derivatives of the analytic signal and receive,

$$\vec{N}(\vec{U},T)\,\ddot{F} - \vec{M}(\vec{U},T)\,\dot{F} + \vec{L}(\vec{U})\,F = \vec{0}, \tag{2.11}$$

with the following expressions as the coefficients

$$\begin{aligned}
\vec{N}(\vec{U},T) &= -\rho\,\vec{U} + (\lambda+\mu)\,(\vec{U}\,\vec{\nabla}T)\,\vec{\nabla}T + \mu\,\nabla^2T\,\vec{U}\,,\\
\vec{M}(\vec{U},T) &= (\lambda+\mu)\left[\vec{\nabla}\vec{U}\,\vec{\nabla}T + \vec{\nabla}(\vec{U}\,\vec{\nabla}T)\right] + (\vec{U}\,\vec{\nabla}T)\vec{\nabla}\lambda + \vec{\nabla}\mu\times(\vec{\nabla}T\times\vec{U}) + 2(\vec{\nabla}\mu\,\vec{\nabla})T\,\vec{U}\,,\\
\vec{L}(\vec{U}) &= (\lambda+\mu)\vec{\nabla}(\vec{\nabla}\vec{U}) + \mu\nabla^2\vec{U} + (\vec{\nabla}\vec{U})\vec{\nabla}\lambda + \vec{\nabla}\mu\times(\vec{\nabla}\times\vec{U}) + 2(\vec{\nabla}\mu\,\vec{\nabla})\vec{U}\,.
\end{aligned} \tag{2.12}$$

Since my ansatz (2.9) also requires the inequalities (2.8) to be valid the dominant terms in the approximate solution of equation (2.11) are the derivatives with $\vec{\mathsf{N}}(\vec{\mathsf{U}},T)$ and $\vec{\mathsf{M}}(\vec{\mathsf{U}},T)$. Another requirement of this type of ansatz is that each of the three coefficient-functions has to vanish independently for all frequencies so I can set them equal to zero.
Setting $\vec{\mathsf{N}}(\vec{\mathsf{U}},T) \equiv 0$ yields, as I will show, the *eikonal equations* for two individual wavefields corresponding to P and S waves as it governs the kinematic aspect of wave propagation. The equation $\vec{\mathsf{M}}(\vec{\mathsf{U}},T) \equiv 0$ can be used to calculate the amplitudes of those two wavefields and is a general representation of the *transport equations*. The third coefficient-function $\vec{\mathsf{L}}(\vec{\mathsf{U}})$ is generally neglected as it only yields trivial solutions. In the following I also will neglect the transport equations as I am mainly interested in the calculation of traveltimes using ray theory.

2.2.2 The eikonal equation and its eigenvalue problem

I can easily reformulate the eikonal equations in such a way that they resemble a system of equations known from linear algebra as a typical *eigenvalue problem*:

$$(\Gamma_{ij} - \delta_{ij})\mathsf{U}_i = 0\,, \qquad \text{with} \qquad \Gamma_{ij} = \frac{\lambda+\mu}{\rho}\frac{\partial T}{\partial \mathsf{x}_i}\frac{\partial T}{\partial \mathsf{x}_j} + \frac{\mu}{\rho}\delta_{ij}\frac{\partial T}{\partial \mathsf{x}_k}\frac{\partial T}{\partial \mathsf{x}_k}\,. \tag{2.13}$$

The hereby introduced 3×3 matrix Γ_{ij} is commonly known as the *Christoffel matrix*—displayed here for the special case of isotropy. In a next step, I can with little effort determine the three corresponding eigenvalues E_i by setting

$$\det(\Gamma_{ij} - E\,\delta_{ij}) = 0\,, \tag{2.14}$$

and solving the resulting cubic algebraic equation. This leads to the eigenvalues,

$$E_1 = \frac{\lambda+2\mu}{\rho}\,\vec{\nabla}T\cdot\vec{\nabla}T \qquad \text{and} \qquad E_2 = E_3 = \frac{\mu}{\rho}\,\vec{\nabla}T\cdot\vec{\nabla}T\,, \tag{2.15}$$

corresponding to the already-mentioned two different wave modes, which can be observed in elastodynamic, isotropic media.
They are interpreted as the longitudinal primary (P) wave and the *degenerate solution* for two types of secondary (S) waves, which are generally decoupled in anisotropic media. P waves are linearly polarized with particle motion being parallel to the propagation direction of a wavefront. The S waves are polarized in the plane being tangent to the wavefront with the direction of the polarization being a superposition of its *eigenvectors*—usually chosen mutually perpendicular in that plane.
According to equation (2.13), the eigenvalues E_1, or E_2 and E_3 also have to be equal to one. This provides us with the commonly known formulations of the eikonal equations for P and S waves so that

$$\vec{\nabla}T\cdot\vec{\nabla}T = 1/\alpha^2 \qquad \text{and} \qquad \vec{\nabla}T\cdot\vec{\nabla}T = 1/\beta^2\,, \tag{2.16}$$

introducing the P wave velocity $\alpha = \sqrt{\frac{\lambda+2\mu}{\rho}}$ and the S wave velocity $\beta = \sqrt{\frac{\mu}{\rho}}$.

2.2.3 The Hamiltonian and its characteristic equations

The eikonal equations (2.16) taken by themselves are nonlinear partial differential equations which are usually solved by the method of *characteristics* (see, e.g., Herzberger, 1958). Characteristics are 6 dimensional trajectories in the phase space $\vec{x}(\xi)$-$\vec{p}(\xi)$, with a parameter ξ, indicating the progress along the curve, which solve the eikonal equations. In geophysics they correspond to the *ray*-trajectories.
Substituting the P and S wave velocities α and β, respectively, by a general wave propagation velocity v, leads to the eikonal equations in their general form

$$\vec{p}\cdot\vec{p} = \frac{1}{v^2(\vec{x})}, \qquad \text{with} \qquad \vec{p} = \vec{\nabla}T\,. \tag{2.17}$$

I previously also introduced the *slowness vector* $\vec{p}$ which is simply the gradient of the traveltime T. It is now possible to arrange the two terms of equation (2.17) in several different ways classified as so-called *Hamiltonian* expressions $\mathscr{H}(\vec{x},\vec{p}(\vec{x})) = 0$. Some examples are given by

$$(\vec{p}\cdot\vec{p} - 1/v^2)/2 = 0 \quad \Leftrightarrow \quad (\vec{p}\cdot\vec{p})^{\frac{1}{2}} - 1/v = 0 \quad \Leftrightarrow \quad \frac{1}{2}\ln(v^2\,\vec{p}\cdot\vec{p}) = 0\,. \tag{2.18}$$

Many comprehensive textbooks have been published on the matter of this subject (see, e.g., Bleistein, 1984) so I will not go into any detail on how to arrive at the *characteristic system* of differential equations. But I will state them here for the sake of clarity of the subsequent steps.

$$\frac{\mathrm{d}x_i}{\mathrm{d}\xi} = \frac{\partial\mathscr{H}}{\partial p_i}, \qquad \frac{\mathrm{d}p_i}{\mathrm{d}\xi} = -\frac{\partial\mathscr{H}}{\partial x_i}\,. \tag{2.19}$$

Inserting one of the Hamiltonian expressions (2.18) into the system of equations (2.19) yields a *ray tracing system*. It can be used to calculate the trajectory of a ray through a given medium from a given starting point. Once the components of $\vec{x}$ and $\vec{p}$ are determined the traveltime T along the ray $\mathscr{C}$ can be obtained by integration along the variable ξ:

$$T = \int\limits_{\mathscr{C}} p_k \frac{\partial\mathscr{H}}{\partial p_k}\,\mathrm{d}\xi = \int\limits_{\mathscr{C}} \frac{1}{v(\vec{x},\vec{p})}\,\mathrm{d}\xi \tag{2.20}$$

2.3 Dynamic ray tracing by means of paraxial rays

The previous section was concerned with introducing a general approach to describe wave propagation in laterally inhomogeneous layered structures in order to solve *forward-modeling* problems. Dynamic ray tracing on the other hand is a method which is able to address *inverse seismic*

problems—as they are encountered commonly in seismic imaging. It establishes an approximative relationship between the trajectory of a *central ray* Ω and the path of any trajectory within a certain proximity of it which is called the *paraxial* vicinity. An inverse problem is therefore solved by finding the optimum matching physical properties for a central ray in order to describe the reflection events recorded into seismic traces which lie in its neighboring region.

The intermediate step which has to be taken to arrive at dynamic ray tracing leads across the introduction of the *paraxial ray tracing system*. Paraxial ray tracing is able to calculate approximate solutions for *phase-space coordinates* along the paraxial rays. By dynamic ray tracing it is moreover possible to exactly compute the partial derivatives of these phase-space coordinates taken along a central ray.

2.3.1 Paraxial ray tracing

For the derivation of the paraxial ray tracing system, I will consider a bundle of rays, which surrounds a so-called central ray. The central ray with the coordinates $(\vec{x},\vec{p})$ exactly solves a ray tracing system which can be established by (2.19) and any Hamiltonian expression (2.18).
Within the close vicinity of this central ray I now can extrapolate its solution—as long as the high-frequency assumption is maintained—in a way that it remains approximately valid for a portion of this bundle of rays. Consequently, this portion will be declared to be the paraxial rays with their coordinates being related to those of the central ray by $(\vec{x}+\Delta\vec{x},\vec{p}+\Delta\vec{p})$, with sufficiently small differences $\Delta\vec{x}$ and $\Delta\vec{p}$.
Further one particular representation along the trajectories of the rays $\mathrm{d}\xi = v^2\,\mathrm{d}\tau = \mathrm{d}\sigma$ is chosen with $\mathrm{d}\sigma$ being commonly referred to as the *optical length* originating from geometrical optics. The ray tracing systems for the central and all its paraxial rays can now be explicitly formulated and have the following relationship:

$$\begin{aligned} \frac{\mathrm{d}\vec{x}}{\mathrm{d}\sigma} = \vec{p}\,, \quad &\longrightarrow \quad \frac{\mathrm{d}(\vec{x}+\Delta\vec{x})}{\mathrm{d}\sigma} = \vec{p}+\Delta\vec{p}\,, \\ \frac{\mathrm{d}\vec{p}}{\mathrm{d}\sigma} = |\vec{p}|\,\vec{\nabla}|\vec{p}|\,, \quad &\longrightarrow \quad \frac{\mathrm{d}(\vec{p}+\Delta\vec{p})}{\mathrm{d}\sigma} = (|\vec{p}|+\vec{\nabla}|\vec{p}|\cdot\Delta\vec{x})\vec{\nabla}(|\vec{p}|+\vec{\nabla}|\vec{p}|\cdot\Delta\vec{x})\,, \end{aligned} \tag{2.21}$$

where I omitted the equations for the traveltimes since they are of no concern here. Accounting only up to the first orders of $\Delta\vec{x}$ and $\Delta\vec{p}$ will result in the linear approximations

$$\frac{\mathrm{d}\Delta\vec{x}}{\mathrm{d}\sigma} = \Delta\vec{p}\,, \qquad \text{and} \qquad \frac{\mathrm{d}\Delta\vec{p}}{\mathrm{d}\sigma} = \mathsf{F}\,\Delta\vec{x}\,, \tag{2.22}$$

with 3×3 matrix F consisting of the components

$$\mathsf{F}_{ij} = \frac{\partial|\vec{p}|}{\partial x_i}\,\frac{\partial|\vec{p}|}{\partial x_j} + |\vec{p}|\,\frac{\partial^2|\vec{p}|}{\partial x_i \partial x_j}\,. \tag{2.23}$$

By collecting the deviations of location and slowness vector into one six-dimensional *phase-space* displacement vector $\Delta\vec{\Phi}$ and introducing the *system matrix* $\mathsf{S}^{(x)}$ I can rewrite the paraxial ray tracing system (2.22) in a much clearer way,

$$\frac{\mathrm{d}\Delta\vec{\Phi}}{\mathrm{d}\sigma} = \mathsf{S}^{(x)}\,\Delta\vec{\Phi}\,, \qquad \text{with} \qquad \Delta\vec{\Phi} = \begin{pmatrix} \Delta\vec{\mathrm{x}} \\ \Delta\vec{\mathrm{p}} \end{pmatrix}, \quad \text{and} \quad \mathsf{S}^{(x)} = \begin{pmatrix} \mathsf{O} & \mathsf{I} \\ \mathsf{F} & \mathsf{O} \end{pmatrix}. \tag{2.24}$$

The system matrix contains the elements O which is a 2×2 null matrix and matrix I being a 2×2 identity matrix.

2.3.2 The ray propagator matrix

Another useful formalism to describe the properties of a paraxial ray is provided with the help of the *ray propagator matrix* Π. By selecting two points S and G on a central ray as well as two points S' and G' situated on a paraxial ray the deviation of the phase-space coordinates between primed and unprimed symbols can be expressed by introducing $\Delta\vec{\Phi}_S$ and $\Delta\vec{\Phi}_G$.

If a linear relationship between both phase-space deviation vectors is assumed, their transformation matrix $\Pi(G,S)$ is introduced by writing

$$\Delta\vec{\Phi}_G = \Pi(G,S)\,\Delta\vec{\Phi}_S\,, \tag{2.25}$$

where the ray propagator matrix will consequently be a solution of system (2.24).
One remarkable feature of the ray propagator matrix is the *symplectic property* which I will briefly state here to read

$$\Pi^T\,\mathsf{J}\,\Pi = \mathsf{J}\,, \quad \text{with} \quad \mathsf{J} = \begin{pmatrix} \mathsf{O} & \mathsf{I} \\ -\mathsf{I} & \mathsf{O} \end{pmatrix}. \tag{2.26}$$

The four symplectic invariants stated above represent the symmetry conditions satisfied by all dynamic ray tracing systems. They can be presented in many different forms which are of no further concern here. I will only use them implicitely later, e.g., when discussing the forward and backward propagation relations.

Another important observation is made by using Liouville's theorem, stating that propagator matrix $\Pi(G,S)$ and its inverse matrix not only share the same eigenvalues but also are nonsingular along a whole ray:

$$\det|\Pi(G,S)| = 1\,. \tag{2.27}$$

Other features—such as compliance to a chain rule—are beyond the scope of this thesis (see, e.g., Gilbert and Backus, 1966, for a detailed treatment). In Section (2.4.5) I will once more revert to the ray propagator formalism in a more thorough manner.

2.3.3 Dynamic ray tracing

The main aim of *dynamic ray tracing* is to overcome the limitations of the paraxial ray tracing system. It does so by quantifying the degree of similarity between the ray tracing systems of central and paraxial rays. The term "dynamic" originates from the fact that one constituent of this quantification accounts for the so-called *geometrical-spreading factor* and therefore can provide an estimate for the decay in amplitude of a wavefront.
In order to achieve an estimation of similarity, the phase-space displacement vector $\Delta\vec{\Phi}$, introduced in equation (2.24), is differentiated by a set of arbitrarily selected ray coordinates γ_i with $i = 1,2,3$ which characterize the central ray. Applying these derivatives to the paraxial ray tracing system yields

$$\frac{\mathrm{d}}{\mathrm{d}\sigma}\begin{pmatrix} \frac{\partial\vec{\mathrm{x}}}{\partial\gamma_i} \\ \frac{\partial\vec{\mathrm{p}}}{\partial\gamma_i} \end{pmatrix} = \mathsf{W}\begin{pmatrix} \frac{\partial\vec{\mathrm{x}}}{\partial\gamma_i} \\ \frac{\partial\vec{\mathrm{p}}}{\partial\gamma_i} \end{pmatrix}, \qquad \text{with} \qquad i = 1,2,3\,. \tag{2.28}$$

Then, the above system of matrix-multiplications is substituted by

$$\mathsf{Q}^{(x)}_{ij} = \frac{\partial\vec{\mathrm{x}}_i}{\partial\gamma_j}, \qquad \text{and} \qquad \mathsf{P}^{(x)}_{ij} = \frac{\partial\vec{\mathrm{p}}_i}{\partial\gamma_j}, \qquad \text{with} \qquad i,j = 1,2,3\,, \tag{2.29}$$

which results in what is commonly called the *dynamic ray tracing system*:

$$\frac{\mathrm{d}}{\mathrm{d}\sigma}\begin{pmatrix} \mathsf{Q}^{(x)} \\ \mathsf{P}^{(x)} \end{pmatrix} = \mathsf{W}\begin{pmatrix} \mathsf{Q}^{(x)} \\ \mathsf{P}^{(x)} \end{pmatrix}. \tag{2.30}$$

The advantage of the transformation into the dynamic phase space variables, i.e., the phase space variables' derivatives with respect to the ray coordinates γ_i, can be made obvious by the following consideration. If the dynamic ray tracing system is once solved for a certain central ray, it is possible to extend that knowledge to *any* paraxial ray by a simple multiplication of this solution with the displacement in-between the rays:

$$\begin{pmatrix} \mathrm{d}\vec{\mathrm{x}} \\ \mathrm{d}\vec{\mathrm{p}} \end{pmatrix} = \begin{pmatrix} \mathsf{Q}^{(x)} \\ \mathsf{P}^{(x)} \end{pmatrix}\begin{pmatrix} \mathrm{d}\gamma_1 \\ \mathrm{d}\gamma_2 \\ \mathrm{d}\gamma_3 \end{pmatrix}. \tag{2.31}$$

This means that the computational effort involved in tracing of paraxial rays will be greatly reduced.

2.4 Ray tracing in ray-centered coordinates

There are many examples of problems in physics where the proper choice of the coordinate system provides a clue to a much more elegant solution. This is also true in this case, where it is

possible to simplify the dynamic ray tracing system derived in the last section considerably by a transformation to the *ray-centered coordinate system*.
Ray tracing in this form was firstly used by Popov and Pšenčík (1978) to calculate the *geometrical spreading factor* $\mathscr{L}$ along a central ray. Shortly after that it was shown by Hubral (1979) how to directly relate the computed properties of the system to curvatures of propagating wavefronts.

2.4.1 Definition of ray-centered coordinates

I now will introduce a local coordinate system (q_1, q_2, q_3) connected to a given central ray Ω which defines its unit vectors to be varying along that ray. One of the coordinates, for instance q_3, is chosen to correspond to a monotonous parameter along the ray, e.g., the arclength s, while vectors $\vec{\mathsf{e}}_1$ and $\vec{\mathsf{e}}_2$ form a two-dimensional Cartesian coordinate system perpendicular to Ω at $q_3 = s$ with its origin on the central ray.
The vector $\vec{\mathsf{e}}_3$ is chosen to be the unit tangent $\vec{\mathsf{t}}$ to the central ray, i.e., to be perpendicular to the associated wavefront:

$$\vec{\mathsf{e}}_3 = \vec{\mathsf{t}} = \vec{\nabla} T = \frac{1}{|\vec{\mathsf{p}}|}\,\vec{\mathsf{p}} = v\,\vec{\mathsf{p}}\,. \tag{2.32}$$

Vectors $\vec{\mathsf{e}}_1$ and $\vec{\mathsf{e}}_2$ are selected to be mutually perpendicular. Therefore, any point expressed in ray-centered coordinates will be denoted by $\vec{\mathsf{q}} = (q_1, q_2, q_3)^T$ for its location and $\vec{\mathsf{p}}^{(q)} = (p_1^{(q)}, p_2^{(q)}, p_3^{(q)})^T$ for its slowness vector.

Now it would be useful to establish the relationship between the unit vectors, while propagating a wavefront at $q_3 = s$ further down its raypath by an infinitesimal distance ds. I will make use of the orthogonality of the unit vectors prior to constructing the derivatives leading to

$$\vec{\mathsf{e}}_I \cdot \vec{\mathsf{p}} = 0\,, \qquad \longrightarrow \qquad \frac{\mathrm{d}\vec{\mathsf{e}}_I}{\mathrm{d}s}\,\vec{\mathsf{p}} + \vec{\mathsf{e}}_I \cdot \frac{\mathrm{d}\vec{\mathsf{p}}}{\mathrm{d}s} = 0\,, \qquad I = 1,2\,. \tag{2.33}$$

Restricting the variations of $\vec{\mathsf{e}}_I$ to be aligned in direction of $\vec{\mathsf{e}}_3$ and the plane tangent to the wavefront for the opposite case yields

$$\frac{\mathrm{d}\vec{\mathsf{e}}_I}{\mathrm{d}s} = \varepsilon_{I3}\,\vec{\mathsf{p}}\,, \qquad \text{and} \qquad \frac{\mathrm{d}\vec{\mathsf{e}}_3}{\mathrm{d}s} = \varepsilon_{3I}\,\vec{\mathsf{e}}_I\,, \tag{2.34}$$

which have to be solved for ε_{I3} and ε_{3I}. This is done by inserting either of above equations into (2.33), multiplying by $\vec{\mathsf{p}}$, respectively $\vec{\mathsf{e}}_I$, and simplifying the results to read

$$\varepsilon_{I3} \;=\; -v^2(\vec{\mathsf{e}}_I \cdot \frac{\mathrm{d}\vec{\mathsf{p}}}{\mathrm{d}s}) = \vec{\mathsf{e}}_I \cdot \vec{\nabla} v = \frac{\partial v}{\partial q_I}\,, \qquad I = 1,2\,, \tag{2.35}$$

$$\varepsilon_{3I} \;=\; -\vec{\mathsf{e}}_3 \cdot \frac{\mathrm{d}\vec{\mathsf{e}}_I}{\mathrm{d}s} = -(\vec{\mathsf{e}}_I \cdot \vec{\nabla} v)\, p_3^{(q)} = -\frac{\partial v}{\partial q_I}\, p_3^{(q)}\,. \tag{2.36}$$

Finally, the derivatives of the unit vectors can be established:

$$\frac{\mathrm{d}\vec{\mathrm{e}}_I}{\mathrm{d}s} = \frac{\partial v}{\partial q_I}\,\vec{\mathrm{p}}\,, \qquad \text{and} \qquad \frac{\mathrm{d}\vec{\mathrm{e}}_3}{\mathrm{d}s} = -\left(\frac{\partial v}{\partial q_I}\,\vec{\mathrm{e}}_I\right) p_3^{(q)}\,. \tag{2.37}$$

2.4.2 Ray tracing system in ray-centered coordinates

A change of the coordinate system does not change any physical law but only alters the appearance of the expressions—sometimes even simplifying it. Therefore, the characteristic equations (2.19) introduced earlier will not change their physical behavior by a substitution of $\vec{\mathrm{x}}$ by $\vec{\mathrm{q}}$ and $\vec{\mathrm{p}}$ by $\vec{\mathrm{p}}^{(q)}$. Additionally, the optical length $\mathrm{d}\sigma$ from now on is replaced by the arclength $\mathrm{d}s$:

$$\frac{\mathrm{d}\vec{\mathrm{q}}}{\mathrm{d}s} = v\,\vec{\mathrm{p}}^{(q)}\,, \qquad \text{and} \qquad \frac{\mathrm{d}\vec{\mathrm{p}}^{(q)}}{\mathrm{d}s} = \nabla_q\left(\frac{1}{v}\right). \tag{2.38}$$

The gradient operator ∇_q takes the form of partial derivatives with respect to q_i for $i = 1,2,3$. For the third component $q_3 = s$ of the location vector the ray tracing system simplifies as already hinted to

$$\frac{\mathrm{d}s}{\mathrm{d}s} = v p_3^{(q)}\,, \qquad \text{and} \qquad \frac{\mathrm{d}p_3^{(q)}}{\mathrm{d}s} = \frac{\mathrm{d}}{\mathrm{d}s}\left(\frac{1}{v}\right), \tag{2.39}$$

which implies that $p_3^{(q)} = 1/v$.
Thus, the ray tracing system in ray-centered coordinates consists of only four independent equations

$$\frac{\mathrm{d}q_I}{\mathrm{d}s} = v p_I^{(q)}\,, \qquad \text{and} \qquad \frac{\mathrm{d}p_I^{(q)}}{\mathrm{d}s} = \frac{\mathrm{d}}{\mathrm{d}q_I}\left(\frac{1}{v}\right). \tag{2.40}$$

A central ray now is completely described by the third components of its location and slowness vector

$$\vec{\mathrm{q}} = (0,0,s)^T\,, \qquad \text{and} \qquad \vec{\mathrm{p}}^{(q)} = (0,0,1/v)^T\,. \tag{2.41}$$

2.4.3 Paraxial ray tracing in ray-centered coordinates

The previously introduced simplification also impacts the paraxial ray-tracing system as—by using the ray-centered coordinates—I only have to work with four differential equations instead of six. One possibility to derive its specific shape is initiated by a first-order Taylor expansion of the inverse of the velocity as it is present in right-hand-side expression of system (2.40). The description of the change of the slowness vector along the ray now reads

$$\frac{\partial}{\partial q_I}\left(\frac{1}{v}\right) = -\frac{1}{v^2}\frac{\partial v}{\partial q_I} = -\frac{1}{v^2}\frac{\partial}{\partial q_J}\left.\frac{\partial v}{\partial q_I}\right|_{\vec{\mathrm{q}}=\vec{0}} q_J\,, \qquad I,J = 1,2\,. \tag{2.42}$$

A matrix V containing the second derivatives of the velocity field is defined according to

$$\frac{\partial}{\partial q_I}\left(\frac{1}{v}\right) = -\frac{1}{v^2}\,\frac{\partial}{\partial q_J}\frac{\partial v}{\partial q_I}\bigg|_{\vec{\mathsf{q}}=\vec{0}} q_J = -\frac{1}{v^2}\,\mathsf{V}_{IJ}\,q_J\,. \tag{2.43}$$

If I now replace the above term in ray tracing system (2.40) this will already yield the corresponding paraxial system. It also exists a popular compact representation of it as an analog to (2.24) but now for ray-centered coordinates:

$$\frac{\mathrm{d}}{\mathrm{d}\sigma}\mathsf{W}^{(q)} = \mathsf{S}\mathsf{W}^{(q)}\,, \quad \text{with} \quad \mathsf{W}^{(q)} = \left(q_1, q_2, p_1^{(q)}, p_2^{(q)}\right)^T, \quad \text{and} \quad \mathsf{S} = \begin{pmatrix} \mathsf{O} & v\mathsf{I} \\ -1/v^2\,\mathsf{V} & \mathsf{O} \end{pmatrix}. \tag{2.44}$$

Let me repeat again that even though the paraxial raytracing system is linear and hereby very convenient for further use it is merely a crude approximation for a paraxial vicinity of small q_1 and q_2.

2.4.4 Dynamic ray tracing in ray-centered coordinates

Once again a dynamic ray tracing system is established by taking the derivatives of system (2.44) with respect to the ray-coordinates γ_K. This is done in analogy to my derivations in Section 2.3.3, but now only for $K = 1, 2$. It yields two 2×2 matrices Q and P in similar fashion as in Cartesian coordinates:

$$\frac{\partial}{\partial\gamma_K}\frac{\mathrm{d}q_I}{\mathrm{d}s} = \frac{\partial}{\partial\gamma_K}\left(v\,p_I^{(q)}\right), \quad \Longleftrightarrow \quad \frac{\mathrm{d}}{\mathrm{d}s}\mathsf{Q} = v\,\frac{\partial p_I^{(q)}}{\partial\gamma_K}\,, \tag{2.45}$$

$$\frac{\partial}{\partial\gamma_K}\frac{\mathrm{d}p_I^{(q)}}{\mathrm{d}s} = \frac{\partial}{\partial\gamma_K}\left(\frac{\mathrm{d}}{\mathrm{d}q_I}\left(\frac{1}{v}\right)\right), \quad \Longleftrightarrow \quad \frac{\mathrm{d}}{\mathrm{d}s}\mathsf{P} = -\frac{1}{v^2}\,V_{IJ}\,\frac{\partial q_J}{\partial\gamma_K}\,. \tag{2.46}$$

By also substituting the expression $\mathrm{d}s = v\,\mathrm{d}T$, a very common formulation for the dynamic ray tracing system in ray-centered coordinates can finally be received:

$$\frac{\mathrm{d}}{\mathrm{d}T}\begin{pmatrix}\mathsf{Q}\\ \mathsf{P}\end{pmatrix} = v\,\mathsf{W}^{(q)}\begin{pmatrix}\mathsf{Q}\\ \mathsf{P}\end{pmatrix}. \tag{2.47}$$

2.4.5 Ray propagator matrix in ray-centered coordinates

The reasonable way for the ray propagator matrix Π, briefly introduced in Section 2.3.2, to be still applicable in ray-centered coordinates is to transfer it in the same manner as it was done for the ray tracing systems above. Doing so will simplify the understanding of the formalism

and facilitate its use in my further derivations. Two points S and G situated on a central ray are introduced, as well as two points $S^{\perp}$ and $G^{\perp}$ located on the planes tangent to wavefronts placed at S and G, respectively.
The ray propagator matrix in ray-centered coordinates $\Pi^{(q)}$ linearly relates the phase-space coordinates of these four points. This can be initially written as

$$\begin{pmatrix} \vec{\mathsf{q}}(G^{\perp}) - \vec{\mathsf{q}}(G) \\ \vec{\mathsf{p}}^{(q)}(G^{\perp}) - \vec{\mathsf{p}}^{(q)}(G) \end{pmatrix} = \Pi^{(q)}(G,S) \begin{pmatrix} \vec{\mathsf{q}}(S^{\perp}) - \vec{\mathsf{q}}(S) \\ \vec{\mathsf{p}}^{(q)}(S^{\perp}) - \vec{\mathsf{p}}^{(q)}(S) \end{pmatrix}. \tag{2.48}$$

Each of the two-component location and slowness vectors are equal to zero along the central ray, therefore

$$\begin{pmatrix} \vec{\mathsf{q}}(G^{\perp}) \\ \vec{\mathsf{p}}^{(q)}(G^{\perp}) \end{pmatrix} = \Pi^{(q)}(G,S) \begin{pmatrix} \vec{\mathsf{q}}(S^{\perp}) \\ \vec{\mathsf{p}}^{(q)}(S^{\perp}) \end{pmatrix}. \tag{2.49}$$

Subsequently, I can further express relation (2.49) by incorporating similar derivatives with respect to ray coordinates γ_K as for the dynamic ray tracing system, leading to

$$\left.\begin{pmatrix} \frac{\partial q_I}{\partial \gamma_J} \\ \frac{\partial p_I^{(q)}}{\partial \gamma_J} \end{pmatrix}\right|_G = \underline{\Pi}^{(q)}(G,S) \left.\begin{pmatrix} \frac{\partial q_I}{\partial \gamma_J} \\ \frac{\partial p_I^{(q)}}{\partial \gamma_J} \end{pmatrix}\right|_S, \quad \Longleftrightarrow \quad \left.\begin{pmatrix} \mathsf{Q} \\ \mathsf{P} \end{pmatrix}\right|_G = \Pi^{(q)} \left.\begin{pmatrix} \mathsf{Q} \\ \mathsf{P} \end{pmatrix}\right|_S. \tag{2.50}$$

Finally, it is time to merge equations (2.47) and (2.50) into the so-called equation of the *dynamic evolution* of the ray propagator matrix in the ray-centered coordinate system. Keeping in mind that a resubstitution of $\mathrm{d}/\mathrm{d}T = v\,\mathrm{d}/\mathrm{d}s$ is carried out, it results in

$$\frac{\mathrm{d}}{\mathrm{d}s}\Pi^{(q)}(G,S) = \mathsf{W}^{(q)}\,\Pi^{(q)}(G,S). \tag{2.51}$$

Now I can introduce the ray propagator matrix $\Pi^{(q)}(T,T_0)$ with T corresponding to G and T_0 to S, respectively. For the case that the point G coincides with S the initial condition $T = T_0$ is met, which results in

$$\Pi^{(q)}(T_0,T_0) = \mathsf{I}, \tag{2.52}$$

where I is the 4×4 identity matrix.
Its common notation is based on a decomposition in four main components

$$\Pi^{(q)}(G,S) = \begin{pmatrix} \mathsf{Q}_1(G,S) & \mathsf{Q}_2(G,S) \\ \mathsf{P}_1(G,S) & \mathsf{P}_2(G,S) \end{pmatrix}. \tag{2.53}$$

The choice for those components to be named similar to the components of the dynamic ray tracing system is justified in case such a particular system is used in accordance with equation (2.51). Then, each pair of $\mathsf{Q}_i(G,S)$ and $\mathsf{P}_i(G,S)$ can be imagined as being a solution for a particular type of initial condition—of either point or plane-wave source, respectively.

- The submatrix $(\mathsf{Q}_1(G,S),\mathsf{P}_1(G,S))^T$ on the one hand is interpreted as the solution of system (2.47) with initial values at point S: $\mathsf{Q}=\mathsf{I}$ and $\mathsf{P}=\mathsf{0}$. This corresponds to a plane-wave source, since the slowness vector's direction is constant, thus its derivative equals to zero. The condition is commonly called the *normalized telescopic point/plane wavefront* initial condition.
- The submatrix $(\mathsf{Q}_2(G,S),\mathsf{P}_2(G,S))^T$ on the other hand is interpreted as the solution for initial values at point S: $\mathsf{Q}=\mathsf{0}$ and $\mathsf{P}=\mathsf{I}$, which corresponds to a *normalized point-source* initial condition, since the derivative of the source location vanishes.

2.4.6 The second derivative of traveltime in ray-centered coordinates

With the knowledge of parameters $\mathsf{Q}(s)$ and $\mathsf{P}(s)$ for all locations s along a central ray I can conveniently calculate several other useful quantities and additionally express their relevant differential equations in a well arranged way. Some examples are the matrix of curvature of a wavefront $\mathsf{K}(s)$, the geometrical spreading factor $\mathscr{L}(s)$, or the matrix of the second derivatives of the traveltime field $\mathsf{M}(s)$. The latter property plays a central role in the proceedings toward a general expression for describing wave propagation in the subsurface. Matrix $\mathsf{M}(s)$ is formulated alternatively by expanding its definition in the following way:

$$\mathsf{M}(s)=\frac{\partial^2 T}{\partial q_I\,\partial q_J}=\frac{\partial}{\partial q_I}\left(\frac{\partial T}{\partial q_J}\right)=\frac{\partial p_J^{(q)}}{\partial q_I}=\frac{\partial p_J^{(q)}}{\partial \gamma_K}\,\frac{\partial \gamma_K}{\partial q_I}=\mathsf{P}\,\mathsf{Q}^{-1}\,. \tag{2.54}$$

Its associated nonlinear differential equation of the Ricatti type is found through the derivative of M with respect to s and the dynamic ray tracing system (2.47), reading

$$\frac{\mathrm{d}\mathsf{M}}{\mathrm{d}s}=\frac{\mathrm{d}\mathsf{P}}{\mathrm{d}s}\,\mathsf{Q}^{-1}+\mathsf{P}\,\frac{\mathrm{d}\mathsf{Q}^{-1}}{\mathrm{d}s} \;=\; \frac{\mathrm{d}\mathsf{P}}{\mathrm{d}s}\,\mathsf{Q}^{-1}+\mathsf{P}\,\mathsf{Q}^{-1}\,\frac{\mathrm{d}\mathsf{Q}}{\mathrm{d}s}\,\mathsf{Q}^{-1}\,, \tag{2.55}$$

$$\frac{\mathrm{d}\mathsf{M}}{\mathrm{d}s} \;+\; v\,\mathsf{M}^2+v^{-2}\,\mathsf{V}=\mathsf{0}\,. \tag{2.56}$$

In order to obtain a solution $\mathsf{M}(G)$ at a particular point G along a central ray, one has to explicitly know about initial conditions at a given point S situated on the very same ray. Either the knowledge of $\mathsf{M}(S)$ or of its composites $\mathsf{Q}(S)$ and $\mathsf{P}(S)$ will suffice here.

2.4.7 Continuation relations and wavefront experiments

To find a solution in terms of its composites leads me to introduce the *continuation relations* for matrix M. They utilize the minors of the ray propagator matrix $\Pi^{(q)}(G,S)$ to calculate $\mathsf{M}(G)$

assuming $\mathsf{M}(S)$ is known. Firstly, I present the forward continuation for $\mathsf{Q}(G)$ and $\mathsf{P}(G)$ by repeating relation (2.50) in a slightly different notation:

$$\begin{aligned} \mathsf{Q}(G) &= \mathsf{Q}_1(G,S)\,\mathsf{Q}(S) + \mathsf{Q}_2(G,S)\,\mathsf{P}(S)\,, \\ \mathsf{P}(G) &= \mathsf{P}_1(G,S)\,\mathsf{Q}(S) + \mathsf{P}_2(G,S)\,\mathsf{P}(S)\,. \end{aligned} \tag{2.57}$$

The relation for the backward continuation follows from the chain rule of the ray propagator matrix and lets me determine $\mathsf{Q}(S)$ and $\mathsf{P}(S)$ from $\mathsf{Q}(G)$ and $\mathsf{P}(G)$:

$$\begin{aligned} \mathsf{Q}(S) &= \mathsf{P}_2^T(G,S)\,\mathsf{Q}(G) - \mathsf{Q}_2^T(G,S)\,\mathsf{P}(G)\,, \\ \mathsf{P}(S) &= -\mathsf{P}_1^T(G,S)\,\mathsf{Q}(G) + \mathsf{Q}_1^T(G,S)\,\mathsf{P}(G)\,. \end{aligned} \tag{2.58}$$

The forward and backward continuation for matrix M follow from expressions (2.57) and (2.58) using relation (2.54),

$$\begin{aligned} \mathsf{M}(G) &= \left[\mathsf{P}_1(G,S) + \mathsf{P}_2(G,S)\,\mathsf{M}(S)\right]\left[\mathsf{Q}_1(G,S) + \mathsf{Q}_2(G,S)\,\mathsf{M}(S)\right]^{-1}\,, \\ \mathsf{M}(S) &= \left[-\mathsf{P}_1^T(G,S) + \mathsf{Q}_1^T(G,S)\,\mathsf{M}(G)\right]\left[\mathsf{P}_2^T(G,S) - \mathsf{Q}_2^T(G,S)\,\mathsf{M}(G)\right]^{-1}\,. \end{aligned} \tag{2.59}$$

There exist simplified expressions of the above relations if I assume either a point source (PS), or a plane-wave/telescopic source (TS) at S or G, respectively. For instance, if I put a point source at point S the corresponding source matrix $\mathsf{M}(S)$ will approach infinity as $\mathsf{Q}(S)$ approaches zero. For a telescopic source placed at point G the source matrix $\mathsf{M}(G)$ will approach zero as $\mathsf{P}(G)$ approaches zero. Below I compiled the four possible forward and backward continuation relations for both types of sources. A thorough treatment of the whole subject with respect to far more complicated problems, e.g., delayed line sources, can be found in Červený (2001).

$$\begin{aligned} \mathsf{M}_{\mathrm{PS}}(G) &= \mathsf{P}_2(G,S)\,\mathsf{Q}_2^{-1}(G,S) = \mathsf{Q}_2^{-1T}(G,S)\,\mathsf{P}_2^T(G,S)\,, \\ \mathsf{M}_{\mathrm{PS}}(S) &= -\mathsf{Q}_1^T(G,S)\,\mathsf{Q}_2^{-1T}(G,S) = -\mathsf{Q}_2^{-1}(G,S)\,\mathsf{Q}_1(G,S)\,, \\ \mathsf{M}_{\mathrm{TS}}(G) &= \mathsf{P}_1(G,S)\,\mathsf{Q}_1^{-1}(G,S) = \mathsf{Q}_1^{-1T}(G,S)\,\mathsf{P}_1^T(G,S)\,, \\ \mathsf{M}_{\mathrm{TS}}(S) &= -\mathsf{P}_1^T(G,S)\,\mathsf{P}_2^{-1T}(G,S) = -\mathsf{P}_2^{-1}(G,S)\,\mathsf{P}_1(G,S)\,. \end{aligned} \tag{2.60}$$

The proof for each of the equations on the right-hand-sides of the above expressions is found—without providing any derivation—by adapting suitable invariants of the symplectic property of the ray propagator matrix. One can observe from looking at (2.60) that all four resulting matrices are symmetric.

An interesting question which arises from the previous investigations is concerning the description of all of the composites of the ray propagator matrix by means of the specific traveltime derivatives (2.60). They represent the two principal types of experiments, i.e., using point sources and plane-wave sources, which can be reproduced fairly easily by geophysical measurements. For the following I shall consider two point sources being placed at S and G. The

matrices $\mathsf{M}_{\mathrm{PS}}(G)$ and $\mathsf{M}_{\mathrm{PS}}(S)$ are determined from traveltime information close to G and S, respectively. Details on how to achieve this will be given in the next chapter. Furthermore, I require an experiment with a source which is different from a point source, e.g., generating a locally plane wavefront. I place it at S with the aim to determine the telescopic matrix $\mathsf{M}_{\mathrm{TS}}(G)$ from traveltime data in the vicinity of G.
Now I solve the three matching derivatives in the continuation relations (2.60) towards the non-inverse composites of the ray propagator matrix

$$\mathsf{P}_2 = \mathsf{M}_{\mathrm{PS}}(G)\,\mathsf{Q}_2\,, \qquad \mathsf{Q}_1 = -\mathsf{Q}_2\,\mathsf{M}_{\mathrm{PS}}(S)\,, \qquad \mathsf{P}_1 = \mathsf{M}_{\mathrm{TS}}(G)\,\mathsf{Q}_1\,. \tag{2.61}$$

Once more an invariant of the symplectic property of the ray propagator matrix is needed to derive a non-linear system of equations for Q_2 which will also be of particular interest for the discussion of chapter 3:

$$\mathsf{P}_2\,\mathsf{Q}_1^T - \mathsf{P}_1\,\mathsf{Q}_2^T = \mathsf{I}\,, \qquad \text{or} \qquad \mathsf{Q}_1\,\mathsf{P}_2^T - \mathsf{Q}_2\,\mathsf{P}_1^T = \mathsf{I}\,. \tag{2.62}$$

The system of equations is obtained by replacing all occurrences of P_2, Q_1, and P_1 with the substitutes originating from (2.61) and their transposed forms:

$$\begin{aligned} -\mathsf{M}_{\mathrm{PS}}(G)\,\mathsf{Q}_2\,\mathsf{M}_{\mathrm{PS}}^T(S)\,\mathsf{Q}_2^T &+ \mathsf{M}_{\mathrm{TS}}(G)\,\mathsf{Q}_2\,\mathsf{M}_{\mathrm{PS}}(S)\,\mathsf{Q}_2^T = \mathsf{I}\,, \\ \Longleftrightarrow \qquad \mathsf{Q}_2\,\mathsf{M}_{\mathrm{PS}}(S)\,\mathsf{Q}_2^T &= \left(\mathsf{M}_{\mathrm{TS}}(G) - \mathsf{M}_{\mathrm{PS}}(G)\right)^{-1}\,. \end{aligned} \tag{2.63}$$

The above system is solved best by using numerical and iterative schemes such as Newton's method for non-linear systems of equations. Unfortunately, system (2.63) is also underdetermined by one equation which means that I have to either introduce an additional wavefront experiment or the non-singularity of the *whole* ray propagator matrix, $\det|\Pi(G,S)| = 1$ in order to describe matrix Q_2 completely. Nevertheless, this result will be of further use in the discussion of the imaging workflows in chapter 3.

2.5 Calculation of paraxial traveltimes

Finally I can focus on the main objective of this chapter—the derivation of traveltime expression for the paraxial vicinity of a central ray Ω. There exist several ways to do this, the most common one is to use a Taylor expansion, which will be used here as well. Depending on the choice of the coordinate system, a traveltime approximation will assume a different form which consequently impacts on its usefulness in geophysical application.

It is obvious that once the matrix $\mathsf{M}(G)$ is determined for any given point $G \equiv [0,0,s_0]$ along a central ray it is possible to exactly compute its corresponding paraxial traveltimes. Any point

which lies on the plane which is perpendicular to Ω and passing through R qualifies for that. I can set up a simple quadratic expansion in the notation of the ray-centered coordinate system to read

$$T(q_1,q_2,s_0) = T(s_0) + \frac{1}{2}\vec{\mathsf{q}}^T\,\mathsf{M}(s_0)\,\vec{\mathsf{q}}\,, \quad \text{with} \quad \vec{\mathsf{q}} = (q_1,q_2)^T\,. \tag{2.64}$$

The drawbacks of this kind of expansion are the lack of an approximation along the arclength s but also the ray-centered coordinate system itself as it is inconvenient to handle. One by one, I now will explain on how to overcome these disadvantages.

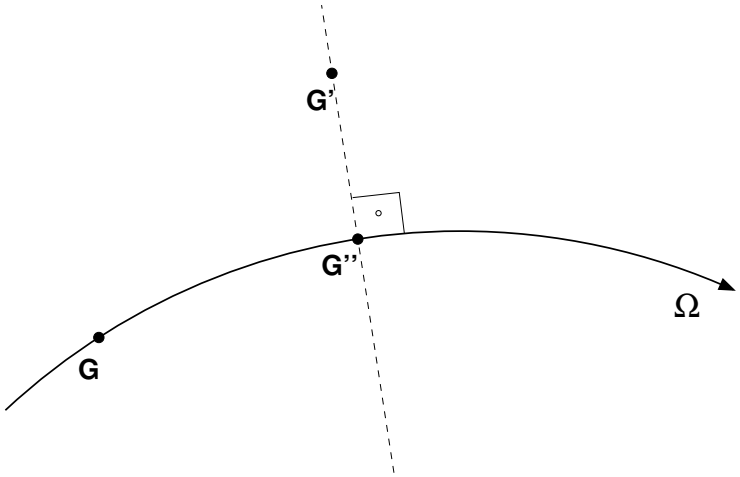

Figure 2.1: *Taylor expansion of paraxial traveltimes in the local vicinity of point G. Point G' is situated near G but does not necessarily have to lie on ray Ω. Point G'' specifies the intersection of Ω and the plane containing G' which is perpendicular to the ray.*

2.5.1 Paraxial traveltimes in ray-centered coordinates

The main disadvantage of the quadratic expansion (2.64) for a paraxial traveltime T is the lack of approximation in direction of the third coordinate $q_3 \equiv s$ of the ray-centered coordinate system. Yet, I still want to maintain the benefits of the dynamic ray tracing system being expressed in a very elegant form when utilizing these coordinates.
One way to overcome this problem is found by establishing a second order Taylor expansion approximating the traveltime that a wavefront takes to propagate from point G at $(0,0,s_0)^T$ to point G'' at $(0,0,s)^T$ along a central ray Ω. Figure (2.1) illustrates the situation. The approximation reads

$$T(G'') = T(G) + \left.\frac{\partial T}{\partial s}\right|_{s=s_0}(s-s_0) + \frac{1}{2}\left.\frac{\partial^2 T}{\partial^2 s}\right|_{s=s_0}(s-s_0)^2\,. \tag{2.65}$$

The two Taylor coefficients, i.e., the first and second derivatives of T with respect to s, are calculated by

$$\left.\frac{\partial T}{\partial s}\right|_{s=s_0} = \left.\frac{\mathrm{d}T}{\mathrm{d}s}\right|_{s=s_0} = v^{-1}(G)\,, \qquad \text{and} \qquad \left.\frac{\partial^2 T}{\partial^2 s}\right|_{s=s_0} = -v^{-2}(G)\,\left.\frac{\partial v}{\partial s}\right|_{s=s_0}\,. \tag{2.66}$$

The two traveltime expressions (2.64) and,(2.65), together with derivatives (2.66), are now combined to construct a local approximation for a point G' in the vicinity of G as indicated in Figure (2.1).

$$T(G') = T(G) + \frac{1}{v(G)}\,(s-s_0) + \frac{1}{2\,v^2(G)}\,\left.\frac{\partial v}{\partial s}\right|_G (s-s_0)^2 + \frac{1}{2}\,\mathsf{M}_{IJ}(G)\,q_I q_J\,, \quad I,J=1,2\,. \tag{2.67}$$

Even though, this expression is a helpful improvement it still lacks the ability of introducing pre-calculated derivatives with respect to a fixed coordinate system as here the derivatives are still taken with respect to an ever-changing central ray.

2.5.2 Transformation to local ray-centered Cartesian coordinates

As I showed, choosing ray-centered coordinates simplifies many ray-theoretical derivations considerably. However, practical applications usually demand in- and output in Cartesian coordinates. Therefore, the back-transformation to *local ray-centered Cartesian coordinates*, denoted with

$$\vec{\mathsf{y}} = (y_1, y_2, y_3)^T\,, \tag{2.68}$$

will be discussed in this section.
The difference between ray-centered coordinates and local ray-centered Cartesian coordinates is that $q_3 = s$ no longer is measured *along the ray* passing through origin G but *along the tangent to the ray* denoted by y_3 (see, Figure (2.2)). Denoting the position of any given point G' in the ray-centered coordinate system by (q_1, q_2, s), the radius vectors for the same point in both coordinate systems are constructed by

$$\vec{\mathsf{r}}(y_1, y_2, y_3) = \vec{\mathsf{r}}(G) + y_1\,\vec{\mathsf{e}}_1 + y_2\,\vec{\mathsf{e}}_2 + y_3\,\vec{\mathsf{e}}_3\,, \tag{2.69}$$

$$\vec{\mathsf{r}}(q_1, q_2, s) = \vec{\mathsf{r}}(0,0,s) + q_1\,\vec{\mathsf{e}}_1 + q_2\,\vec{\mathsf{e}}_2\,, \tag{2.70}$$

respectively, with $\vec{\mathsf{e}}_1, \vec{\mathsf{e}}_2$, and $\vec{\mathsf{e}}_3$ being Cartesian unit vectors.
In order to know how to transform the one coordinate system into the other, I take the total

differentials for both cases, which yields

$$\begin{aligned} \mathrm{d}\vec{r} &= \mathrm{d}y_1\,\vec{e}_1 + \mathrm{d}y_2\,\vec{e}_2 + \mathrm{d}y_3\,\vec{e}_3\,, && (2.71)\\ \mathrm{d}\vec{r} &= \left(\frac{\mathrm{d}}{\mathrm{d}s}\vec{q}(0,0,s) + q_1\frac{\mathrm{d}}{\mathrm{d}s}\vec{e}_1 + q_2\frac{\mathrm{d}}{\mathrm{d}s}\vec{e}_2\right) + \mathrm{d}q_1\,\vec{e}_1 + \mathrm{d}q_2\,\vec{e}_2 \\ &= \mathrm{d}q_1\,\vec{e}_1 + \mathrm{d}q_2\,\vec{e}_2 + \left(1 + \left(\frac{1}{v}\frac{\mathrm{d}v}{\mathrm{d}q_I}\right)\Big|_{q_I=0} q_I\right)\mathrm{d}s\,\vec{e}_3\,, \qquad I = 1,2\,. && (2.72) \end{aligned}$$

Comparing the coefficients of (2.71) and (2.72) leads to

$$\begin{aligned} \mathrm{d}y_1 &= \mathrm{d}q_1 \\ \mathrm{d}y_2 &= \mathrm{d}q_2 \\ \mathrm{d}y_3 &= \left(1 + \left(\frac{1}{v}\frac{\mathrm{d}v}{\mathrm{d}q_I}\right)\Big|_{q_I=0} q_I\right)\mathrm{d}s \equiv h\,\mathrm{d}s\,, && (2.73) \end{aligned}$$

with scale factor h being a substitute to indicate the relationship to an orthogonal *metric tensor*.

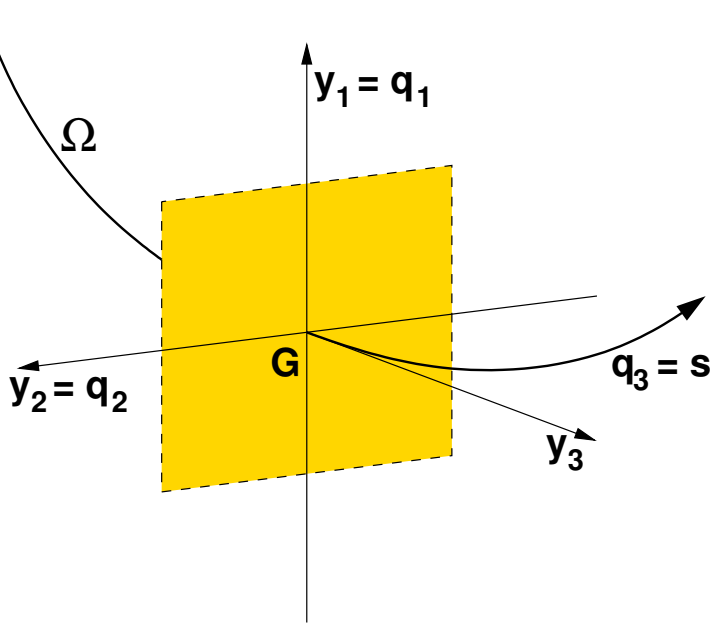

Figure 2.2: *Relationship between ray-centered coordinates and local ray-centered Cartesian coordinates. The q_1- and q_2-axes coincide with the y_1- and y_2-axes, respectively. The q_3-axis follows ray Ω, but the y_3-axis of the local ray-centered Cartesian coordinate system constructed at G coincides with the tangent to Ω at that point.*

2.5.3 Paraxial traveltimes in local ray-centered Cartesian coordinates

The calculation of traveltimes for arbitrary points situated on paraxial rays becomes much more convenient once I turn to the local ray-centered Cartesian coordinates. Considering the same situation as the one assumed for the derivation of expression (2.67) the Taylor expansion in direction of the arclength in local ray-centered Cartesian coordinates transforms via:

$$s - s_0 = h^{-1} y_3 \approx \left(1 - \frac{1}{v}\frac{\partial v}{\partial y_I} y_I\right) y_2\,, \qquad \text{and} \qquad (s-s_0)^2 \approx y_3^2\,, \quad I = 1,2\,. \tag{2.74}$$

The above approximations are now inserted in expression (2.67) which yields

$$\begin{aligned} T(G') &= T(G) + \frac{1}{v(G)} y_3 - \frac{1}{2\,v^2(G)}\frac{\partial v(G)}{\partial y_3} y_3^2 \\ &\quad - \frac{1}{v^2(G)}\frac{\partial v(G)}{\partial y_I} y_I y_3 + \frac{1}{2} M_{IJ}(G)\, y_I y_J\,, \quad I,J = 1,2\,. \end{aligned} \tag{2.75}$$

Formulated in a much more compact way by using the vector- and matrix-notation it reads

$$\begin{aligned} T(G') &= T(G) + \vec{\mathsf{y}}^T \cdot \vec{\mathsf{p}}^{(y)}(G) + \frac{1}{2}\vec{\mathsf{y}}^T\, \mathsf{M}^{(y)}(G)\, \vec{\mathsf{y}} \qquad (2.76) \\ &= T(G) + (y_1, y_2, y_3)\cdot(0,0,1/v(G))^T + \frac{1}{2}(y_1,y_2,y_3)\, \mathsf{M}^{(y)}(G)\, (y_1,y_2,y_3)^T\,, \end{aligned}$$

where

$$\mathsf{M}^{(y)}(G) = \begin{pmatrix} M_{11}(G) & M_{12}(G) & -(\frac{1}{v^2}\frac{\partial v}{\partial y_1})_G \\ M_{21}(G) & M_{22}(G) & -(\frac{1}{v^2}\frac{\partial v}{\partial y_2})_G \\ -(\frac{1}{v^2}\frac{\partial v}{\partial y_1})_G & -(\frac{1}{v^2}\frac{\partial v}{\partial y_2})_G & -(\frac{1}{v^2}\frac{\partial v}{\partial y_3})_G \end{pmatrix}. \tag{2.77}$$

2.5.4 Paraxial slowness vector

The paraxial slowness vector is the gradient of paraxial traveltime field $\vec{\mathsf{p}} = \vec{\nabla} T$, thus closely related to matrix M. I utilized it in my thesis to approximate the direction of polarization for different types of seismic waves as it will be explained in chapter 3.

As I already introduced the expressions of the paraxial traveltimes in different coordinate systems (see, e.g., (2.64), (2.67), and (2.75)) it is now easy to take their first spatial derivatives and compile the most important results here.

The quadratic expansion for $T(G') = T(q_1, q_2, s_0)$ reduces to a linear expansion for the ray-centered coordinate system

$$\vec{\mathsf{p}}^{(q)}(G') = \mathsf{M}(G)\,(q_1,q_2)^T\,, \quad \text{and} \quad p_3^{(q)}(G') = v^{-1}(G)\,. \tag{2.78}$$

For the Taylor expansion (2.75) of $T(G') = T(y_1, y_2, y_3)$ in the local ray-centered Cartesian coordinate system the first derivative can be written as

$$\vec{\mathsf{p}}^{(y)}(G') = \vec{\mathsf{p}}^{(y)}(G) + \mathsf{M}^{(y)}(G)\,(y_1, y_2, y_3)^T\,. \tag{2.79}$$

Then again, I can express the traveltime field in terms of the paraxial slowness vector, which will prove useful in the next section. Again I shall state the result for both the ray-centered and the local ray-centered Cartesian coordinate system:

$$T(G') = T(G) + \frac{1}{2}\vec{\mathsf{q}}^T(G') \cdot \vec{\mathsf{p}}^{(q)}(G')\,, \quad \text{for} \quad G' \in \Sigma^\perp\,, \tag{2.80}$$

$$T(G') = T(G) + \frac{1}{2}\vec{\mathsf{y}}^T(G') \cdot \left(\vec{\mathsf{p}}^{(y)}(G') + \vec{\mathsf{p}}^{(y)}(G)\right)\,. \tag{2.81}$$

Note that $\Sigma^\perp$ refers to a plane perpendicular to a central ray which intersects it in G.

2.5.5 Two-point eikonal equation

The so-called *two-point eikonal* is introduced in order to describe the traveltime difference between an arbitrary paraxial ray Ω' and a given central ray Ω. Two points S' and G' are chosen on the paraxial ray indicating its starting and ending positions. The central ray's respective points S and G are assumed to lie in their vicinity.
Additionally, it is necessary to introduce the points $S^\perp$ and $G^\perp$. They are found by constructing two local ray-centered Cartesian coordinate systems at either end of Ω and projecting the primed paraxial points into the respective plane $\Sigma^\perp$ of each system.
The coordinates of points $S^\perp$ and $G^\perp$ in the ray-centered coordinate system are specified by $\vec{\mathsf{q}}(S^\perp) = (q_1(S^\perp), q_2(S^\perp))^T$ and $\vec{\mathsf{q}}(G^\perp) = (q_1(G^\perp), q_2(G^\perp))^T$. Consequently, one now can express the positions of points S' and G' in local ray-centered Cartesian coordinates by

$$\vec{\mathsf{y}}(S') = \begin{pmatrix} y_1(S') \\ y_2(S') \\ y_3(S') \end{pmatrix} = \begin{pmatrix} q_1(S^\perp) \\ q_2(S^\perp) \\ y_3(S') \end{pmatrix}, \quad \vec{\mathsf{y}}(G') = \begin{pmatrix} y_1(G') \\ y_2(G') \\ y_3(G') \end{pmatrix} = \begin{pmatrix} q_1(G^\perp) \\ q_2(G^\perp) \\ y_3(G') \end{pmatrix}. \tag{2.82}$$

Now I wish to express not only the traveltime from S' to G' but also the corresponding slowness vectors $\vec{\mathsf{p}}^{(y)}(S')$ and $\vec{\mathsf{p}}^{(y)}(G')$ for each paraxial ray Ω'.
By using relation (2.79) and by decomposing matrix $\mathsf{M}^{(y)}(G)$ for a point G defined in expression (2.77) into derivatives of traveltime and velocity field, I can write

$$p_i^{(y)}(G') = p_i^{(y)}(G) + \delta_{iK}\,\mathsf{M}_{KJ}^{(y)}(G)\,y_J(G') + \hat{\mathsf{M}}_{ij}^{(y)}(G)\,y_j(G')\,. \tag{2.83}$$

Here matrix $\hat{\mathsf{M}}_{KJ}^{(y)}$ stands for $\hat{\mathsf{M}}_{IJ}^{(y)} = 0$, $\hat{\mathsf{M}}_{3j}^{(y)} = \mathsf{M}_{3j}^{(y)}$, and $\hat{\mathsf{M}}_{j3}^{(y)} = \mathsf{M}_{j3}^{(y)}$. Kronecker delta δ_{iK} ($i = 1,2,3$; $K = 1,2$) has the conventional meaning.

Again, I have to return to the ray propagator matrix in ray-centered coordinates $\Pi^{(q)}$, as its formalism now is being used to relate the two points of the traveltime eikonal. This time I consider wavefronts propagating from $S^{\perp}$ to $G^{\perp}$ and also vice versa. It is important to remind the reader that a change of the propagation direction along the ray also changes the properties of the ray propagator matrix. I begin from relation (2.49) for the slowness vector in ray-centered coordinates using some basic algebra and the symplectic property of $\Pi^{(q)}$ to derive the following

$$\begin{aligned} \vec{\mathsf{q}}(G^{\perp}) &= \mathsf{Q}_1\,\vec{\mathsf{q}}(S^{\perp}) + \mathsf{Q}_2\,\vec{\mathsf{p}}^{(q)}(S^{\perp}) \\ \Longleftrightarrow\quad \vec{\mathsf{p}}^{(q)}(S^{\perp}) &= \mathsf{Q}_2^{-1}\,\vec{\mathsf{q}}(G^{\perp}) - \mathsf{Q}_2^{-1}\,\mathsf{Q}_1\,\vec{\mathsf{q}}(S^{\perp}) \end{aligned} \tag{2.84}$$

$$\begin{aligned} \vec{\mathsf{p}}^{(q)}(G^{\perp}) &= \mathsf{P}_1\,\vec{\mathsf{q}}(S^{\perp}) + \mathsf{P}_2\,\vec{\mathsf{p}}^{(q)}(S^{\perp}) \\ \underbrace{\Longrightarrow}_{(2.84)}\quad \vec{\mathsf{p}}^{(q)}(G^{\perp}) &= (\mathsf{P}_1 - \mathsf{P}_2\,\mathsf{Q}_2^{-1}\,\mathsf{Q}_1)\,\vec{\mathsf{q}}(S^{\perp}) + \mathsf{P}_2\,\mathsf{Q}_2^{-1}\,\vec{\mathsf{q}}(G^{\perp}) \end{aligned} \tag{2.85}$$

$$\vec{\mathsf{p}}^{(q)}(S^{\perp}) = -\mathsf{Q}_2^{-1}\,\mathsf{Q}_1\,\vec{\mathsf{q}}(S^{\perp}) + \mathsf{Q}_2^{-1}\,\vec{\mathsf{q}}(G^{\perp}) \tag{2.86}$$

$$\vec{\mathsf{p}}^{(q)}(G^{\perp}) = -\mathsf{Q}_2^{-1T}\,\vec{\mathsf{q}}(S^{\perp}) + \mathsf{P}_2\,\mathsf{Q}_2^{-1}\,\vec{\mathsf{q}}(G^{\perp}) \tag{2.87}$$

Looking back at the information I gathered concerning ray propagator matrices, the interpretation for the right column of $\Pi^{(q)}$ as an initial point source proves to be particularly useful.
For equation (2.86) I assume a point source at G which lets me introduce $\mathsf{M}_{\mathrm{PS}}(G)$. An analog treatment is given to equation (2.87) by placing the point source at S which results in the appearance of $\mathsf{M}_{\mathrm{PS}}(S)$

$$\vec{\mathsf{p}}^{(q)}(S^{\perp}) = \mathsf{M}_{\mathrm{PS}}(G)\,\vec{\mathsf{q}}(S^{\perp}) + \mathsf{Q}_2^{-1}\,\vec{\mathsf{q}}(G^{\perp}), \qquad \vec{\mathsf{p}}^{(q)}(G^{\perp}) = -\mathsf{Q}_2^{-1T}\,\vec{\mathsf{q}}(S^{\perp}) + \mathsf{M}_{\mathrm{PS}}(S)\,\vec{\mathsf{q}}(G^{\perp}). \tag{2.88}$$

Considering this, a preliminary version of the two-point eikonal can be stated with the help of the traveltime approximation in terms of the paraxial slowness vector (2.81) being applied for either end of the paraxial ray:

$$\begin{aligned} T(G',S') &= \Delta T(G',G) - \Delta T(S',S) = \Big(T(G') - T(G)\Big) - \Big(T(S') - T(S)\Big) \\ &= T(G,S) + \frac{1}{2}\vec{\mathsf{y}}^{T}(G')\cdot\Big(\vec{\mathsf{p}}^{(y)}(G') + \vec{\mathsf{p}}^{(y)}(G)\Big) - \frac{1}{2}\vec{\mathsf{y}}^{T}(S')\cdot\Big(\vec{\mathsf{p}}^{(y)}(S') + \vec{\mathsf{p}}^{(y)}(S)\Big). \end{aligned} \tag{2.89}$$

Now I can insert decomposition (2.83) into the above approximation with the implicit consideration of the first two components of (2.79) to be $\mathsf{M}^{(y)}_{KJ}(G')\,y_J = p^{(q)}_K(G')$—the same applies to point S', respectively. In a second step an additional substitution using the ray-propagator nota-

tion from (2.88) is carried out which yields

$$\begin{aligned} T(G',S') &= T(G,S)+y_i(G')\,p_i^{(y)}(G)-y_i(S')\,p_i^{(y)}(S) \\ &\quad +\frac{1}{2}y_i(G')\left(\delta_{iK}\,\mathsf{M}_{KJ}^{(y)}(G)\,y_J(G')+\hat{\mathsf{M}}_{ij}^{(y)}(G)\,y_j(G')\right) \\ &\quad -\frac{1}{2}y_i(S')\left(\delta_{iK}\,\mathsf{M}_{KJ}^{(y)}(S)\,y_J(S')+\hat{\mathsf{M}}_{ij}^{(y)}(S)\,y_j(S')\right) \\ &= T(G,S)+y_i(G')\,p_i^{(y)}(G)-y_i(S')\,p_i^{(y)}(S) \\ &\quad +\frac{1}{2}y_i(G')\left(\delta_{iK}\left\{(\mathsf{M}_{\mathrm{PS}}(S))_{KJ}\,y_J(G')-\left(\mathsf{Q}_2^{-1}\right)_{JK}y_J(S')\right\}+\hat{\mathsf{M}}_{ij}^{(y)}(G)\,y_j(G')\right) \\ &\quad -\frac{1}{2}y_i(S')\left(\delta_{iK}\left\{(\mathsf{M}_{\mathrm{PS}}(G))_{KJ}\,y_J(S')+\left(\mathsf{Q}_2^{-1}\right)_{KJ}y_J(G')\right\}+\hat{\mathsf{M}}_{ij}^{(y)}(S)\,y_j(S')\right). \end{aligned} \tag{2.90}$$

The decomposition of matrix $\mathsf{M}^{(y)}$ can be reversed now as it has been calibrated to the initial condition of a point source at both S and G. Therefore, I now can write (2.90) in full matrix notation after collecting the terms with Q_2^{-1} in another 3×3 matrix by considering the symplectic property:

$$\begin{aligned} T(G',S') &= T(G,S)+\vec{\mathsf{y}}(G')\cdot\vec{\mathsf{p}}^{(y)}(G)-\vec{\mathsf{y}}(S')\cdot\vec{\mathsf{p}}^{(y)}(S) \\ &\quad +\frac{1}{2}\,\vec{\mathsf{y}}^{T}(G')\cdot\mathsf{M}^{(y)}(G,S)\cdot\vec{\mathsf{y}}(G')-\frac{1}{2}\,\vec{\mathsf{y}}^{T}(S')\cdot\mathsf{M}^{(y)}(S,G)\cdot\vec{\mathsf{y}}(S') \\ &\quad -\vec{\mathsf{y}}^{T}(S')\cdot\mathsf{G}^{(y)}(G,S)\cdot\vec{\mathsf{y}}(G'), \end{aligned} \tag{2.91}$$

where three matrices $\mathsf{M}^{(y)}(G,S)$, $\mathsf{M}^{(y)}(S,G)$, and $\mathsf{G}^{(y)}(G,S)$ are given by

$$\mathsf{M}^{(y)}(G,S)=-\begin{pmatrix} -\mathsf{M}_{\mathrm{PS}}(S) & \left(\frac{1}{v^2}\frac{\partial v}{\partial y_1}\right)_G \\ & \left(\frac{1}{v^2}\frac{\partial v}{\partial y_2}\right)_G \\ \left(\frac{1}{v^2}\frac{\partial v}{\partial y_1}\right)_G \quad \left(\frac{1}{v^2}\frac{\partial v}{\partial y_2}\right)_G & \left(\frac{1}{v^2}\frac{\partial v}{\partial y_3}\right)_G \end{pmatrix}, \qquad \mathsf{G}^{(y)}(G,S)=\begin{pmatrix} \mathsf{Q}_2^{-1} & 0 \\ & 0 \\ 0\quad 0 & 0 \end{pmatrix},$$

$$\mathsf{M}^{(y)}(S,G)=-\begin{pmatrix} -\mathsf{M}_{\mathrm{PS}}(G) & \left(\frac{1}{v^2}\frac{\partial v}{\partial y_1}\right)_S \\ & \left(\frac{1}{v^2}\frac{\partial v}{\partial y_2}\right)_S \\ \left(\frac{1}{v^2}\frac{\partial v}{\partial y_1}\right)_S \quad \left(\frac{1}{v^2}\frac{\partial v}{\partial y_2}\right)_S & \left(\frac{1}{v^2}\frac{\partial v}{\partial y_3}\right)_S \end{pmatrix}. \tag{2.92}$$

2.6 Transformation to general Cartesian coordinates

The final step I want to apply is the transformation of traveltime formulation (2.91) into a general Cartesian coordinate system placed at both S and G with the x_3-axis pointing in depth direction.

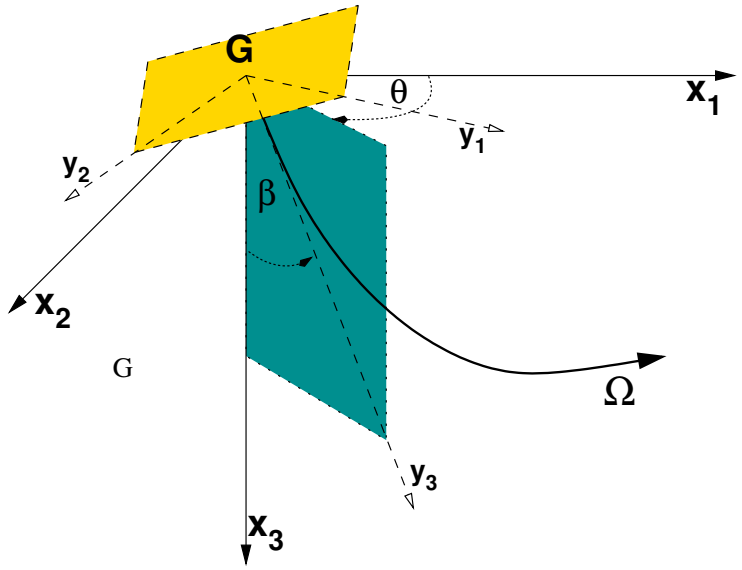

Figure 2.3: *Relationship between general Cartesian coordinates and local ray-centered Cartesian coordinates. The origins of both systems coincide at point G. The y_1- and y_2-axis of the local ray-centered Cartesian system lie on a plane (yellow) which is perpendicular to the tangent of central ray Ω and passing through G. A rotation by angle θ will align the projection of the y_1- and y_2-axis, into the x_1x_2-plane of the general Cartesian system perfectly with the respective x-axes. The residual tilt of both systems is overcome with a subsequent rotation by angle β.*

I denote the Cartesian coordinates of the points under consideration by

$$\vec{\mathrm{x}}(G',G) = \begin{pmatrix} x_1(G') - x_1(G) \\ x_2(G') - x_2(G) \\ x_3(G') - x_3(G) \end{pmatrix}, \qquad \text{and} \qquad \vec{\mathrm{x}}(S',S) = \begin{pmatrix} x_1(S') - x_1(S) \\ x_2(S') - x_2(S) \\ x_3(S') - x_3(S) \end{pmatrix}. \tag{2.93}$$

In order to reach the local ray-centered Cartesian coordinates by means of the general Cartesian coordinates, I rotate its system's axes by two emergence angles. One angle named β is measured with respect to the depth axis, the other one, called θ, indicates the azimuthal direction measured with respect to the x_1-axis.
Altogether, for each central ray under consideration, one will have to specify two times two angles at either end of the ray which are denoted by β_S and β_G for vertical and θ_S and θ_G for azimuthal emergence angles. Similar to the convention of polar coordinates they are measured positively in counterclock-wise direction as indicated in Figure (2.3).

The rules for the transformation are simple linear multiplications with cascaded rotation matrices

which read

$$\vec{\mathsf{y}}(G') = \mathsf{D}(G)\vec{\mathsf{x}}(G',G) \qquad \text{and} \qquad \vec{\mathsf{y}}(S') = \mathsf{D}(S)\vec{\mathsf{x}}(S',S)\,, \tag{2.94}$$

with

$$\mathsf{D}(P) = \begin{pmatrix} \cos\theta_P \cos\beta_P & \sin\theta_P \cos\beta_P & -\sin\beta_P \\ -\sin\theta_P & \cos\theta_P & 0 \\ \cos\theta_P \sin\beta_P & \sin\theta_P \sin\beta_P & \cos\beta_P \end{pmatrix}, \qquad \text{for} \qquad P = S, G\,. \tag{2.95}$$

Substituting the transformations (2.94) into traveltime equation (2.91) yields the final expression

$$\begin{aligned} T(G',S') \;=\; & T(G,S) + \vec{\mathsf{x}}^T(G',G)\,\mathsf{D}^T(G)\cdot\vec{\mathsf{p}}^{(y)}(G) - \vec{\mathsf{x}}^T(S',S)\,\mathsf{D}^T(S)\cdot\vec{\mathsf{p}}^{(y)}(S) \\ & + \frac{1}{2}\,\vec{\mathsf{x}}^T(G',G)\,\mathsf{D}^T(G)\mathsf{M}^{(y)}(G,S)\,\mathsf{D}(G)\vec{\mathsf{x}}(G',G) \\ & + \frac{1}{2}\,\vec{\mathsf{x}}^T(S',S)\,\mathsf{D}^T(S)\mathsf{M}^{(y)}(S,G)\,\mathsf{D}(S)\vec{\mathsf{x}}(S',S) \\ & - \vec{\mathsf{x}}^T(S',S)\,\mathsf{D}^T(S)\,\mathsf{G}^{(y)}(G,S)\,\mathsf{D}(G)\vec{\mathsf{x}}(G',G)\,. \end{aligned} \tag{2.96}$$

Statement (2.96) is commonly called a *parabolic* traveltime approximation because a parabolic hypersurface in multidimensional space is shaped by it. For a better approximation of the paraxial traveltime—in terms of stability during coherence analysis—Ursin (1982) suggested after systematic investigations that in most cases a *hyperbolic* traveltime formula is more suitable. This was also confirmed by Müller (1999) and Jäger (1999).
Therefore, I consistently instrumented the hyperbolic traveltime expansion for the developed seismic data processing scheme. The parabolic expansion was solely used for the derivations of paraxial slowness vectors. By taking the square on both sides of equation (2.96) and keeping only terms up to the second order, I obtain the hyperbolic expansion:

$$\begin{aligned} T^2(G',S') \;=\; & \Big(T(G,S) + \vec{\mathsf{x}}^T(G',G)\,\mathsf{D}^T(G)\cdot\vec{\mathsf{p}}^{(y)}(G) - \vec{\mathsf{x}}^T(S',S)\,\mathsf{D}^T(S)\cdot\vec{\mathsf{p}}^{(y)}(S)\Big)^2 \\ & + T(G,S)\,\vec{\mathsf{x}}^T(G',G)\,\mathsf{D}^T(G)\mathsf{M}^{(y)}(G,S)\,\mathsf{D}(G)\vec{\mathsf{x}}(G',G) \\ & + T(G,S)\,\vec{\mathsf{x}}^T(S',S)\,\mathsf{D}^T(S)\mathsf{M}^{(y)}(S,G)\,\mathsf{D}(S)\vec{\mathsf{x}}(S',S) \\ & - 2\,T(G,S)\,\vec{\mathsf{x}}^T(S',S)\,\mathsf{D}^T(S)\,\mathsf{G}^{(y)}(G,S)\,\mathsf{D}(G)\vec{\mathsf{x}}(G',G)\,. \end{aligned} \tag{2.97}$$

Chapter 3

Implementation

This chapter is dedicated to the introduction of two CRS-stacking operators derived on the basis of expressions (2.96) and (2.97). The focus will be put on issues of workflow design for the stacking procedure and for the handling of multicomponent data assuming wave propagation in 2D depth-slices.

A very general CRS-stacking-operator for three dimensional wave propagation not being limited to any particular geometry of seismic measurement will be the starting point for more specialized subsets to be derived for thorough inspection. One subset is the 2D CO CRS operator for arbitrary acquisition geometries which will be the final form used in my thesis. Two possible workflows based on coherence analysis warranting a stable determination of the necessary stacking parameters are introduced. The relevance of the paraxial slowness vector for the purpose of wavefield separation of multicomponent data is pointed out and the requirement of an extended coherence criterion for that case.

A short coverage on the special case of 3D vertical seismic profiling geometries will conclude the chapter where a special transformation which accounts for monotonously curved wells is presented. The associated discussion aims at an extrapolation of the presently more focused implementation towards future development in a broader spectrum.

3.1 Introduction

With the formulas (2.97) and (2.96) I have derived the most general paraxial traveltime expression conceivable in terms of a second-order approximation. In Hertweck et al. (2007) a very illustrative interpretation of the functionality of CRS operators is given, making use of the redun-

dancy which can be found in seismic data. The work by Yang et al. (2005) finds an equivalence of the response of Kirchhoff *migration-to-zero-offset* (MZO)—when extended to local segments which approximate the subsurface reflectors—to the response of CRS operators.
Depending on the various problem definitions in today's seismic imaging several specialized subsets of this *stacking operator* or *moveout formula* have been investigated as working with the full form despite the highly increased computational capacity still can be considered unfeasible. Examples for specialized stacking operators and the corresponding challenging tasks are:

- **2D & 3D ZO CRS imaging:** The term *zero offset* indicates the close relation to all imaging processes which try to simulate an experiment where source and receiver position coincide. Much alike to, e.g., the NMO/DMO approach a final result of the analysis is a stacked image in the time domain but with a much higher signal-to-noise ratio.
  There exist numerous applications of the CRS operator aiming at the improvement of image quality especially for low-coverage data or data contaminated by background noise (see, one recent example by Frehers et al., 2007). One benefit of the method being the additional number of contributing traces during an analysis helps to compensate these problems and to increase the reliability of stacking results. Another particular specialized operator was developed in order to handle the additional complications of a strong top-surface topography (see Zhang and Wu, 2004, for a case study on synthetic data).

- **Use of 2D & 3D ZO CRS attributes:** The stacking parameters obtained by the data-driven analysis with any of the ZO CRS methods can be converted to resemble physical properties of a hypothetical one-way wave propagation experiment. These properties serve as an input perfectly suited for the subsequent estimation of velocity-depth models by means of tomographic inversion as presented by Duveneck (2004).
  The attributes can further be utilized in the context of quality control where event-consistent picking across reflection events or accurate approximations for aperture sizes are required. For suggested reading on these subjects I refer to Klüver (2007) and Müller (2007).

- **2D CO CRS imaging:** The *common offset* imaging by means of CRS operators also has been investigated to a certain extent with the emphasis being placed on the application to surface seismic data. One advantage of choosing a larger offset in the simulated measurement configuration lies in the possibility to *undershoot* obstacles which hinder any direct ray path being taken (see, e.g., Bergler et al., 2002b).
  Data regularization also can matter a great deal especially where *true amplitude* imaging is required. Gaps in the shot and receiver distribution despite of a good survey design are a commonly encountered nuissance being compensated by interpolating missing traces using neighboring traces in their paraxial vicinity. This subject has been elaborated by Höcht and Ricarte (2006).

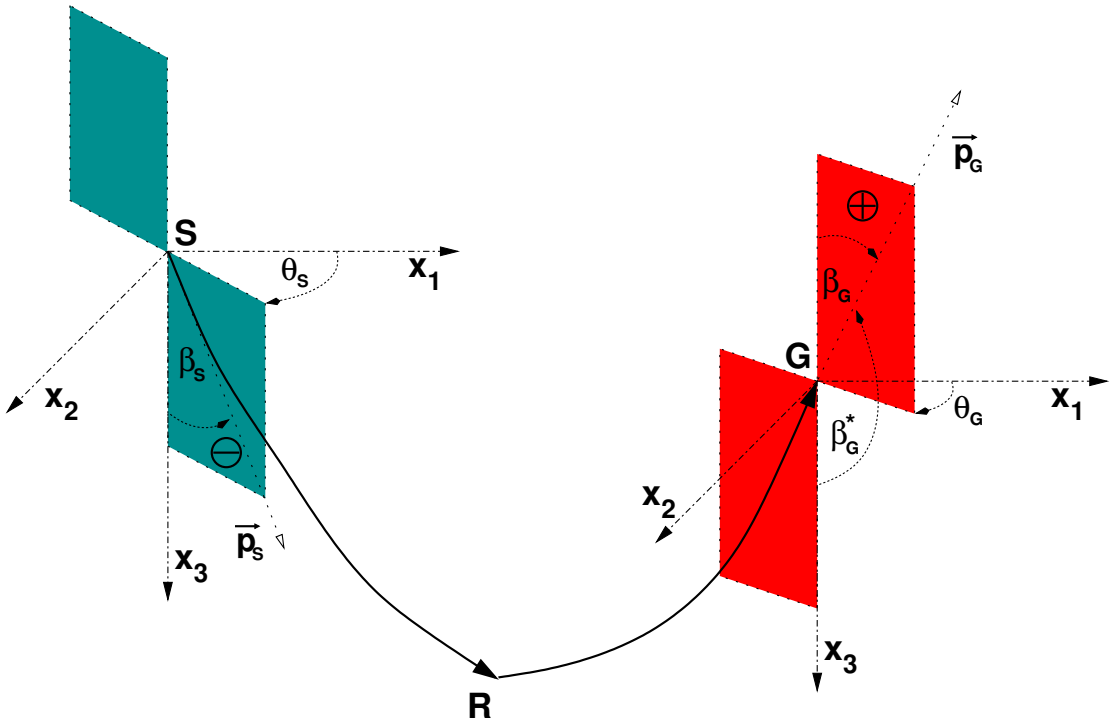

Figure 3.1: *Sign convention for slowness vectors.*

An alternative treatment of acquisition geometries apart from surface seismic settings by the CRS method with emphasis being placed on multicomponent data has also been verified. Furthermore, an investigation over the CO CRS attributes to be utilized to discriminate the wavefield of each individual wavemode was conducted (most recent contribution by Boelsen and Mann, 2005).

As one can observe from the above classification up to this date and to my knowledge there exists no particular coverage of a 3D CO CRS imaging scheme in application for the obvious reason of computational efficiency. The following section is dedicated to the theoretical description of the most general CRS operator which will lead to my presentation of workflow serving as a complete treatment for planar wave-propagation problems. Towards the end of this chapter I attempt to provide some practical considerations for this most general case by reverting to the lessons learned during my investigations.

3.2 Examples of CRS operators for VSP surveys

An important issue I have to firstly address is the convention by which angles of emergence and incidence for a given central ray and its paraxial neighbors are measured. For three-dimensional wave propagation the representation by a elevation angle β and an azimuth angle θ in accordance with the mathematical definition of the spherical coordinate system has been chosen with the same numerical ranges. Hereby, each individual ray is initially represented by two angles at either of its ends S and G.
In order to keep the connection to angle definitions of earlier publications which were mainly dealing with planar wave propagation proper adjustments in the trigonometric functions became necessary while moving from expressions (2.97) and (2.96) to the general form of a 3D CO CRS operator. Elevation angles β_S and β_G for reflected or converted waves are generally measured as acute angles ($< \pi/2$) at source and receiver while transmitted waves are measured as obtuse unless a turning wave is encountered.
The slowness vector at S will be pointing into the subsurface while its counterpart at G will point away from it. A sign-convention is enforced in such a way that β_S will assume negative and β_G positive values under the condition of a positive offset h:

- *Planar wave propagation* is assumed to remain within the plane from which its underlying 2.5D medium was derived and is not to confuse with *plane wave propagation*, describing a specific type of wave. In this way, for wave propagation within the plane which also contains the line of acquisition the signed half-offset $h = 1/2(x_G - x_S)$ determines whether signs of the elevation angles are reversed.

- Generally, in 3D wave propagation the Euclidian offset $h = 1/2|\vec{\mathrm{x}}_G - \vec{\mathrm{x}}_S|$ remains positive by definition and the azimuthal angles θ_S and θ_G will be responsible for any additional complication.

Figure 3.1 illustrates all the angular conventions described previously compiled in one sketch.
The sign convention for propagating wavefronts as emerging from the ray-propagator formalism is also kept in accordance with older publications (see, e.g. Hubral and Krey, 1980): the curvature of a wavefront that lags behind its tangent plane is defined as positive, while the curvature of a wavefront that is ahead of its tangent plane is defined as negative. Both observations are made by looking in propagation direction along the ray under consideration. For the scope of this thesis the further use of CRS wavefront curvatures remains somewhat limited which leads me to keep the notation in terms of $\mathsf{M}^{(y)}(G,S)$, $\mathsf{M}^{(y)}(S,G)$, and Q_2^{-1}. A particular conversion towards wavefront curvatures, i.e., CRS attributes, for the 2D case can be found in section 3.4.

The 3D CO CRS operator for topography including the above angular conventions but without replacing the second derivatives of traveltime by CRS curvatures can be found in appendix A.1 and will not be discussed in extensive detail. The consideration of the local linear velocity gradient at either source or receiver side has been omitted for this case as I regard this to be an additional complication where the unfamiliarity to the operator itself would be sufficient, already. Note that expression (A.1) is shown in the parabolic expansion and has been factorized to reduce the amount of individual terms. The number of stacking parameters in this formula is fourteen which can ultimately be decomposed into three spatial wavefront curvatures and four angular directions. Thus the number of recovered CRS attributes will reduce to thirteen independent properties once the continuation relations are applied as described in section 2.4.7.
Another operator which will only be of minor concern is compiled in appendix A.2. The 2D CO CRS operator for topography considering one component of linear velocity gradient at the receiver side is a very specialized construct, yet can be found useful under certain circumstances, e.g., working as a data-driven filter. I will explain this issue in more detail in chapter 5.

3.2.1 3D CO CRS operator for deviated wells

Furthermore, specialization can be a useful strategy for obtaining a simplified solution scheme when I now turn from general 3D surveys towards the particular case of seismic measurements involving borehole geometries. The following section still involves a more general hypothetical traveltime operator and serves the purpose of a theoretical outlook—as it has not been implemented or tested yet—but algorithms developed for the much more limited 2D case can be transfered here with little additional work. A similar approach has been chosen by Chira and Hubral (2003) in order to simplify the 2D CRS traveltime operator for zero offset under the presence of topography.

Generally, once a well is brought down into the subsurface there will be a very accurate estimation of the trajectory along which the drilling was carried out. For most cases the trajectory follows a monotonous curve and in any other case it can be implied that surveys can still be subdivided into smaller segments to satisfy that condition. Figure 3.2 shows a borehole trajectory passing through an expansion point G for which a local Cartesian coordinate system is constructed which is much alike to a local ray-centered Cartesian coordinate system introduced previously. Its axis $\vec{g}_3$ aligns with the tangent to the trajectory while $\vec{g}_1$ is found in the plane composed by $\vec{g}_3$ and $\vec{x}_3$ and axis $\vec{g}_2$ aligns with the normal vector of that plane. As a result of this transformation two local angles α_G and γ_G are determined and a new monotonous coordinate Δg is assigned to all points $G^\star$ within a certain vicinity of G which will be referred-to as the *paraxial aperture* of the receiver-side. This is done by projecting $\vec{y}(G^\star)$ down on $\vec{g}_3$ for all points which

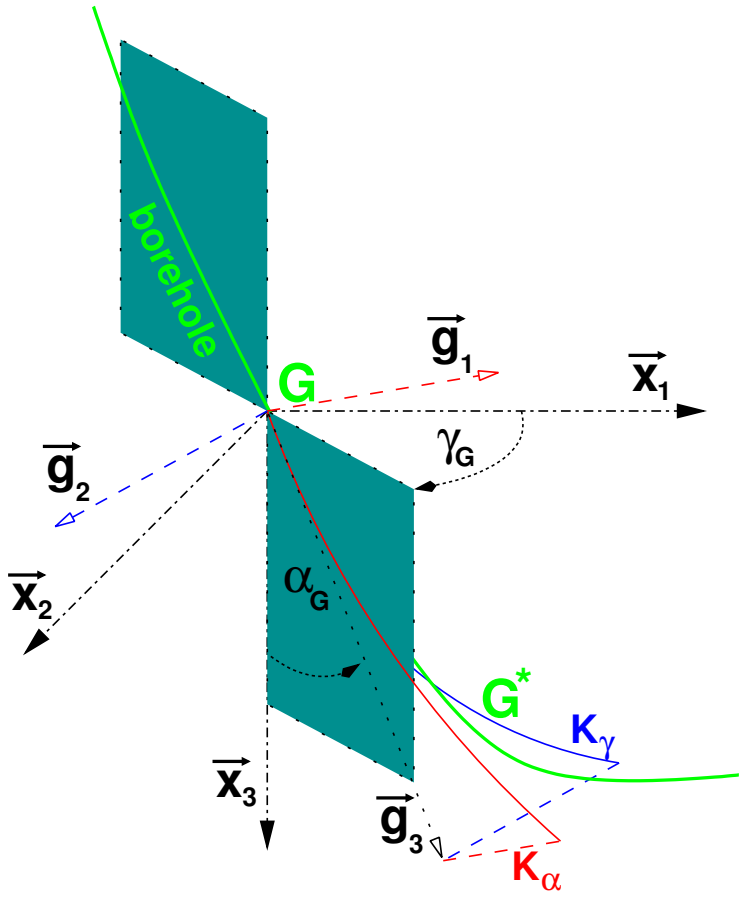

Figure 3.2: *Projection of neighboring receiver levels to a monotonous coordinate and subsequent approximation by a parabolic curve in two directions.*

---

will contribute to subsequent analysis algorithms with respect to G.
The next step involves the determination of two coefficients K_α and K_γ using nonlinear regression which will locally approximate the trajectory by a parabolic curve in both directions. It can be considered to perform this fitting-procedure individually for both sides of the trajectory. Even though this would render the resulting traveltime surface to be no longer differentiable in G one should expect to obtain more reliable stacking parameters in case of inflection points along the trajectory.

The transformation between the displacement vector $\Delta\vec{x}$ and its approximation through Δg is

achieved by chaining two rotation matrices which yields

$$\begin{pmatrix} \Delta x_G \\ \Delta y_G \\ \Delta z_G \end{pmatrix} \approx \begin{pmatrix} \cos\gamma_G \cos\alpha_G & \sin\gamma_G \cos\alpha_G & -\sin\alpha_G \\ -\sin\gamma_G & \cos\gamma_G & 0 \\ \cos\gamma_G \sin\alpha_G & \sin\gamma_G \sin\alpha_G & \cos\alpha_G \end{pmatrix} \begin{pmatrix} \frac{1}{2}K_\alpha \Delta g^2 \\ \frac{1}{2}K_\gamma \Delta g^2 \\ \Delta g \end{pmatrix}. \tag{3.1}$$

If I insert (3.1 into expression (A.1) it is fairly easy to derive the formulation of a 3D traveltime operator for a monotonous curve at the receiver-side in the hyperbolic expansion.

$$\begin{aligned} T(G',S') = T_{\mathrm{CR}} \quad &- \quad \frac{\Delta g\,(\cos\beta_G \cos\alpha_G + \cos\theta_G \sin\beta_G \sin\alpha_G)}{v_G} \\ &+ \quad \frac{(\Delta x_S \cos\theta_S + \Delta y_S \sin\theta_S)\sin\beta_S}{v_S} + \frac{1}{2}\left(\mathtt{C}_G + \frac{1}{v_G}\mathtt{D}_G\right)\Delta g^2 \\ &+ \quad \frac{1}{2}\left(\mathtt{C}_S^2\,\mathsf{M}_{11}^{(y)}(S,G) - 2\,\mathtt{C}_S\mathtt{D}_S\,\mathsf{M}_{12}^{(y)}(S,G) + \mathtt{D}_S^2\,\mathsf{M}_{22}^{(y)}(S,G)\right) \\ &+ \quad \left(\mathtt{C}_S(\mathtt{E}_G\,\mathsf{Q}_{2_{11}}^{-1} + \mathtt{F}_G\,\mathsf{Q}_{2_{12}}^{-1}) - \mathtt{D}_S(\mathtt{E}_G\,\mathsf{Q}_{2_{21}}^{-1} + \mathtt{F}_G\,\mathsf{Q}_{2_{22}}^{-1})\right)\Delta g\,, \end{aligned} \tag{3.2}$$

using the substitutes

$$\begin{aligned} \mathtt{C}_G &= \mathtt{E}_G^2\,\mathsf{M}_{11}^{(y)}(G,S) - 2\,\mathtt{E}_G\mathtt{F}_G\,\mathsf{M}_{12}^{(y)}(G,S) + \mathtt{F}_G^2\,\mathsf{M}_{22}^{(y)}(G,S)\,, \\ \mathtt{D}_G &= (\mathtt{H}_G\cos\gamma_G - \mathtt{J}_G\sin\gamma_G)\,K_\gamma + (\mathtt{J}_G\cos\gamma_G + \mathtt{H}_G\sin\gamma_G)\,K_\alpha\,, \\ \mathtt{E}_G &= \sin\beta_G\cos\alpha_G - \cos\theta_G\cos\beta_G\sin\alpha_G\,, \\ \mathtt{F}_G &= \sin\theta_G\sin\alpha_G\,, \\ \mathtt{C}_S &= (\Delta x_S\cos\theta_S + \Delta y_S\sin\theta_S)\cos\beta_S\,, \\ \mathtt{D}_S &= \Delta x_S\sin\theta_S - \Delta y_S\cos\theta_S\,, \\ \mathtt{H}_G &= \cos\theta_G\sin\beta_G\cos\alpha_G - \cos\beta_G\sin\alpha_G\,, \\ \mathtt{J}_G &= \sin\theta_G\sin\beta_G\,. \end{aligned} \tag{3.3}$$

The vertical displacement Δz_S has been set to zero for I assume a perfectly planar acquisition at the surface. A close inspection of above traveltime formula reveals, despite the complication induced by the parameters which characterize the borehole, that the number of stacking parameters has been reduced from fourteen to ten as it is impossible to reconstruct spatial wavefront curvatures from single-line measurements.

3.2.2 3D CO CRS operator for straight wells

For a straight vertical well which is still a commonly encountered configuration the traveltime operator simplifies considerably as the previously described transformation can be omitted leaving Δz_G as the single coordinate at the receiver-side, again setting $\Delta z_S = 0$. Now the number of

stacking parameters reduces to nine because the azimuthal angle at G cannot be detected by a set of vertically arranged receivers. The formula reads

$$\begin{aligned} T(G',S') = T_{\mathrm{CR}} \;&-\; \frac{\Delta z_G \cos\beta_G}{v_G} + \frac{(\Delta x_S \cos\theta_S + \Delta y_S \sin\theta_S)\sin\beta_S}{v_S} \\ &+\; \frac{1}{2}\sin^2\beta_G \Delta {z_G}^2 \, \mathsf{M}^{(y)}_{11}(G,S) \\ &+\; \frac{1}{2}\left(\mathtt{C}_S^2 \mathsf{M}^{(y)}_{11}(S,G) - 2\,\mathtt{C}_S \mathtt{D}_S \mathsf{M}^{(y)}_{12}(S,G) + \mathtt{D}_S^2 \mathsf{M}^{(y)}_{22}(S,G)\right) \\ &+\; \sin\beta_G \Delta z_G \, \mathtt{C}_S \, \mathsf{Q}^{-1}_{2_{11}} - \sin\beta_G \Delta z_G \, \mathtt{D}_S \, \mathsf{Q}^{-1}_{2_{21}}, \end{aligned} \tag{3.4}$$

using the substitutes

$$\begin{aligned} \mathtt{C}_S &= (\Delta x_S \cos\theta_S + \Delta y_S \sin\theta_S)\cos\beta_S, \\ \mathtt{D}_S &= \Delta x_S \sin\theta_S - \Delta y_S \cos\theta_S. \end{aligned} \tag{3.5}$$

3.2.3 2D CO CRS operator for arbitrary geometries

For an arbitrary measurement configuration assuming planar wave propagation the traveltime operator simplifies even more with the number of CRS attributes reducing to five. The search-strategy for the best-fitting CRS operator which is discussed in the following section are based on its expansion to the hyperbolic form:

$$\begin{aligned} T^2(G',S') \;=\; &\left(T_{\mathrm{CR}} + \frac{\Delta x_G \sin\beta_G}{v_G} - \frac{\Delta z_G \cos\beta_G}{v_G} + \frac{\Delta x_S \sin\beta_S}{v_S} - \frac{\Delta z_S \cos\beta_S}{v_S}\right)^2 \\ &+ T_{\mathrm{CR}}\,\mathtt{C}_G^2 \mathsf{M}^{(y)}_{11}(G,S) + T_{\mathrm{CR}}\,\mathtt{C}_S^2 \mathsf{M}^{(y)}_{11}(S,G) + 2\,T_{\mathrm{CR}}\,\mathtt{C}_G\,\mathtt{C}_S\,\mathsf{Q}^{-1}_{2_{11}}. \end{aligned} \tag{3.6}$$

For the sake of clarity, again, two substitutes have been applied which read

$$\mathtt{C}_G = \Delta x_G \cos\beta_G + \Delta z_G \sin\beta_G, \quad \text{and} \quad \mathtt{C}_S = \Delta x_S \cos\beta_S + \Delta z_S \sin\beta_S. \tag{3.7}$$

The two components of the respective paraxial slowness vector at the receiver side are formulated as the first spatial derivatives of the parabolic expansion of traveltime equation (3.6) yielding

$$\begin{aligned} p_{x_G} &= \frac{\sin\beta_G}{v_G} + \cos\beta_G \left(\mathtt{C}_G \mathsf{M}^{(y)}_{11}(G,S) + \mathtt{C}_S \mathsf{Q}^{-1}_{2_{11}}\right), \\ p_{z_G} &= -\frac{\cos\beta_G}{v_G} + \sin\beta_G \left(\mathtt{C}_G \mathsf{M}^{(y)}_{11}(G,S) + \mathtt{C}_S \mathsf{Q}^{-1}_{2_{11}}\right). \end{aligned} \tag{3.8}$$

using the same substitutes (3.7) as above.

I relate the paraxial slowness vector to the paraxial emergence angle by using the trigonometric relation

$$\tan\beta_P(\Delta x_S, \Delta z_S, \Delta x_G, \Delta z_G) = \frac{p_{x_G}}{p_{z_G}}\,. \tag{3.9}$$

To achieve a similar result, earlier publications reverted to the assumption of a locally circular emerging wavefront being tied to the the central ray (modification were applied to the method by Boelsen (2005) based on Höcht et al. (1999)). From there an extrapolation in direction of the paraxial vicinity was made by a strictly geometric treatment. The drawback of this method was the lack of flexibility with respect to the coordinates and the introduction of numerical singularities which had to be handled individually.
For the treatment suggested by me the singularities are restricted to either of the slowness components vanishing which results in well-defined paraxial emergence angles. Another benefit of this approach is the generality of the formulation including a whole CRS supergather into the scope of consideration if it is desired. For the following I neglected the additional terms involving $\mathsf{Q}_{2_{11}}^{-1}$ so that all paraxial angles of single common shot gathers are extrapolated. One has to keep in mind that as long as v_G is selected without relating it accurately to the depth domain there will be no reliable estimation of the orientation of the wavefield. A coherence analysis performed in the time domain without considering this fact still yields optimum stacking parameters but there will be no real applicability beyond that.

Figure 3.2.3 illustrates the involved variables and parameters employed in equation (3.6). The coefficients $\mathsf{M}_{11}^{(y)}(G,S)$, $\mathsf{M}_{11}^{(y)}(S,G)$, and $\mathsf{Q}_{2_{11}}^{-1}$ have been omitted for the sake of clarity but can be thought-of as the accounting factors for the deformation of the central ray's *ray tube*.

3.3 Performing coherence analysis in the data-domain

If I begin by neglecting the multicomponent approach I am left with an optimization problem of simultaneously determining five stacking parameters in order to provide expression (3.6) with the necessary terms for a proper moveout correction. The means by which the stacking parameters are checked for their quality is a *coherence analysis* performed on the seismic data in the time domain being found in the vicinity of the central ray defined as a CRS supergather. Such a supergather, or aperture if the terminology from geometrical optics is used, is composed of several neighboring shot as well as receiver points around S and G. Its size has to be chosen large enough to guarantee stable stacking parameters but also small enough to be able to still observe the local deformations of the traveltime field. As a commonly chosen criteria for data-driven approaches—the *semblance coefficient*—is used in my implementation being firstly introduced by Taner and Koehler (1969). Physically this quantity is defined to be the normalized ratio of

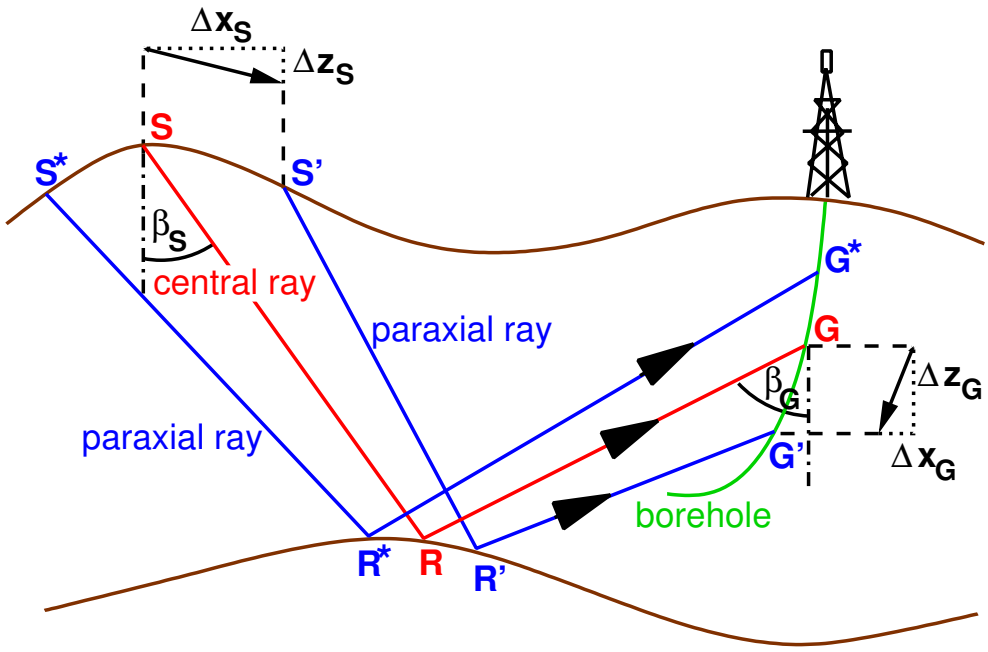

Figure 3.3: *Sketch of a offset VSP geometry in 2D. Top-surface topography and a deviated well are prominent features which, surprisingly, do not increase the number of stacking parameters.*

output to input energy. In mathematical terms S_C, the semblance coefficient, is defined as

$$S_C(\mathsf{f},\beta_G,\beta_S,\ldots) = \frac{\sum_{j=k(i)-W/2}^{k(i)+W/2}\left(\sum_{i=1}^{M}\mathsf{f}_{i,j(i)}\right)^2}{M\sum_{j=k(i)-W/2}^{k(i)+W/2}\sum_{i=1}^{M}\mathsf{f}_{i,j(i)}^2}. \tag{3.10}$$

Here, M is the number of traces inside of the aperture and $k(i)$ denotes the time sample of the discrete CRS traveltime for a particular trace i. The index j represents the sample position within a temporal band of width $W+1$ centered about the CRS traveltime surface. The amplitudes derived from time-series stored in matrix f are computed by means of either a linear or a "sinc" interpolation between the amplitude values associated with the two time samples next to $j(i)$. Please do not confuse the function parameters of $k(i)$ and $j(i)$ with a summation index. The range of possible semblance values varies between 0 and 1 where a higher number indicates a higher content of coherent signal.

For an extended approach of performing a coherence analysis on multicomponent data I suggest to combine two individual semblance analyses into one and to attach additional weighting coefficients. In the case of non-rotated two-component data H, V assuming 2D wave propagation a

possible formulation can be stated as

$$
\begin{aligned}
S_C^{\mathrm{R}}\left(\mathrm{f}^{\mathrm{H}},\mathrm{f}^{\mathrm{V}}\right) &= \sin(\beta_G^{\mathrm{P}})\, S_C(\mathrm{f}^{\mathrm{H}},\beta_G^{\mathrm{P}},\ldots) + \cos(\beta_G^{\mathrm{P}})\, S_C(\mathrm{f}^{\mathrm{V}},\beta_G^{\mathrm{P}},\ldots)\,, \\
S_C^{\mathrm{T}}\left(\mathrm{f}^{\mathrm{H}},\mathrm{f}^{\mathrm{V}}\right) &= \cos(\beta_G^{\mathrm{S}})\, S_C(\mathrm{f}^{\mathrm{H}},\beta_G^{\mathrm{S}},\ldots) + \sin(\beta_G^{\mathrm{S}})\, S_C(\mathrm{f}^{\mathrm{V}},\beta_G^{\mathrm{S}},\ldots)\,,
\end{aligned}
\tag{3.11}
$$

for radially-oriented particle motion and transversely-oriented motion, respectively. Again, I have to point out that emergence angles β_G^{P} and β_G^{S} are the result of a calibration using realistic velocities for P- and S-waves. Altogether, my idea of coupling has not been tested by any means so I cannot comment on possible disadvantages until an investigation has been carried out. I expect this method to improve the identification of shallow or strongly dipping reflection events over a solitary analysis of either component.

The drawback of any imaging method based on coherence analysis is that it expects the shape of a source wavelet to remain identical under varying angles of reflection. In other words the method performs on *isophase lines* for the whole traveltime surface. For very oblique angles of incidence the influence of an unavoidable phase shift will impact on the quality of the estimated stacking parameters. For the common offset CRS method this issue has always to be kept in mind.

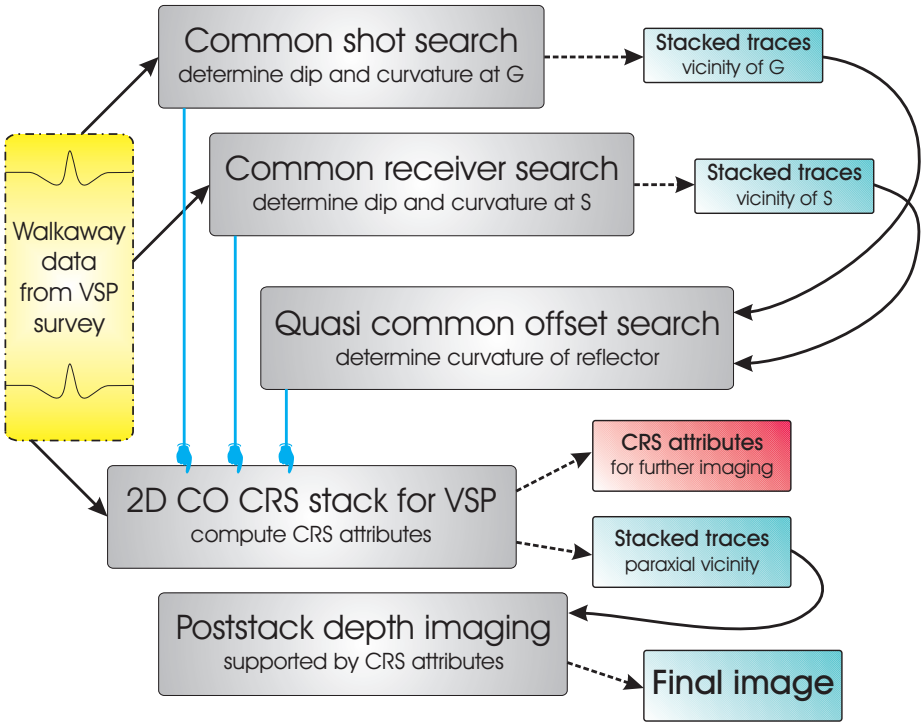

Figure 3.4: *Search strategy for either imaging qCO and qCMP configurations as resulting traces.*

3.4 Poststack imaging using the CO CRS stack

In his master's thesis Boelsen (2005) suggested a simultaneous coupling of wavefield decomposition and coherence analysis with the aim to support the stable determination of the CRS stacking parameters. His work was based on investigations carried out by Bergler et al. (2002a) who placed their emphasis on the processing of surface as well as ocean-bottom seismic data in the non-zero offset domain.
The results of either work were promising advances towards a new way of CRS imaging with the additional aim of wavefield decomposition in case of readily available multicomponent data. The problems which remained unresolved can be summarized as follows:

- the data examples used for verification consisted of relatively simple synthetics which upheld the CMP assumption, i.e., description via *midpoint-offset* coordinates. The earth model does not comply with this assumption when circumstances like irregular topography, complex near-surface or subsurface are present. Moreover, not all acquisition geometries provide data which can be transfered into the CMP domain, with data recorded by borehole surveys being an example.

- the wavefield decomposition of field data requires a calibration of the CRS-based stacking parameters to true near-surface velocities. The sensitivity to incorrect velocities especially for VSP data with different velocities at the various receiver levels is enormous.

- the initial design of a CRS-based search strategy with respect to the handling of multicomponent data suffered from very poor computational performance in a way that further systematic research was rendered impractical.

Therefore, my redesign aimed primarily at the compensation of the above imperfections and unclarities.

As indicated earlier, five stacking parameters have to be determined from the multi-coverage data domain. Since a simultaneous search—even with todays advances in computer power—would still be too costly, I sought for simplifications and found them in the partitioning of the task. Two pairs of the parameters are determined from differently aligned subsets of the data domain, containing the prestack data in the common shot (CS) and common receiver (CR) domain. To this point there exist clear similarities to the *common-shot point stacking* introduced by Keydar et al. (1996) while in the subsequent steps the concept has been carried to a much further extent. The fifth stacking parameter is determined from intermediate stacking results which are produced alongside of each coherence analysis of the previous two searches. This set of stacked traces follows a certain relationship of shot and receiver points to which I will refer to very generally

as *bilinear relation* as we still have not made any restrictions concerning the type of acquisition geometry.
For the sake of earlier conventions and simplicity the matrix elements from expression have been renamed in the following way:

$$K_{\mathrm{CR}} = v_S \mathsf{M}_{11}^{(y)}(S,G)\,, \quad K_{\mathrm{CS}} = v_G \mathsf{M}_{11}^{(y)}(G,S)\,, \quad Q_2^{-1} = \mathsf{Q}_{2_{11}}^{-1}\,. \tag{3.12}$$

In the first two searches for pairs of one angle $\beta_{S/G}$ and one wavefront curvature $K_{\mathrm{CR/CS}}$ the traveltime operator (3.6) is broken down according to the type of configuration which is under investigation. This is done mathematically by setting either the displacements at S or G equal to zero. For the third search the whole expression is utilized with four stacking parameters being in place already. The workflow displayed in Figure 3.3 describes the most significant steps of the whole algorithm and how they build upon each other.
Each constituent's analysis is carried out through a linearized parameter search with an initial plane wave assumption which first will yield the slowness-related terms of the traveltime operator. For this search the paraxial aperture will be reduced to roughly $3/4$—a rule of thumb not backed by physical explanation—of the originally intended value. Having an estimate of the local dip of a reflection event I can add an additional degree of freedom accounting for the local curvature of the event with the full aperture being used. Furthermore, I now can perform an iterative refinement for either one of the stacking parameters or a local optimization for two parameters simultaneously. However, prestack data of high quality is required for this method to be able to localize an optimum quintet of values from the parameter space for every time sample of the output trace. Moreover, the input data has to contain an adequate signal-to-noise ratio to provide stable stacking parameters across a whole source wavelet which becomes significant during wavefield decomposition. Fortunately, not only surface seismic data for larger offsets but also VSP data seem to meet these requirements for the cases I encountered so far.

3.4.1 Technical issues

This is a short compilation concerning the details of the implementation being chosen for Workflow 3.3. More details on these matters can be found in the manual of the respective computer code which has been developed in the course of this thesis.

- **Basic description**: The 3D ZO CRS source code developed by Alex Müller, Karlsruhe University was employed serving as an initial frame for my coding. It features pragmatic search-strategies as discussed by Bergler (2004), *simulated annealing* to speed up local optimization, and MPI-based parallelization. To even give a rough estimation for the time to process a set of VSP data is difficult. With the present computational power

(see, appendix B for some indication) the processing of *one* gather during *one* of the initial searches remained below 5 s. The time invested for stacking or actual wavefield decomposition was negligible.

- **Adjustments**: For the code to be usable with the above workflow and in a more general sense the elevation coordinates at source and receiver had to be included. The binning according to those coordinates into CS and CR gathers had also to be considered. As I solely focused on 2D acquisition of either surface seismic or walkover VSP lines a linear regression had to be included as well (see, e.g., Mann (2002) for a similar treatment).

- **Improvements**: Trace normalization based on the *analytic signal* of a time series was included and evidently improved the stability of the coherence analysis. For each shot and receiver position the near-surface velocity can be chosen individually which accounts for near-surface heterogenities as well as for the flexibility being needed in a borehole as it penetrates various layers of rock in the subsurface. The curvature searches do now iterate on a logarithmic scaling which will cover a much broader range of values with comparably fewer increments instead of a relying on a linear scale.

- **Open issues**: Apertures based on the *projected Fresnel zone* can be easily determined from the CRS stacking parameters once a preliminary search has been carried out. Stacking results will meet a prerequisite like *amplitude preserving imaging* more easily if the number of contributing traces is controlled in this way.
  If there are several maximal coherence values detected for different quintets of stacking parameters this is usually caused by intersecting reflection events. The handling of such *conflicting dip* problems will improve the image quality in regions where they occur. The subjects of adaptive apertures as well as conflicting dips were due to the limited amount of time not included in the implementation. I again refer to the publications of Mann (2002) and Bergler (2004) for possible solutions.

3.4.2 Resulting imaging space

For the case of surface seismic data the search strategy normally yields a set of CRS stacked traces for a particular common-offset bin which can be chosen arbitrarily as long as it still contained in the multicoverage data. The improvement over earlier strategies lies in the handling of topography and the flexibility in the near-surface velocity for both ends of the central rays being imaged. Another option which can be considered is the simulation of common-midpoint gathers that are missing from the input data due to irregularities in the survey design. Moreover a whole new set of stacked data can then be synthesized from the initial data with the result being

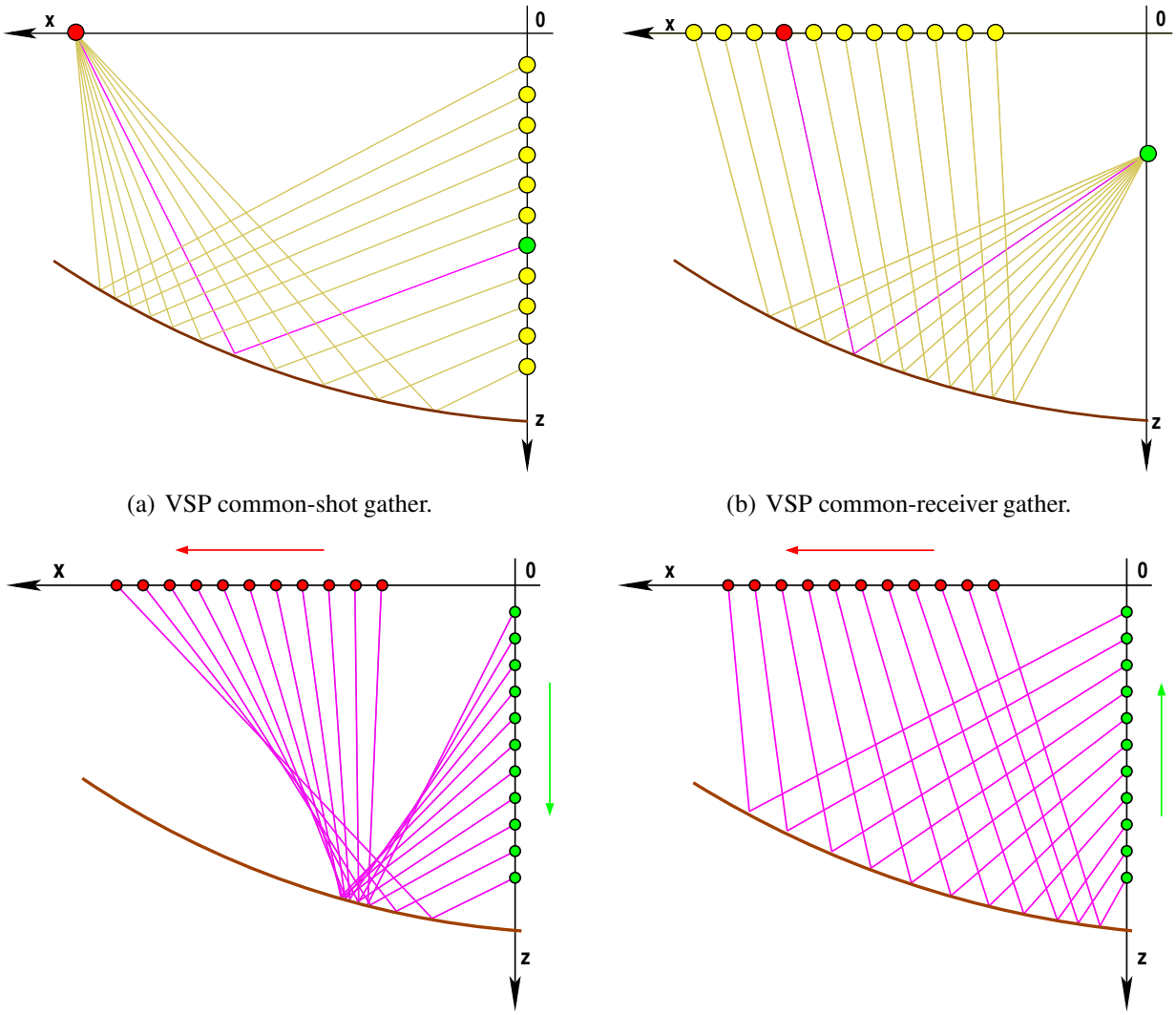

(a) VSP common-shot gather.

(b) VSP common-receiver gather.

(c) Quasi common-midpoint gather.

(d) Quasi common-offset gather.

Figure 3.5: *Schematics of different imaging spaces used in the intermediate and final steps of the CO CRS processing for VSP walkover data.*

CRS-filtered according to a general second order traveltime approximation. I will illustrate this as a promising possibility in section 5.2.

The common-shot and common-receiver domain are not symmetrical for the VSP case as one can observe for a synthetic example shown in Figure 1.5. The two sketches in the top area of Figure 3.5 describe how a central ray with respect to its paraxial rays will behave for a single reflector in depth assuming a point-source being placed at either S (see, Figure 3.5(a)) or hypothetically at G (see, Figure 3.5(a)) which would be realized in a *reverse VSP* measurement). One can already reason that these two experiments are the underlying physical interpretation for the first two search-steps of the Workflow 3.3.
An even greater difficulty lies in the lack of a distinct CMP and CO binning in the data because the shot points are moved rather horizontal while the receivers are attached to a vertical cable. This peculiarity requires the bilinear relation for the third search in the workflow to be performed in a artificially constructed configuration.

Figures 3.5(c) and 3.5(d) illustrate two different types of bilinear relation for central rays which illuminate a target reflector in opposite ways. To the first configuration I will refer to as the *quasi common-midpoint* (qCMP) geometry. If source and receiver positions both move away from the wellhead as in Figure 3.5(c) one covers a very limited lateral range because the reflection points remain close together. One also observes that the angles of incidence show a great variance. In case of an opposing movement as it is indicated by the so-called *quasi common-offset* (qCO) geometry depicted in Figure 3.5(d) the covered range extends very far away from the well and the angles of incidence remain fairly similar. A downside of this geometry is that while the resulting set of traces will provide an optimum illumination which covers an extensive part of each reflector, the area which lies close and shallow with respect to the recording array is not imaged at all. The shape of the chosen reflection interface does not change any of the above observations too significantly even if I consider it to be strongly concave or convex. For receivers which lie closely above an interface the observations will not hold anymore. Altogether, the survey design carried out *a priori* heavily impacts on the potential for a wide lateral illumination. A sufficient coverage by shot points at reasonable spacing has to be considered.

Therefore, I recommend for all investigations which aim at lateral imaging of walkaway VSP geometry the simulated central rays i to follow the relation

$$x_0 + i\,dx + z_0 + i\,dz = h_{\mathrm{VSP}} = \mathrm{const}\,, \tag{3.13}$$

with increments $dx > 0$ and $dz < 0$, position x_0 being close to the well, and position z_0 at the deepest receiver level. The quasi-offset h_{VSP} can be regarded as the classical *finite offset* of surface seismic acquisition in case the borehole axis was rotated by 90 degrees to the opposite side of the sources. Ideally, the target of a seismic survey, e.g., a reservoir for hydrocarbons, should lie some distance beneath the recording array. As an alternative to this requirement it is

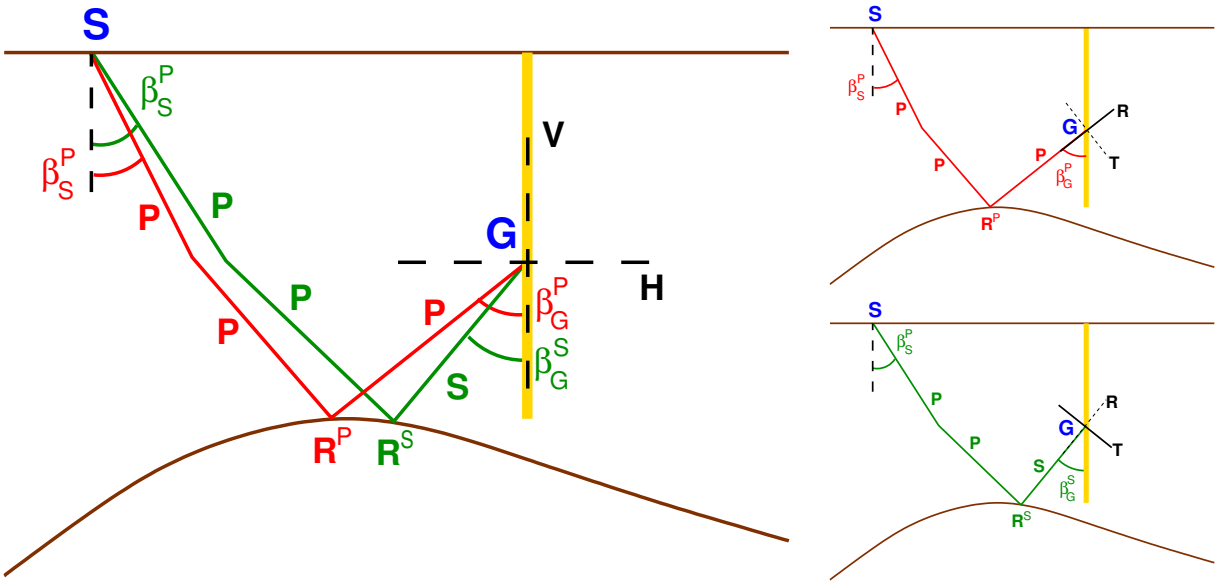

(a) Prior to rotation reflection events are recorded superpositioned.

(b) Applied separation.

Figure 3.6: *Schematic of wavefield separation based on emergence angles estimated at G.*

necessary to provide a sufficient number of geophones above the target in order to guarantee a stable coherence analysis in selected subsets of the full array.

Returning to Workflow 3.3 I want to point out that the positions of analyzed CS and CR gathers in the recorded data and the associated shot and receiver expansion points related to simulated rays have to be in accordance with relation (3.13). In this way the intermediate stacking results for CS- and CR-searches will be kinematically equivalent so that both sets of traces can enter into the third parameter search simultaneously. This requirement has been indicated by the red and green dots for the various measurement configurations of Figure 3.5 and is also valid for a third search in actual CO geometries from, e.g., surface seismic data. Concluding, since the CRS-stacked VSP time and attribute sections are obtained in either a quasi-common-offset or conventional CO domain, it will be difficult characterizing the subsurface at this stage. A standard depth migration has always to be performed right after the application of the CRS stack which will move the reflection events to their true location so that a geological interpretation will become feasible.

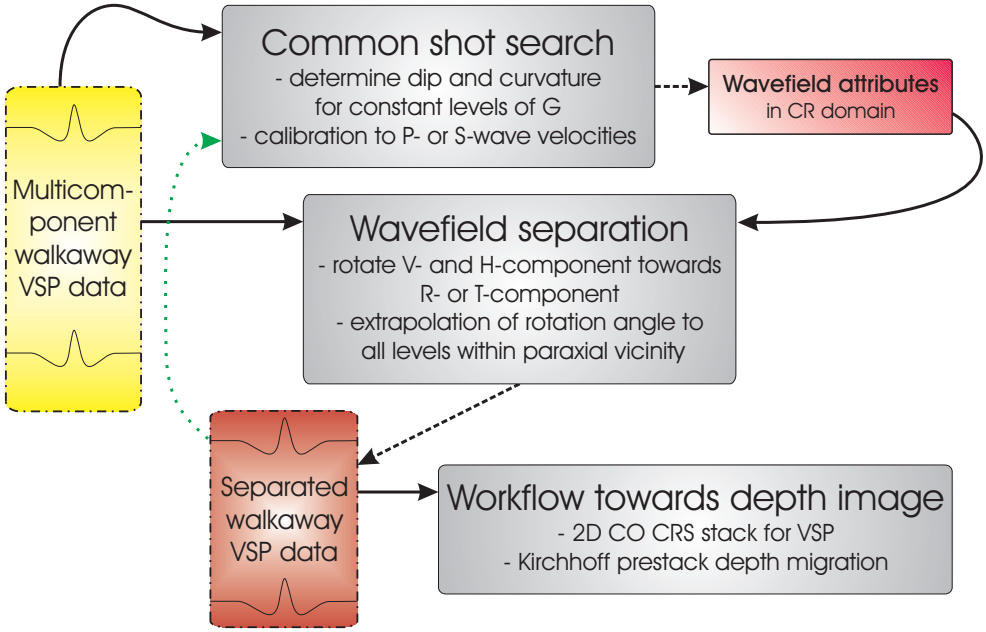

Figure 3.7: *Wavefield separation based on CRS attributes—processing workflow.*

3.5 Wavefield separation using CRS attributes

The idea behind the wavefield decomposition based on the CO CRS approach is realizable with little effort. For the chosen explanation I restricted myself to sources which emit mainly compressional wave energy, e.g., explosive charges, but analog considerations also apply for shear wave-emitting sources. As depicted in Figure 3.6(a) one observes P-waves being created at point S which propagate through the subsurface and eventually will reach an impedance contrast in form of a reflection interface to produce a seismic reflection. The reflection event mainly consists of P-wave energy but some energy will also be converted into S-waves according to Zoeppritz' equations. Reflection point R^{P} and conversion point R^{S} generally do not coincide.

Therefore, a two-component geophone placed at point G will not only record PP- and PS-events originating from different directions related to the emergence angles β_G^{P} and β_G^{S}. Additionally, any observed event will be distributed on the vertical (mainly P-waves) and horizontal (usually S-waves) component of the geophone in a superpositioned sense.

The proposed processing scheme includes the individual determination of the emergence angles β_G^{P} and β_G^{S} for a virtual geophone placed on the receiver side of a central ray. A calibration to either P- or S-wave velocity-depth functions has to be performed prior to each of these analyses which will assign a true, physical meaning to the stacking parameters. The calibration is the

most crucial step of the whole procedure an can be achieved by different means, being explained here with respect to VSP-related geometries:

- reverting to existing depth-velocity models from the surveyed area. In case of synthetic data the initial model for the generation of the seismograms can be used (as shown by Boelsen and Mann, 2005).
- inverting the first-break information from checkshot data. This method was exercised for example **B**.
- performing a CO CRS stack for *all* source-receiver pairs of the first-break, i.e., the downgoing waves, calibrated to underestimated velocities. Its results, once corrected in a certain way, can also serve as very good estimates for the velocity-curves of upgoing waves if anisotropy is negligible. I will provide further details on this newly introduced method in example **A**.

Either of the first two methods highly depends on a reasonable choice of smoothing windows and weights. This is due to investigations which have shown that the numerical range of the stacking parameters can fluctuate severely, yielding a poor wavefield decomposition, while the coherence analysis still performed stable. In this way, a correlation with hodogram data obtained for a prominent horizon is desirable, being an issue for future research.

The wavefield decomposition of the horizontal and vertical components of prestack data aims at a reliable discrimination of individual sets of data showing either increased P- or S-wave energy. Two ways exist to achieve this aim where the first relies on performing two coherence analyses for *all* source-receiver pairs, considered impractical from a computational point of view—yet feasible with today's computer power for the 2D case. The second option makes use of the paraxial slowness vector which was introduced in section 3.2.3. This implies that the CO CRS analyses are performed on a particular selection of source-receiver pairs, assuming them to be linked to a range of *paraxial geophones*. The apertures which were chosen during the individual search steps will have a direct impact on the quality of paraxial emergence angles estimated through relation (3.9).

Once the emergence angles for the whole set of prestack data have been determined either through computation or extrapolation the subsequent wavefield decomposition can be performed. For each sample of the time series a rotation matrix with the local angle at G as an argument is multiplied with the vector of initial horizontal and vertical amplitudes. The result will be a vector with *transversal* (T) and *radial* (R) components. Depending on the angle being considered, amplification will either be dealt to compressional waves for the R-component or to shear waves for the T-component. Both possibilities are depicted in Figure 3.6(b). At this stage a wavefield

decomposition with respect to the source-side of the central rays can be an optional step and depends heavily on the signature of the device which generates the seismic energy.

There are two difficulties which will require special attention in case of the investigation of this method being carried to a higher level. One problem is the sensitivity of an extrapolated emergence angle to variations in the velocity field for the receiver array being centered around an expansion point G. Especially in case of VSP data where velocity contrasts are directly intersected or a strongly heterogeneous weathering layer is encountered in some surface seismic data, the accuracy of the extrapolation will decline rapidly with increasing displacement. A possible solution towards a correction term lies in the consideration of the linear velocity gradient as introduced in appendix A.2.
Another even more problematic point is the alteration of the shape of a seismic wavelet once all of its constituent time samples have passed the rotation by associated angles which have been determined more or less individually. I suggest a coupling of the resulting volume of emergence angles—being smoothed with the length of the wavelet in mind—with the traditional polarization-orientation analysis, i.e., employing hodograms.

In case of a multicomponent approach I formerly used to couple the CO CRS wavefield decomposition with the initial search-step in the CS domain. The focus was placed on a decomposition for all traces which were located inside the search apertures as demanded by the bilinear configuration of sources and receivers. This implies that the traces lying outside of the apertures were not considered for extrapolating a paraxial angle as the result would have been highly inaccurate anyway.

With an additional usefulness of decomposed data for conventional imaging algorithms, e.g., prestack depth migration, in mind I decided to establish the method as an independent and external processing step. By this means the CO CRS imaging workflow has become a more general process working on single-component traces, only. The decomposition workflow as shown in Figure 3.5 now receives two-component traces and will provide single-component traces with the desired wavemode being enhanced. The initial search-step for a local dip and curvature in common-shot gathers is still its main component. The difference to the earlier implementation is that the resulting configuration of stacked traces resembles a common-receiver gather. In this way a more regular output can be generated and aperture ranges can be specified more dynamically.

A technical issue which had to be overcome for VSP walkaway data obtained from vertical wells is the insensitivity of the angular stacking parameter to a particular direction. The proper sign is found through a rotation of the respective time samples by $\pm\beta_G$ and a subsequent stacking of the amplified constituents. The higher stacking value selects the appropriate sign for that sample.

Chapter 4

Three VSP data examples

All three examples I am going to present are based on seismic data as it is regularly measured in the vertical seismic profiling acquisition geometry. From a research point of view each one of them has peculiar features which justify it to be shown here. To simplify the reference to the individual examples I will call them from now on data sets **A**, **B**, and **C**. The ascending order of placement in this chapter reflects the amount of invested efforts in order to carry out the processing and can be regarded as a measure of the challenges involved.
I will address the individual distinctive features in the introduction of each example's discussion with respect to the other two. The chronological order by which the examples were compiled is the following: **A** for the acoustic case, **B**, **A** for the elastic case, and **C**. Personally, I consider example **C** to be the most challenging not only from the technical, or better, implementation side, but also from a modeling viewpoint with respect to illumination. The lack of an appropriate tool for the preconditioning of the data—our license of PROMAX expired—towards the end of my studies restricted the amount of qualified results being produced. Yet, I am confident that these preliminary results will still prove my point.

4.1 A: Synthetic seismic data—straight vertical well

I will begin this chapter by introducing synthetic data example **A** which was kindly provided by **Paulsson Geophysical Services, Inc.** and served as the central data to experiment with. Obviously, a synthetic model has the advantage that one does not have to deal with irregularities of field data related to their recording. Yet the problem definition while remaining strictly controlable can be shaped towards a very realistic level of complexity.

4.1.1 Data description

Figure 4.1 shows a 3D plot of the two walkover lines crossing a vertical borehole (depth up to ≈ 0.8 km) almost straight in north-south and east-west direction. Both lines have approximate lengths of 2.0 km. There are several gaps in the shot-spacing indicating the close relationship to the field data set which will be investigated as example **B**. The acquisition surface can be described as almost planar with a slight dip towards the west. The two reflectors in depths of approximately 0.5 km and 1.0 km are both strongly dipping and the second reflector has a very irregular shape.

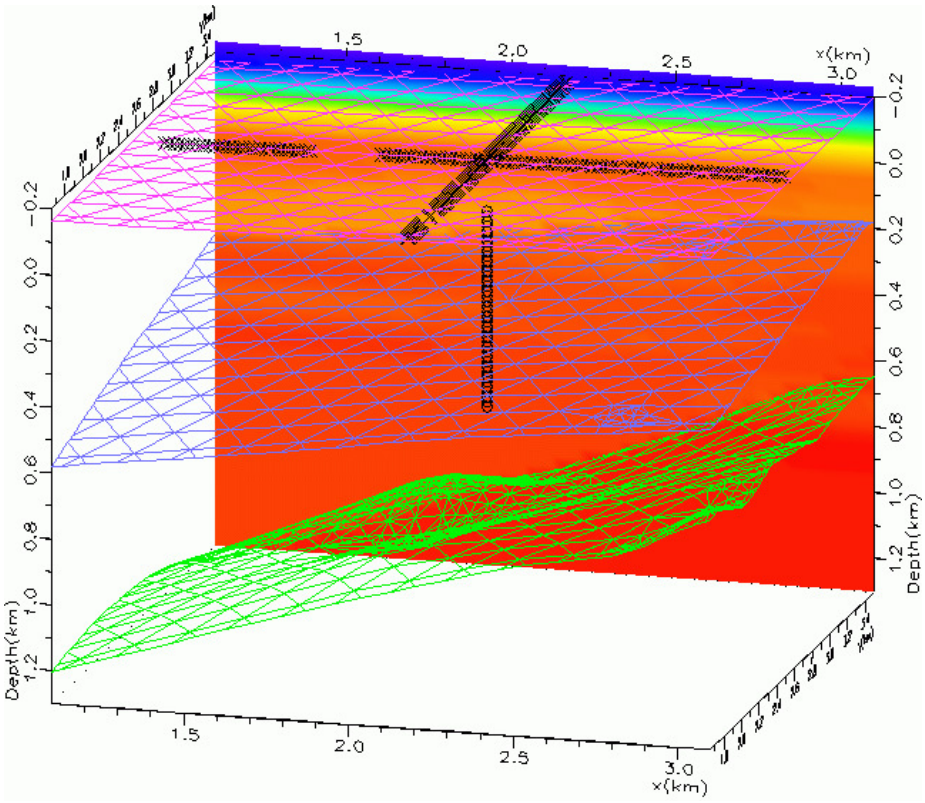

Figure 4.1: *Map of the two walkover lines being processed. The two reflectors in depth show significant dip and structure.*

Slices through the underlying heterogeneous 3D velocity model for primary waves taken right through the two walkover lines are depicted in Figure 4.2. The whole model contains a steep velocity gradient for the first 300 m, which cannot be observed in the figures because it is clipped out of the displayed range. This gradient will be responsible for the observation of turning waves on the upper levels of the geophone chain as a result of the raytracing. The corresponding

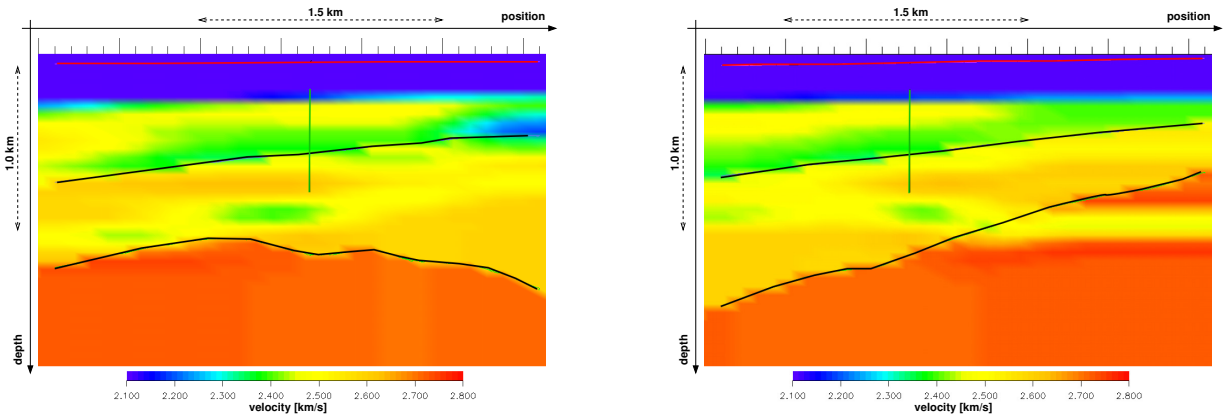

(a) Velocity model in north-south direction.

(b) Velocity model in east-west direction.

Figure 4.2: *Velocity models sliced along the two survey directions.*

shearwave velocities were derived by applying a constant v_P/v_S-ratio of $\sqrt{3}$ as being a commonly used value.

The elastic raytracing and the subsequent generation of synthetic seismograms both were carried out with the help of the modeling tool NORSAR. The raycodes which were synthesized are the following: the downgoing P wave, the reflected PP and SS waves, but also the converted PS waves for both reflectors. Emphasis during the processing phase was put on all the events related to a compressional source. The shearwave sources were polarized in direction of the walkover line and their sole purpose was to have an indicator of expectation for their time of arrival with respect to all the other arrivals.

The description of the prestack data concerning the geometry of the virtual survey is compiled in Table 4.1. In order for this type of coherence-based analyses to be working on reflected or converted energy contained in VSP-recorded data, it has to be preconditioned in the following manner. Downgoing energy has to be focused on the first arrivals of the P-wave either by using deconvolution operators or surgical f-k-filtering. In a similar way, the downgoing S-waves should be eliminated. Such a condition for the data can be easily composed by using synthetic seismograms obtained from ray methods.

4.1.2 Velocity calibration and wavefield decomposition

My primary objective during the CO CRS-based wavefield decomposition is the relation of determined stacking parameters for each central ray to the true polarization direction of an incoming wavefront. Great care must be taken for the estimation of the calibration velocities v_P and v_S at

Context	Parameter	Value
Modeling parameters	Used method	Isotropic Raytracing for (V, H_1, H_2) components
	Depth model	3D, heterogenous
	Ray codes	P, PP, PS, SS
	v_P/v_S ratio	$\sqrt{3}$
	Signal-to-noise ratio	7
Shot and receiver geometry	Number of shots	2×108
	Shot interval	≈ 16.8 m
	Surface topography	± 15.0 m
	Number of receiver levels	40
	First receiver in depth	153.5 m
	Receiver interval	15.24 m
	Number of 3C traces	2×4320
Recording parameters	Recording time	0.0...2.0 s
	Sampling interval	2.0 ms
	Frequency range	20-160 Hz
	Mean frequency	60 Hz

Table 4.1: *Information on the prestack data, obtained from the trace-headers prior to processing.*

the receiver side. As I will show here, even a apparently accurate depth-velocity relationship can still be way too over- or underestimated to serve for the secondary objective, i.e., extrapolating paraxial emergence angles.

The various depth-velocity curves for P-waves shown in Figure 4.3 were not directly derived from the velocity model as I generally do not know the depth model for an area under investigation. For the solid red line in Figure 4.3 I therefore used a synthetic *checkshot* close to the wellhead and picked the first arrivals of the downgoing primary to serve as input to a 1D inversion algorithm and smoothed the resulting curve. This method of calibration turned out to be difficult to control via the width of the smoothing window and very sensitive to the choice of the initial velocity and thickness of the weathering layer during inversion.

A test of the reliability of this calibration was carried out by studying the emergence angles for the downgoing waves generated at all shotpoints and reaching every receiver. The ideal angles were forward-computed through the raytracing routines provided by NORSAR (see, Figure 4.4(a)) and compared to values obtained by the CS-search of the CO CRS strategy. For the data-driven analysis of downgoing events one simply has to limit the processing range to the vicinity of the

first-break picks in the data and introduce an additional quadrant for the range of β_G.

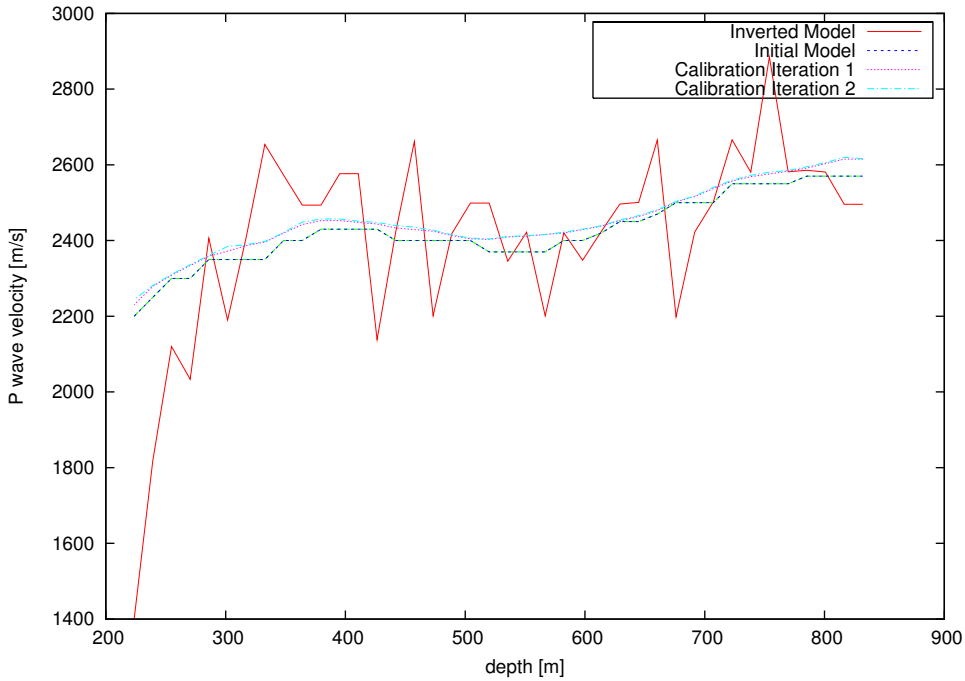

Figure 4.3: *Depth-velocity curves used for calibration. The solid curve (red) was obtained by checkshot inversion. The three remaining curves illustrate the process of finding a suitable calibration velocity in a data-driven way. See text for details.*

The remaining contour plots in Figure 4.4 show three sets of angles found by these means—for the sake of clarity, the angles are plotted as being measured with respect to an x_3-axis pointing upwards and without a sign. The main observation in Figure 4.4(b) is that the calibration to an inverted depth-velocity curve leads to significantly incorrect estimations for β_G for most receiver levels. An overestimation of the velocity leads to an over-compensation through the choice a minimal emergence angle, yielding a maximum moveout for many shots in the central area. On the other hand an underestimation will impact in excessively high angles where values close to vertical incidence would be expected.

In the underestimation (see, Figure 4.4(c)) lies the solution for finding proper velocities as I can utilize Snell's law to convert the slowness vector for the absolute minimum angle on each receiver level to its proper value. The three corresponding depth-velocity curves shown in Figure 4.3 illustrate the process. I begin the data-driven strategy with a rough estimate of a general underestimated depth-velocity trend v_{in} (blue dashed line) for all receiver levels. The CO CRS search returns a minimal emergence angle β_{in} at some point S which generally can be different

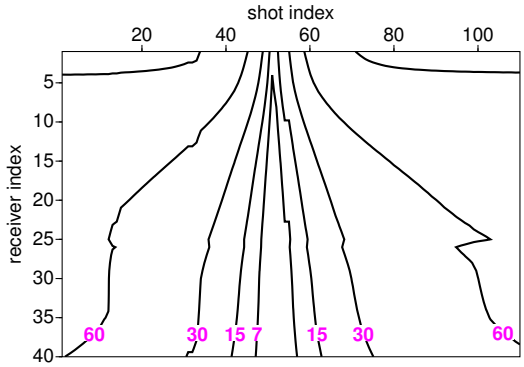

(a) Raytracing in original model.

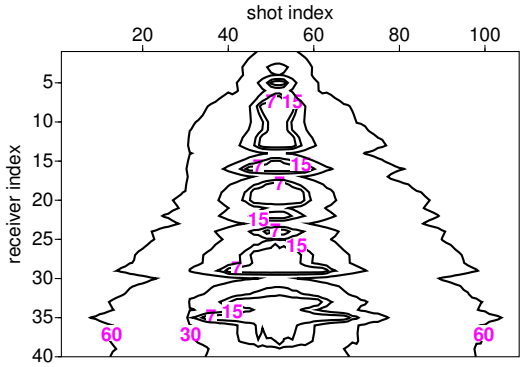

(b) Velocities from checkshot inversion.

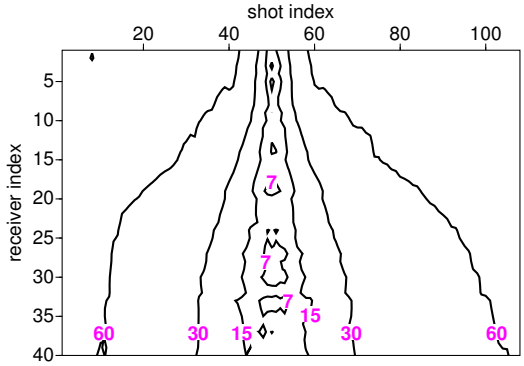

(c) Underestimated velocities.

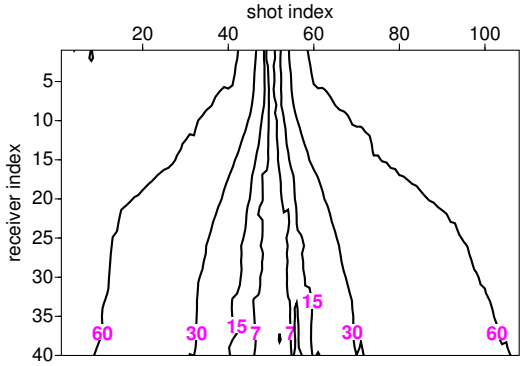

(d) Calibrated velocities.

Figure 4.4: *Contour plots of emergence angles obtained for downgoing waves. Incorrect velocities yield either over- or underestimated emergence angles.*

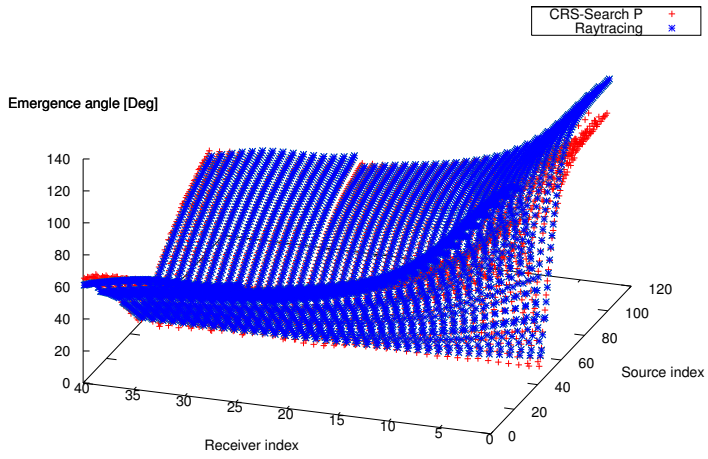

Figure 4.5: *Application of the velocity calibration using downgoing waves and comparison to raytracing in the original model. See text for details.*

for each depth level. Under the assumption that β_{in} is a *critical angle* of an internal reflection and $\beta_{\text{corr}} = 90^\circ$ the conversion is achieved using

$$v_{\text{corr}} = \frac{v_{\text{in}}}{\sin \beta_{\text{in}}} - \Delta v_{\text{off}}\,, \tag{4.1}$$

where Δv_{off} indicates an adjustment towards another deliberately underestimated velocity curve as it cannot be expected that β_{in} was a fully reliable value.

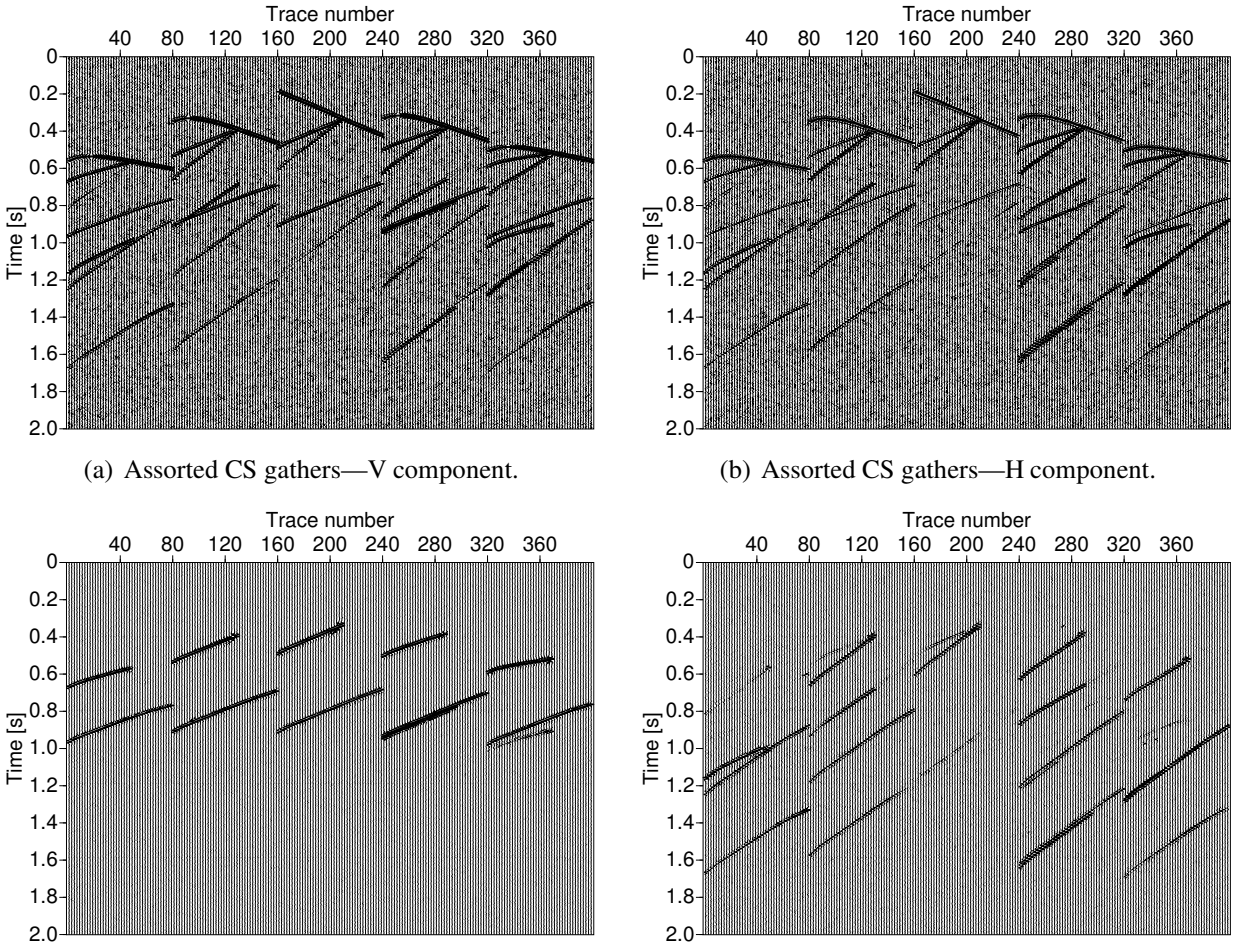

(a) Assorted CS gathers—V component.

(b) Assorted CS gathers—H component.

(c) Assorted CS gathers—R orientation.

(d) Assorted CS gathers—T orientation.

Figure 4.6: *Result: Wavefield decomposition performed on the multicomponent prestack data of the NS line. Displayed are five shotgathers at various offsets along the walkover line. Rotation by the according polarization angle yields either an enhanced radial (using β_G^{P}) or transversal orientation (with β_G^{S}, respectively).*

The corrected but intermediate depth-velocity curve is indicated in Figure 4.3 by the magenta-

colored, dotted line. Another iteration of the CO CRS search for downgoing events will then result in new minimal angles β_{in}^{*} and improved velocities as displayed by the cyan-colored, dashed and dotted line. Overall improvements of an additional iteration are small, yet, they are noticeable.

A comparison of the ideal raytracing result and the data-driven method calibrated to the latter velocity curve (see, Figure 4.4(d)) shows a close match of both methods. The discrepancies which can still be observed at the outer edges of Figure 4.4 for shallow receiver levels are most likely caused by an inappropriate size of the aperture during the search.

Corresponding S-wave velocities were found by reapplying a constant $v_{\text{P}}/v_{\text{S}}$-ratio of $\sqrt{3}$. With the underlying depth-velocity model in mind I can safely deduce it in this manner. Yet, an analog treatment for the downgoing S-waves as already described for its counterpart should result in a similar velocity curve. For the case of field data, however, it will not necessarily follow the trend of the P-wave's curve.

To give an impression on the quality of the wavefield decomposition under "laboratory conditions", I present five multicomponent common shot gathers picked over the whole range of the NS-walkover line (see, Figure 4.6). The decomposition clearly distinguishes the two types of polarization and the overall amplitudes of the events are also increased. One notices that the transverse oriented data in Figure 4.6(d) still contains the events associated with the shearwave source characterized by much later arrivals and lower amplitudes. As I mentioned earlier, a velocity calibration of the shot-side of the traveltime operator achieves a further discrimination for such events.

4.1.3 CRS-processing and depth migration

After the wavefield decomposition being applied with respect to the receiver side for both the NS- and EW-walkover line, there were two subsets of data extracted from each of them. Now, the subsequent processing steps of Workflow 3.3 were exercised with a bilinear relation as depicted in Figure 4.1.3. The widest illumination being possible was achieved by connecting the forty outermost source positions on either side with all available receiver levels following the qCO configuration. This, being a downside already mentioned, introduces a mismatch for the remaining central shot points, which were connected to the deepest receiver level, resembling partially a synthetic CR gather. Note that the intermediate traces obtained for this region—with the limits of the present implementation—were not qualified for the third search-step. Therefore, the S/N-ratio of stacked traces from the central area remained comparably lower after the final step.

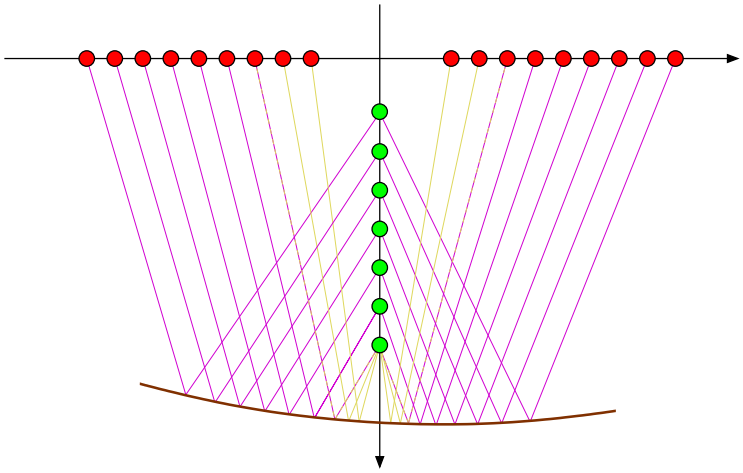

Figure 4.7: *Geometry map explaining the relation of the expansion points. The combination of source and receiver positions resembles a qCO geometry for the outer events (purple) and a CR geometry for the central events (yellow).*

Compiled in Table 4.2 is a description of the main processing parameters towards a set of CO CRS-stacked traces for PP-reflections. The parameters which lead to the underlying decomposed data are included as well. Figure 4.8 shows intermediate and final stacking results obtained for both of the walkover lines using these parameters. The searches in common-shot gathers yielding stacked traces in shown Figures 4.8(a) and 4.8(b) show a close resemblance to the search results in the common-receiver domain (see, Figures 4.8(c) and 4.8(d)). As it was mentioned already both sets of traces—mainly obeying the qCO configuration—went into the third search and the concluding CRS stack based on supergathers from prestack data was applied. As a consequence of this, the S/N ratio of Figures 4.8(e) and 4.8(f) was increased significantly.

The CO CRS stack in the current implementation—like its zero offset counterparts—provides a multitude of useful by-products and intermediate processing results. These should always be scrutinized in order to refine subsequent processing steps. An example for the high quality of the quintet of stacking parameters as they were determined for the NS-walkover line is presented in Figures 4.9(b) through 4.9(f). All angles and curvatures show a considerable wide range, however, stay mostly within the limits given in Table 4.2. The overall resolution is very high since every sample was investigated independently. The reliability of all attributes is ensured by the semblance coefficient measured with respect to the CRS supergathers shown in Figure 4.9(a). It indicates the energy-weighted fit between theoretical traveltime surface and prestack data. Consequently, unstable or unreliable areas within the output are displayed by gray color in Figure 4.9 and were masked with a coherence threshold of 0.3 as an arbitrarily chosen value.

Context	Processing parameter/step	Value
General parameters for coherence analysis	Temporal bandwidth Data preconditioning Coherence measure	30 ms Normalization Semblance
Velocity calibration	v_S^{P} v_G^{P} $v_{S,G}^{\mathrm{S}}$	$1500\,\frac{\mathrm{m}}{\mathrm{s}}$ From downgoing waves (see text) $v_{S,G}^{\mathrm{P}}/\sqrt{3}$
Wavefield decomposition	Analysis of CS gathers Calibration velocities Paraxial aperture Recombination of data	At receiver levels 10, 30 $v_G^{\mathrm{P}}, v_G^{\mathrm{S}}$ 10 levels on either side $\Rightarrow \mathsf{f}^{\mathrm{R}}(v_G^{\mathrm{P}}), \mathsf{f}^{\mathrm{T}}(v_G^{\mathrm{S}})$
Wavemodes investigated	For input f^{R} For input f^{T}	PP events PS, SS events
Search and stack related apertures	Initial searches CS search at (G) CR search at (S) qCO/qCMP search at (G,S) CRS stack at (G,S)	0.75 of full aperture 200 m 200 m 100 m, 100 m 100 m, 100 m
Search ranges and increments (from PP search)	CS search: β_G : $K_{\mathrm{CS}}\,[\frac{1}{\mathrm{m}}]$ CR search: β_S : $K_{\mathrm{CR}}\,[\frac{1}{\mathrm{m}}]$ BR search: $Q_2^{-1}\,[\frac{s}{\mathrm{m}^2}]$	0° to 70°, 70 steps -10^{-3} to $\mp 10^{-6}$ to 10^{-1}, 100 steps -35° to 35°, 70 steps -10^{-3} to $\mp 10^{-6}$ to 10^{-3}, 100 steps -10^{-6} to $\mp 10^{-10}$ to 10^{-6}, 100 steps

Table 4.2: *Example for the CRS processing parameters chosen for the imaging of the NS line. The placement in the listing reflects the chronological application of the various measures being taken.*

Alternatively to the imaging of PP-reflections I performed an analysis of shearwave-related reflections and conversions. An example of a processing with focus on the PS-converted waves is depicted in Figure 4.10. The same order for the resulting sets of stacked traces was chosen as in Figure 4.8. The intermediate stacked data after the searches in gathers of the prestack data (see, Figures 4.10(a) and 4.10(b) for CS search, Figures 4.10(c) and 4.10(d) for CR search) show a slight indication that it is possible to suppress SS-reflections. This was achieved mainly through a calibration to P-wave velocities and the choice of restricted ranges during the CR search but did not work perfectly because the chosen velocity was only a very rough estimate. Further, any suppression is conveyed to the final stacking of CRS supergathers as displayed in Figures 4.10(e) and 4.10(f). It is generally observable in these figures that events involving shearwaves are dipping much steeper and arriving much later. The associated stacking parameters show a similar good quality as the ones for PP-reflections.

All stacked data which were presented in this scope showed a gap in the shallow reflector originating from the shot-receiver combination by the qCO configuration. Naturally, as the receiver array intersects the first interface in depth only the geophones above of it can register any reflections from it. The target zone for this synthetic data should therefore be observed approximately in the depth of the second reflector. In order to give an impression of how stacked traces in the qCMP configuration will look like I also performed an analog processing flow for the NS-walkover line. A comparison between both configurations is displayed in Figure 4.11. The area which is illuminated by a qCMP gather on the one hand, as it can be seen in Figure 4.11(b), remains more in the center for the shallow reflector and extends to an unsigned offset of $\approx 600\,\mathrm{m}$. The qCO gather on the other hand illuminates the area which extends outwards from approximately these points.

Since the main output created by the CO CRS processing for VSP data is—as already mentioned—a set of stacked traces in the quasi common-offset domain unfit for interpretative visualization. Conventional imaging algorithms are required to perform this final step. For a rough assessment of the method I applied a Kirchhoff poststack depth migration to the CRS stacked traces shown in Figure 4.8(e) with the velocity model according to Figure 4.2(a). A preliminary result which still requires a considerable amount of tapering at the edges (see, Figure 4.12(a)) confirms the accuracy of the method up to the first interface. The second interface has a significantly different shape and it is migrated too shallow when being compared to the underlying model.
In order to have more hints to investigate the mismatch of the second interface I applied a Kirchhoff prestack depth migration with a migration aperture which corresponded to all the traces which had been used for the CRS stacking result. The resulting image shown as an inlay (purple box) in Figure 4.12(b) lets me draw several conclusions. The PostSDM illuminates a much larger segment of both interfaces in a constantly high resolution even if I consider the migration artifacts

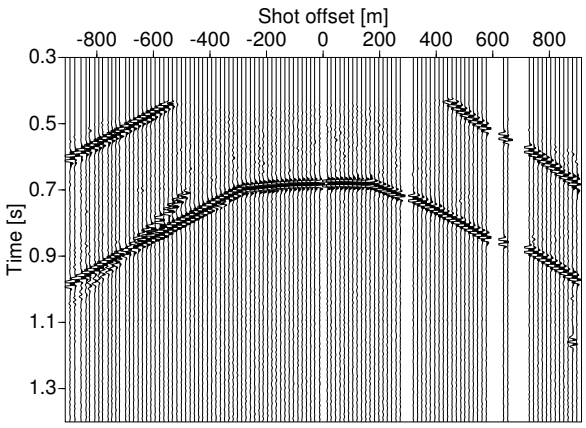

(a) Step 1: CS search for NS-line—P waves at *G*.

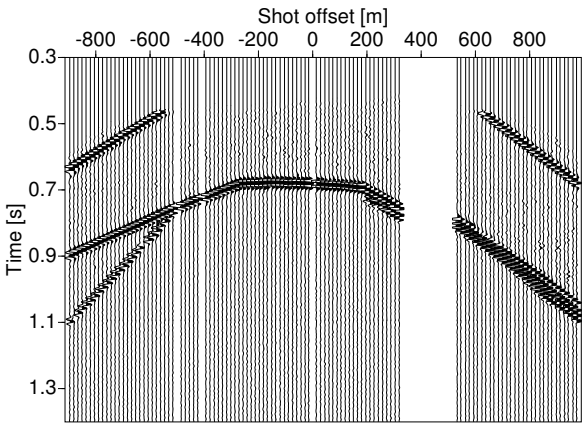

(b) Step 1: CS search for EW-line—P waves at *G*.

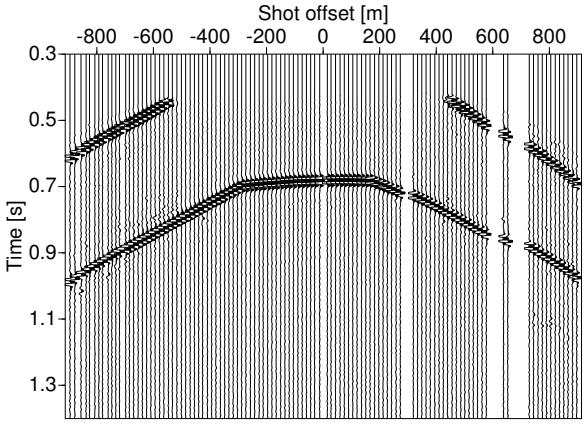

(c) Step 2: CR search for NS-line—P waves at *S*.

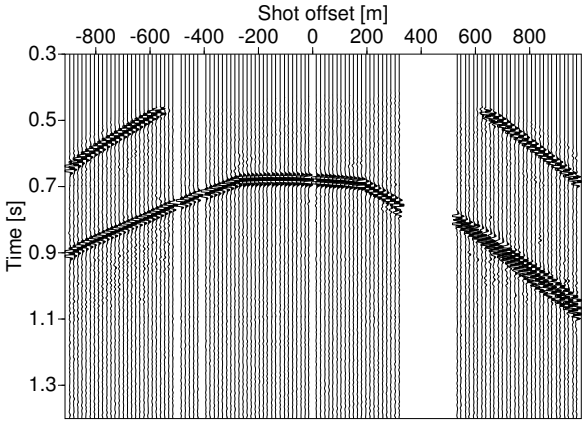

(d) Step 2: CR search for EW-line—P waves at *S*.

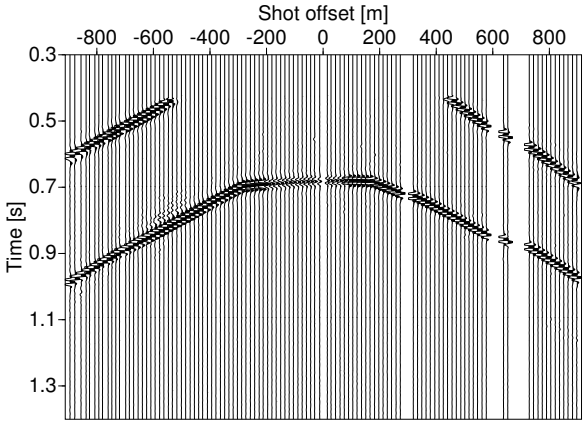

(e) Step 4: CRS stack for NS-line—PP waves.

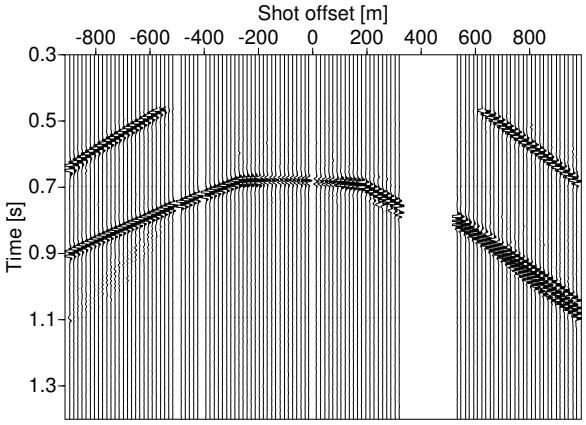

(f) Step 4: CRS stack for EW-line—PP waves.

Figure 4.8: *Result: qCO stacked traces for PP reflections. The estimation of the quintet of CRS attributes was performed on radially-oriented prestack data.*

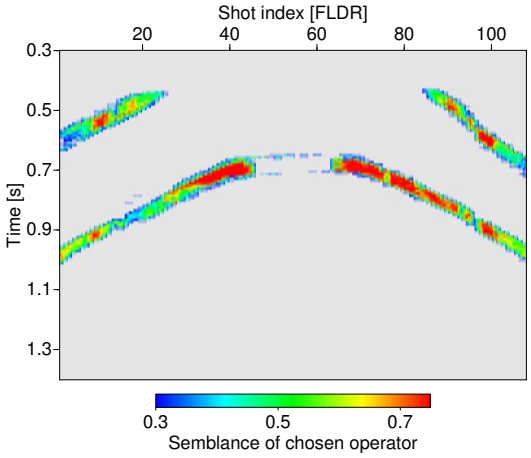

(a) Step 4: CRS stack, NS-line—semblance.

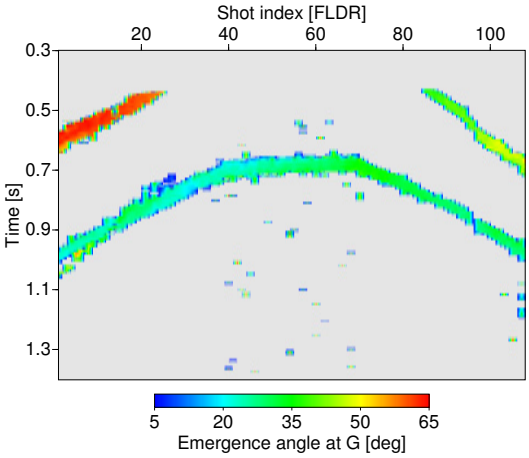

(b) Step 1: CS search, NS-line—angle β_G.

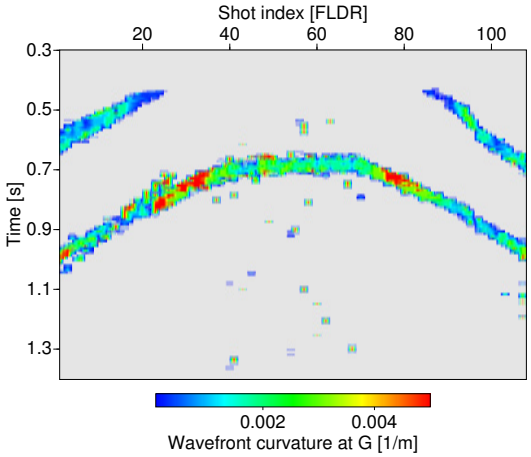

(c) Step 1: CS search, NS-line—curvature K_{CS}.

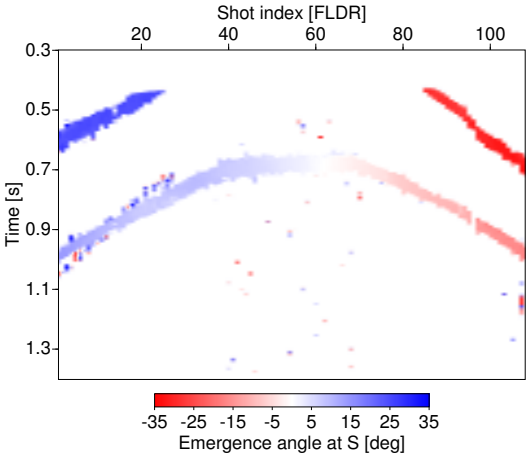

(d) Step 2: CR search, NS-line—angle β_S.

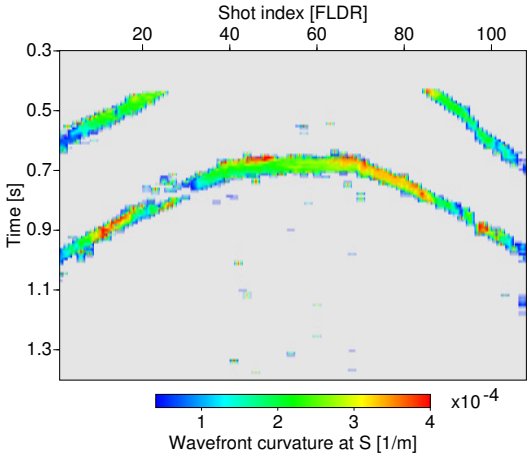

(e) Step 2: CR search, NS-line—curvature K_{CR}.

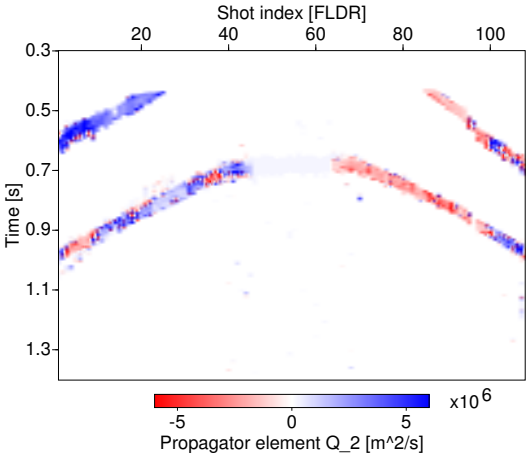

(f) Step 3: BR search, NS-line—curvature K_{BR}.

Figure 4.9: *Result: quintet of CRS attributes for PP reflections.*

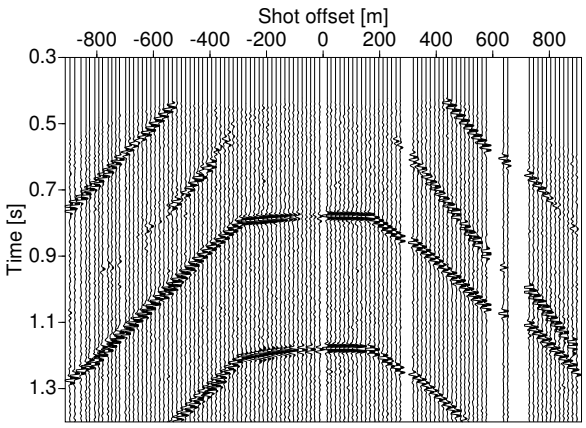

(a) Step 1: CS search for NS-line—S waves at *G*.

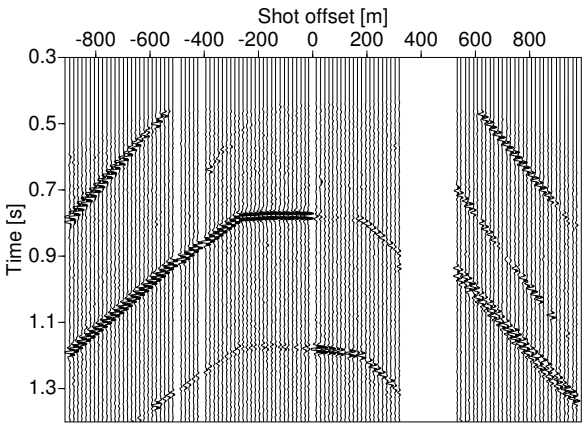

(b) Step 1: CS search for EW-line—S waves at *G*.

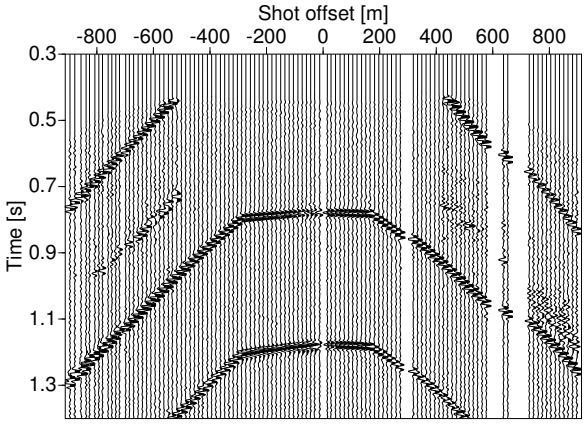

(c) Step 2: CR search for NS-line—P waves at *S*.

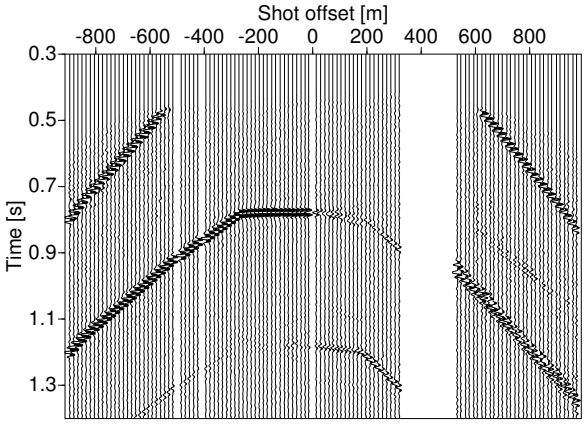

(d) Step 2: CR search for EW-line—P waves at *S*.

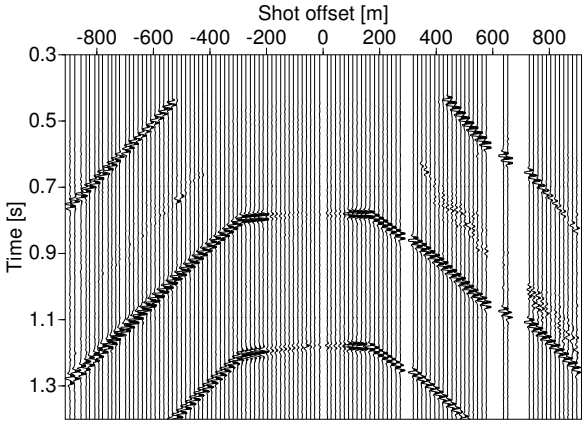

(e) Step 4: CRS stack for NS-line—PS waves.

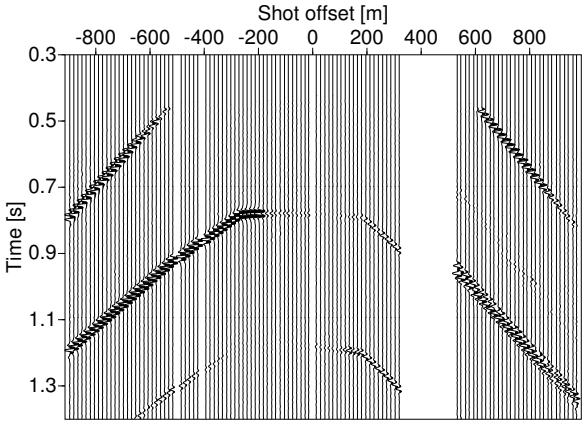

(f) Step 4: CRS stack for EW-line—PS waves.

Figure 4.10: *Result: qCO stacked traces for PS reflections. The estimation of the underlying quintet of CRS attributes was performed on transversely-oriented prestack data.*

which can be avoided easily through tapering of the edge-traces. The PreSDM has not only the same mismatch in depth and shape for the second interface but furthermore is unfocused there. The benefit of imaging a whole reflection segment instead of a single reflection point, which is the dominant feature of CRS-based methods, is very obvious for this example. The issue of mismatches in depth and shape for the area in question was finally resolved by performing several raytracing experiments in the whole 3D velocity model. In this way I was able to follow the raypaths of the modeled reflection events. As it is obvious from Figure 4.13 the assumption that all wave propagation occurs in a vertical plane does certainly not hold for this example.

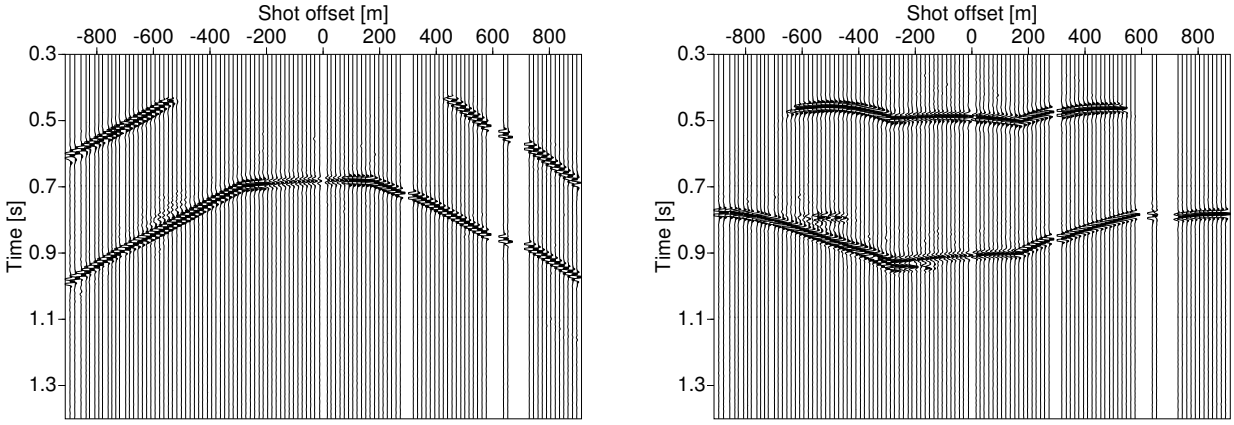

(a) Step 4: CRS stack for NS-line in qCO domain.

(b) Step 4: CRS stack for NS-line in qCMP domain.

Figure 4.11: *Result: qCO versus qCMP domain imaging for PP reflections.*

4.1.4 Summary and conclusions

The initial processing of synthetic data **A** was carried out in the very beginning of my studies and provided me with enough confidence for a more detailed investigation of the whole subject. The imaging sequence using particular bilinear relations was the result of this research. By time, a first verification of the wavefield decomposition for multicomponent data based on acoustic raytracing brought up the necessity of calibrating the stacking parameters. For the final processing of example **A** I utilized a most recent innovation based on downgoing waves which resolved this issue in an elegant way. The imaging workflow based on decomposed data was verified for its reliability up to the final sets of stacked traces and CRS attributes. A poststack depth migration being performed for one fragment of the output yielded suboptimal results which pointed out the general limitations of linear acquisition geometries. In section 5.3 I will provide a possibility to detect the failure of the 2.5D assumption for multicomponent data. A direct comparison, nevertheless, also suggested a superiority over the conventional method, i.e., prestack depth migration,

because the output showed more consistency and less ambiguity.

What remains to be done after investigation of this example is to extend the implementation towards more flexible paraxial apertures and search ranges. The benefits would be an overall improved accuracy and the reliable discrimination of the individual wavemodes.
A poststack depth migration accounting for all reflected and converted poststack traces from both walkover lines will be an interesting subject to finally estimate the consistency of the different branches for a common denominator.

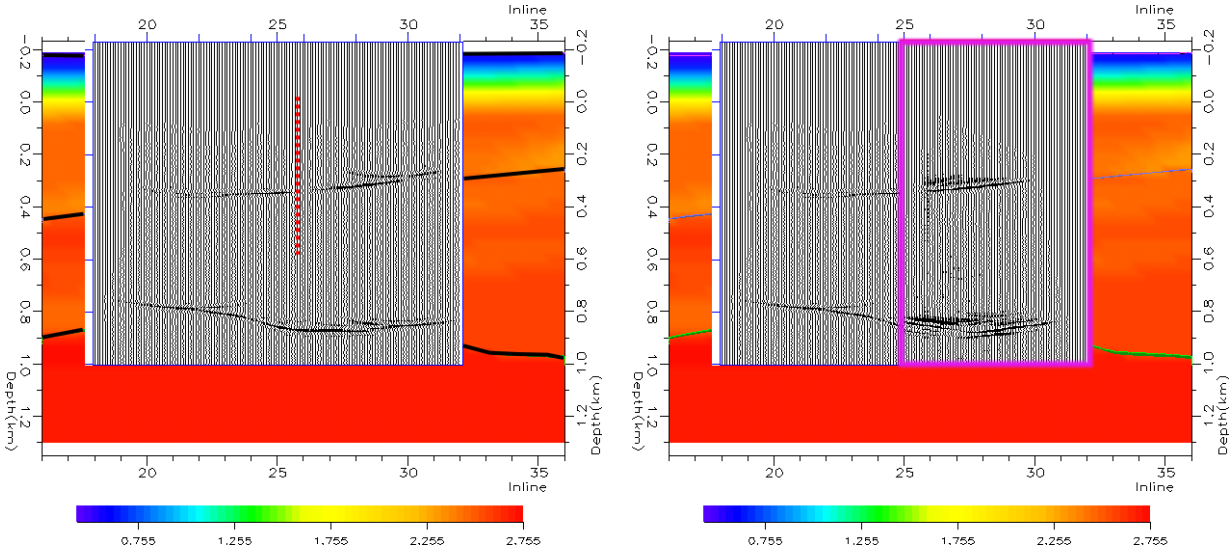

(a) Input are CRS stacked traces.

(b) Input are prestack traces (purple box).

Figure 4.12: *Result: Kirchhoff depth migration of the NS-line*

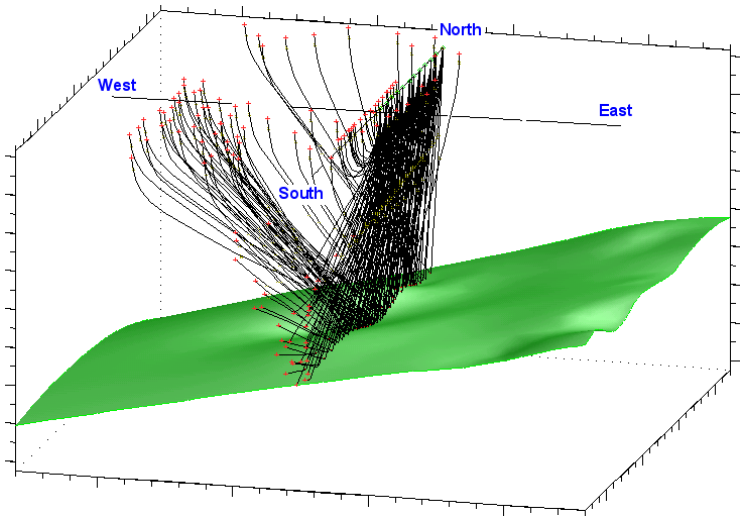

Figure 4.13: *Contradiction to a central assumption: the wave propagation in this 3D model is far from being planar particularly for the second reflector.*

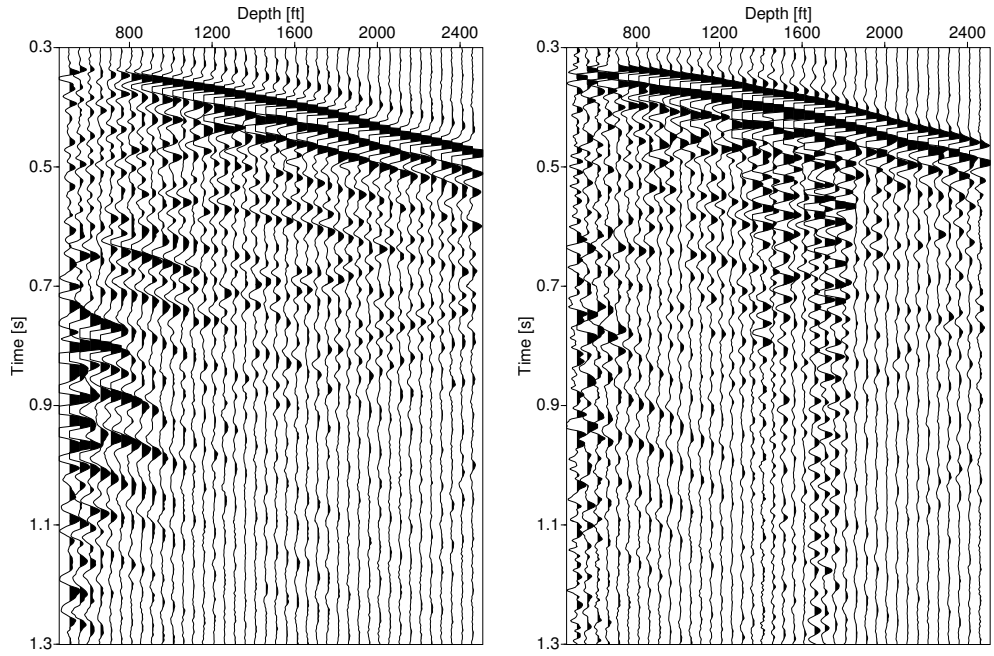

Figure 4.14: *Example common shot gather without any preprocessing. Left: vertical component. Right: inline horizontal component. The source point is located at 1500 ft offset from the wellhead.*

4.2 B: Real field data—straight vertical well

Excerpts of the processing result of this field data were firstly presented in von Steht and Goertz (2007) and speak in great favor of the CO CRS based method.

4.2.1 Data description

The real data example presented here is a walkover line that has been acquired in the San Joaquin basin near Bakersfield, California as part of a much larger 3D VSP using a tubing-deployed 40-level receiver array with 50 ft spacing. The walkover line consists of 110 Vibroseis source points with an average spacing of 50 ft and an almost straight acquisition in the North-South direction. An example CS gather of the original data without any preprocessing applied can be observed in Figure 4.14. Figure 4.16 shows the vertical and inline horizontal component for a common shot gather after deconvolution, bandpass filtering, and a surgical mute for downgoing shear waves in the f-k-domain. Even though the downgoing energy has been focused on the first-arrivals quite well for the vertical component, the result for the horizontal component can not be considered optimal. I mainly blame my lack of experience for choosing the appropriate parameters in the

filter design during deconvolution for these flaws. All of the reference gathers were recorded for a source approximately 1500 ft north of the wellhead.
Two depth-velocity curves for P- and S-waves shown in Figure 4.15 were inverted from check-shots close to the wellhead to be utilized during wavefield decomposition and depth migration.

Context	Parameter	Value
Survey description	Location	Bakersfield, CA, USA
	Contractor - Client	P/GSI - Vaquero Energy
	General survey type	Large 3D VSP survey for 8 wells
	Data used	2D subset for 1 well
		(V, H_1, H_2) components
	Source type	Vibrator
Shot and receiver geometry	Number of shots	108
	Shot interval	≈ 16.8 m
	Surface topography	± 15.0 m
	Number of receiver levels	40
	First receiver in depth	153.5 m
	Receiver interval	15.24 m
	Number of 3C traces	4 320
Recording parameters	Recording time	0.0…2.0 s
	Sampling interval	2.0 ms
	Frequency range	12-148 Hz
	Mean frequency	32 Hz

Table 4.3: *Information on the prestack data, obtained from the trace-headers prior to processing.*

4.2.2 CRS-based wavefield decomposition

Performing the first step of the attribute search in the CS domain and calibrating the resulting CRS operator with the P- and S-wave velocities at all geophone levels yields the emergence angles β_G^{P} and β_G^{S}, respectively. Rotation of the components with the above angles yields the separated PP and PS wavefield (Figure 4.17). I observe that upgoing PP energy migrates from the horizontal component in Figure 4.16 to the PP-radial orientation in Figure 4.17. I also observe upgoing P to S conversions on the PS-transverse orientation after rotation. Figures 4.20 shows the emergence angles for upgoing P reflections (left) and PS conversions (right) that have been

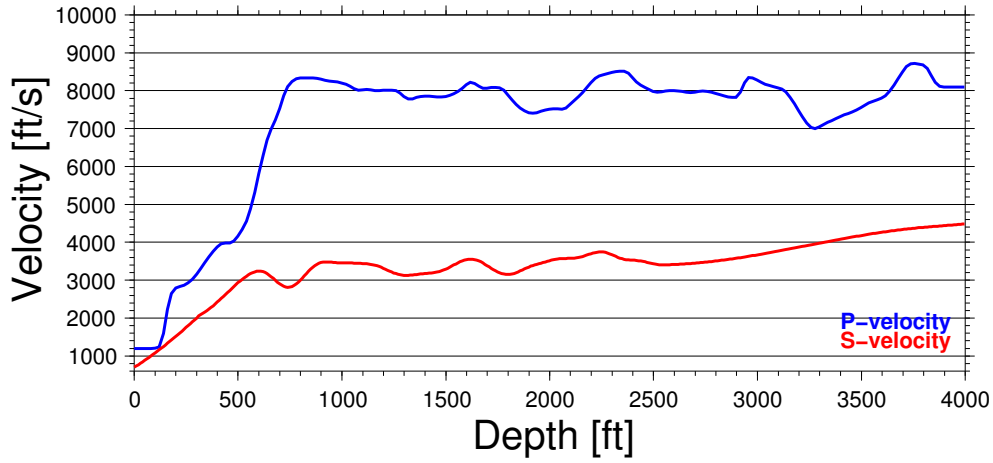

Figure 4.15: *Checkshot velocity function and local receiver velocities used for CRS wavefield decomposition and depth migration.*

used for the rotation. Note the clear distinction between upgoing PP and upgoing PS energy on both components.

4.2.3 CO CRS-processing

Figure 4.18 shows intermediate stacking results obtained by coherence analyses in CS and CR gather from the radial-oriented decomposed prestack data. These time sections serve as an input to a third coherence analysis in order to recover a complete CO CRS response from the subsurface. They share many distinct features, despite originating from opposing ends of the shot-receiver configuration to which they are tied to. The stacking result for the complete walkover line for upgoing PP reflections as well as for upgoing PS conversions can be observed in Figure 4.19. The displayed section is now in the qCO domain: each trace is plotted at the respective shot location and represents a different source and receiver location. The outermost traces represent the shallowest receiver level. As I move towards the center of the section (wellhead), I also move to deeper receiver locations along the array until I reach the lowermost receiver level. The center part of each section (from ≈ -500 ft to 1000 ft offset) represents the near-offset shotpoints recorded in the lowermost receiver level. The CRS-stacked VSP time sections exhibit a greatly increased signal-to-noise ratio compared to the rotated prestack data of Figure 4.17, particularly for the upgoing converted waves. Accompanying the stacks are sections of the five kinematic wavefield attributes that can be used for further processing steps. As an example, I show in Figure 4.21 the geometrical spreading which has been calculated from the parameters associated with the CRS stacked section for PP reflections of Figure 4.19.

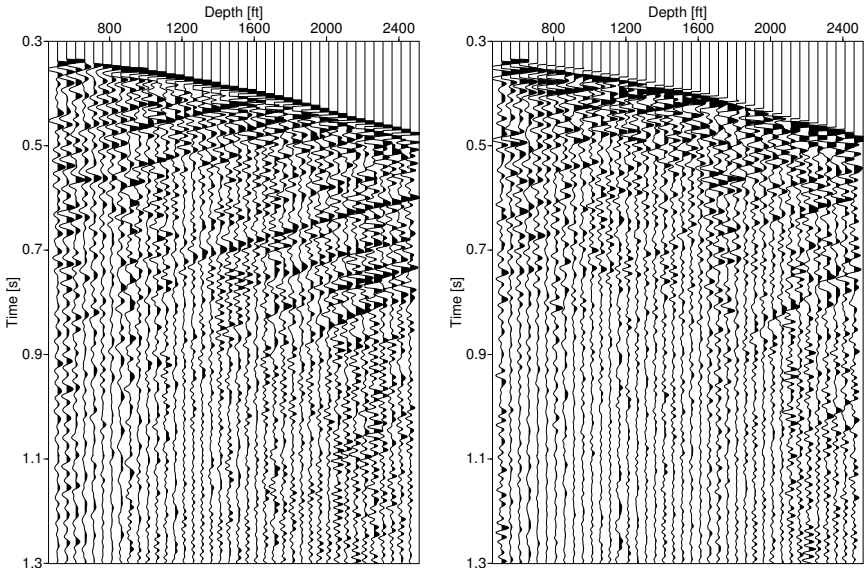

Figure 4.16: *Example common shot gather after preprocessing (deconvolution) and before wavefield decomposition. Left: vertical component. Right: inline horizontal component. The source point is located at 1500 ft offset from the wellhead.*

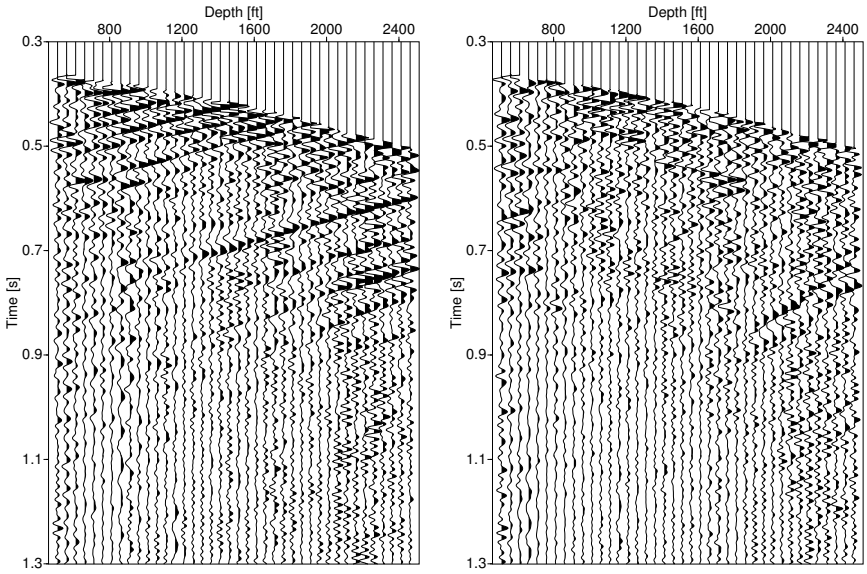

Figure 4.17: *Example common-shot gather after wavefield decomposition. Left: Radial orientation for upgoing PP reflections. Right: inline transverse orientation for upgoing PS conversions. The source point is the same as in Figure 4.16.*

4.2.4 Depth migration and conclusions

Since the CRS-stacked VSP time and attribute sections shown in Figure 4.19 and Figure 4.21 are obtained in the quasi-common-offset (qCO) domain, any interpreter will have a hard time characterizing the subsurface at this stage. I therefore apply a Kirchhoff poststack depth migration to the CRS-stacked qCO section using the velocity profile shown in Figure 4.15. When post-stack migrating data from the qCO domain, it can happen that areas above the lowermost receiver level and close to the well are not optimally illuminated. To avoid gaps in the illumination, I augment the qCO section with an additional stacked common-receiver section for the topmost receiver level for migration. The result from the poststack Kirchhoff migration of the augmented qCO section for both wave modes is shown in Figure 4.22. For comparison, I also applied a full prestack depth migration using the same velocity model and migration aperture without any CRS processing beforehand (Figure 4.23). All images have been top-muted and gained with a $t^{1.5}$-gain. Despite the use of only a 1D velocity function for migration, I observe a considerable structural variation across the image. The post-CRS-stack migration shows a better overall lateral continuity, particularly at the target level (between 3,000 and 4,000 ft) and below. A poststack migration is generally less susceptible to errors in the velocity model, compared to a prestack migration. For the poststack migration, the traces have already been stacked in a data-driven way by the CRS stack without the need for a velocity model. The image is less likely to defocus due to destructive interference, because I have decoupled the stacking from the depth mapping process. The prestack migration, on the other hand, is subject to defocusing due to likely inaccuracies in the velocity model, particularly if only a 1D velocity model is used. The problem is further exacerbated by the typically higher frequency content of VSP data compared to surface seismic data.

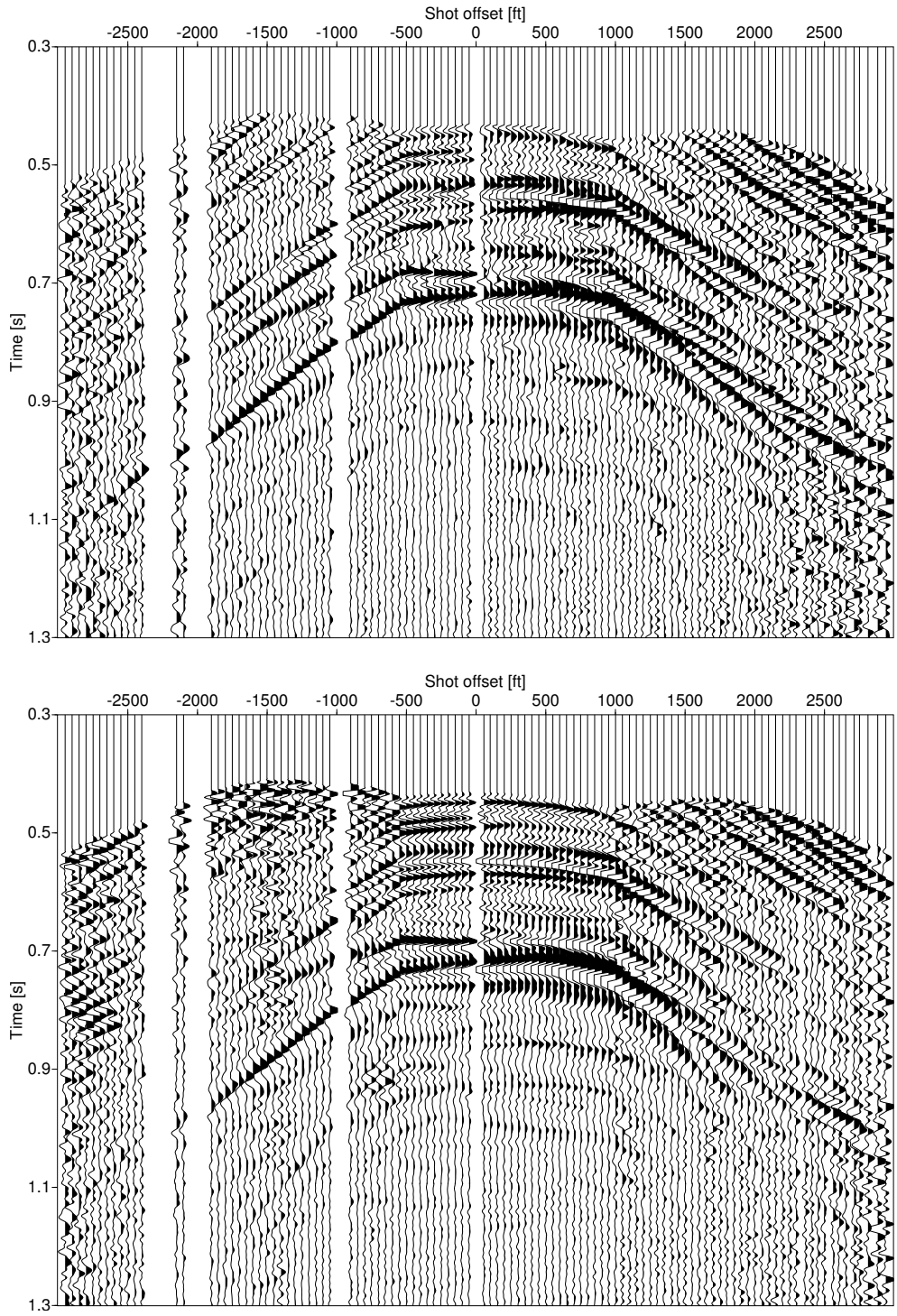

Figure 4.18: *The intermediate CS/CR stack results are simulated qCO sections as depicted in Figure 4.1.3. Top: CS-stacked qCO section for upgoing PP reflections. Bottom: CR-stacked qCO section for upgoing PP reflections.*

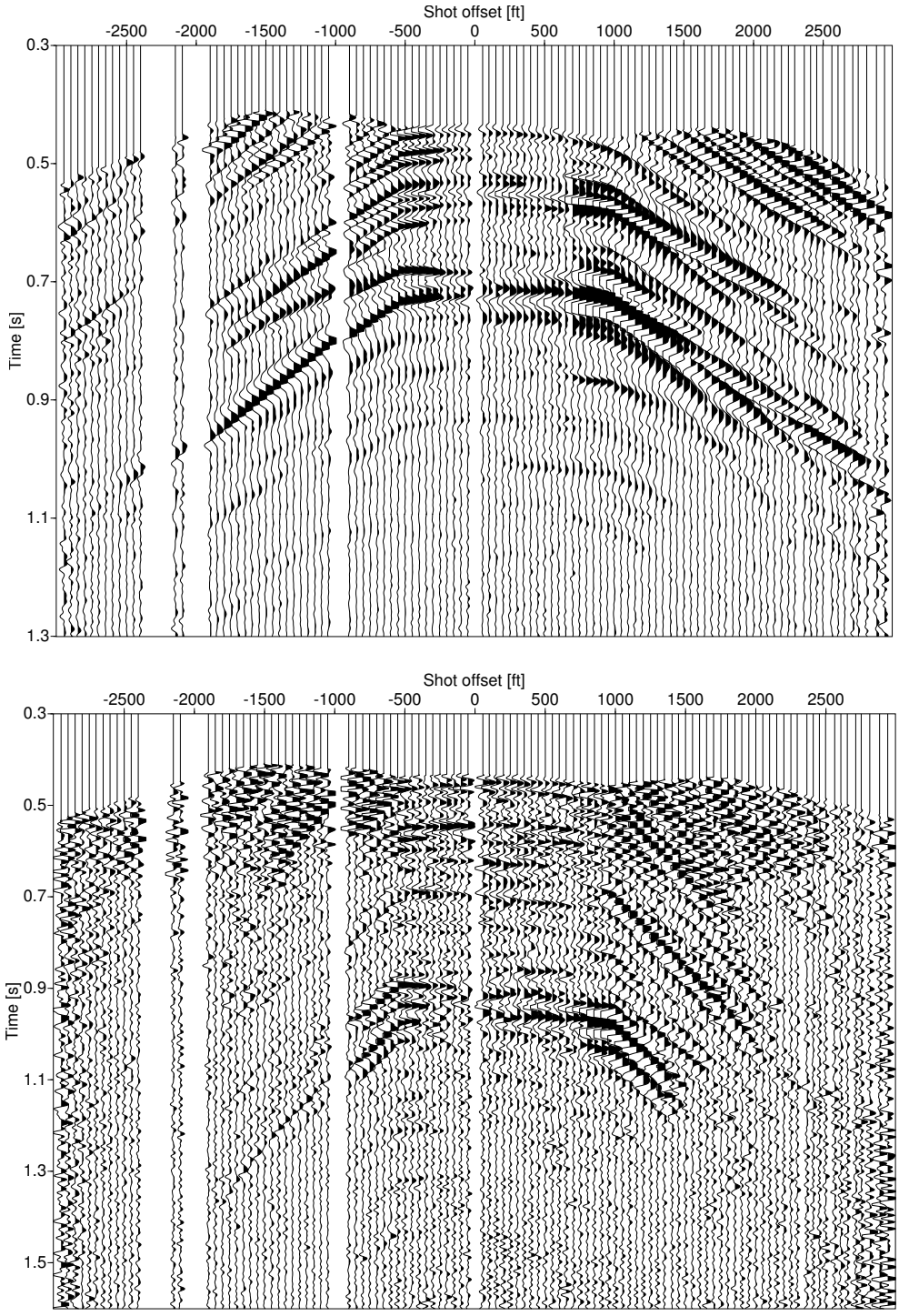

Figure 4.19: *The CRS stack result is a simulated qCO section as depicted in Figure 4.1.3. Top: CRS-stacked qCO section for upgoing PP reflections. Bottom: CRS-stacked qCO section for upgoing PS conversions.*

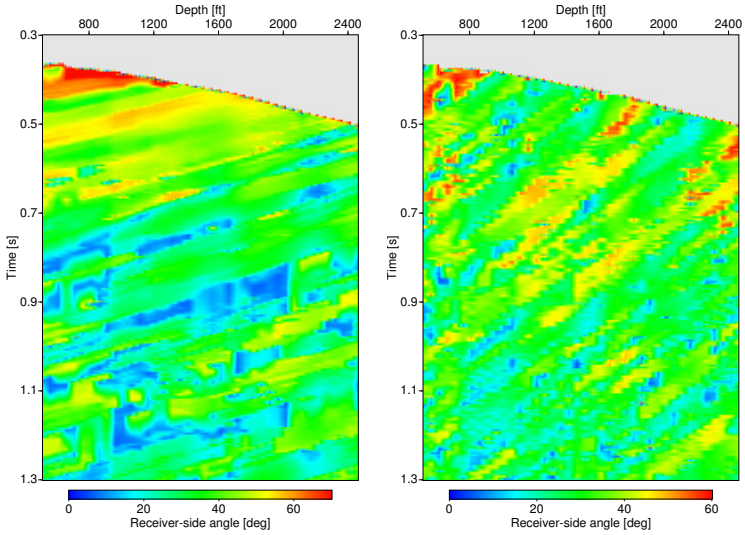

Figure 4.20: *Example CRS attribute section (common-shot domain) used for the CRS-based wavefield decomposition. Left: Emergence angle for upgoing P-waves. Right: Emergence angle for upgoing PS converted waves. The source point is the same as in Figures 4.16 and 4.17.*

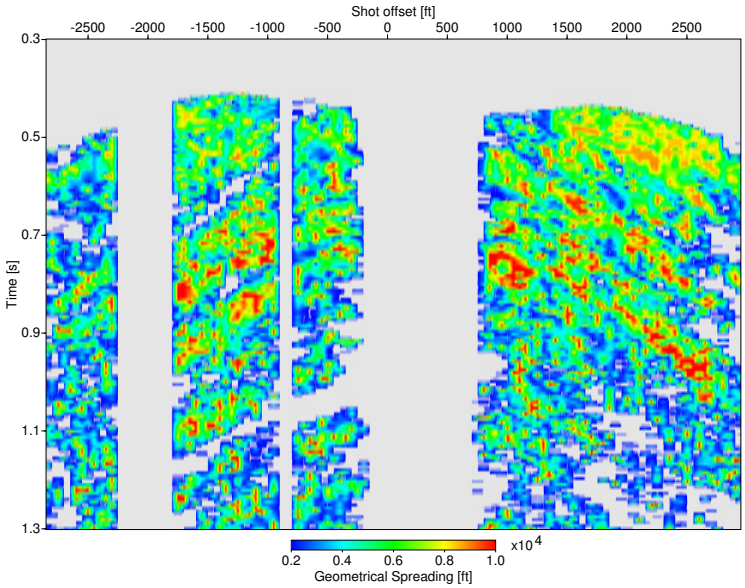

Figure 4.21: *Example wavefield property—Geometrical spreading—calculated from the CRS attributes associated with the stack result for the PP-radial orientation shown in Figure 4.19. Areas of low fold in aperture and low coherence are masked.*

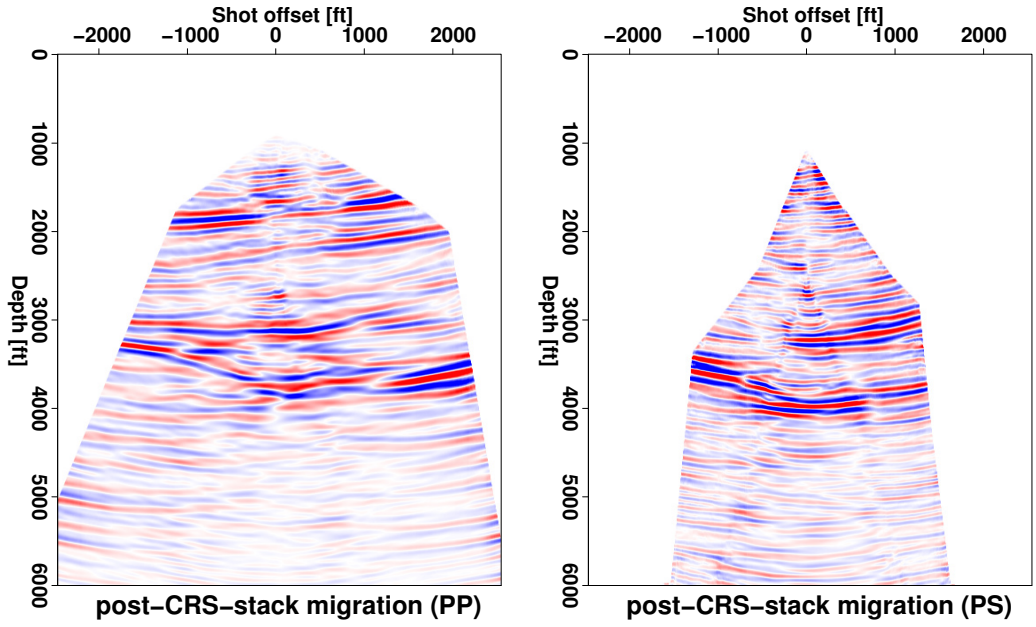

Figure 4.22: *Result of Kirchhoff PostSDM applied on the CRS-stacked section using the 1D velocity profile of Figure 4.15. Left: PP image, Right: PS converted image*

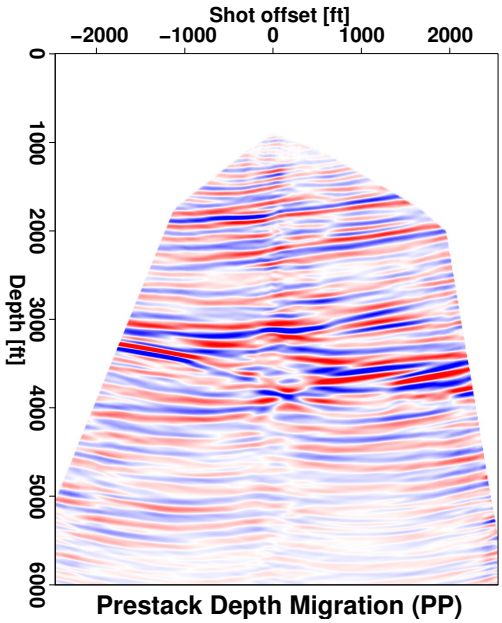

Figure 4.23: *Result of prestack VSP Kirchhoff depth migration.*

Context	Parameter	Value
Modeling parameters	Used method	Isotropic, elastic, finite difference modeling in 3D extracted (V, H_1) components
	Depth model	2.5D, mainly based on homogeneous layers
	v_P/v_S ratio	$\sqrt{3}$
	Signal-to-noise ratio	20
Shot and receiver geometry	Number of shots	100
	Shot interval	30.48 m
	Surface topography	$\pm$50.0 m
	Number of receiver levels	40
	First receiver in depth	537.2 m
	Receiver interval	15.24 m
	Number of 2C traces	4000
Recording parameters	Recording time	0.0...2.0 s
	Sampling interval	2.0 ms
	Frequency range	5-80 Hz
	Mean frequency	35 Hz

Table 4.4: *Information on the prestack data, as specified by the survey and modeling parameters.*

4.3 C: Synthetic seismic data—deviated well

Today, more and more deviated wells are employed in the exploration of a prospect with the intention to eventually maximize hydrocarbon recovery. This tendency was simplified through the method of *directional drilling* being improved steadily. In order to verify the CO CRS method to be applicable to VSP data originating from geometries which differ from straight vertical settings, I generated a synthetic data example specifically for this task.

4.3.1 Data description

Figure 4.24 gives an impression of the depth-velocity model and survey parameters which were set up in the framework of the NUCLEUS software package. It was confirmed through written correspondence with industry professionals that the design of the well can is suitable for a realistic initial trial. The deviation of the borehole with increasing depth picks up very slowly

and finishes in an almost horizontal slope with a projected distance of about 200 m to wellhead and a final depth of 1 km. A comparably mild top-surface topography—the elevation changes monotonously over 100 m—was added to the shot profile which has a total length of approximately 3 km. Substantially more difficulties were encountered for the choice of an appropriate depth-velocity model. At first, I expected an elastic raytracing, similar to example **A**, for almost homogeneous layers in a 2.5D medium and the underlying survey geometry to be a rather small challenge for a conventional software. Due to the oblique angles of incidence and reflection one commonly encounters in VSP surveys, which is worsened by the sharp edges of homogeneous layering, however, continuous reflection events could not be recovered in the raytracing with NORSAR routines.

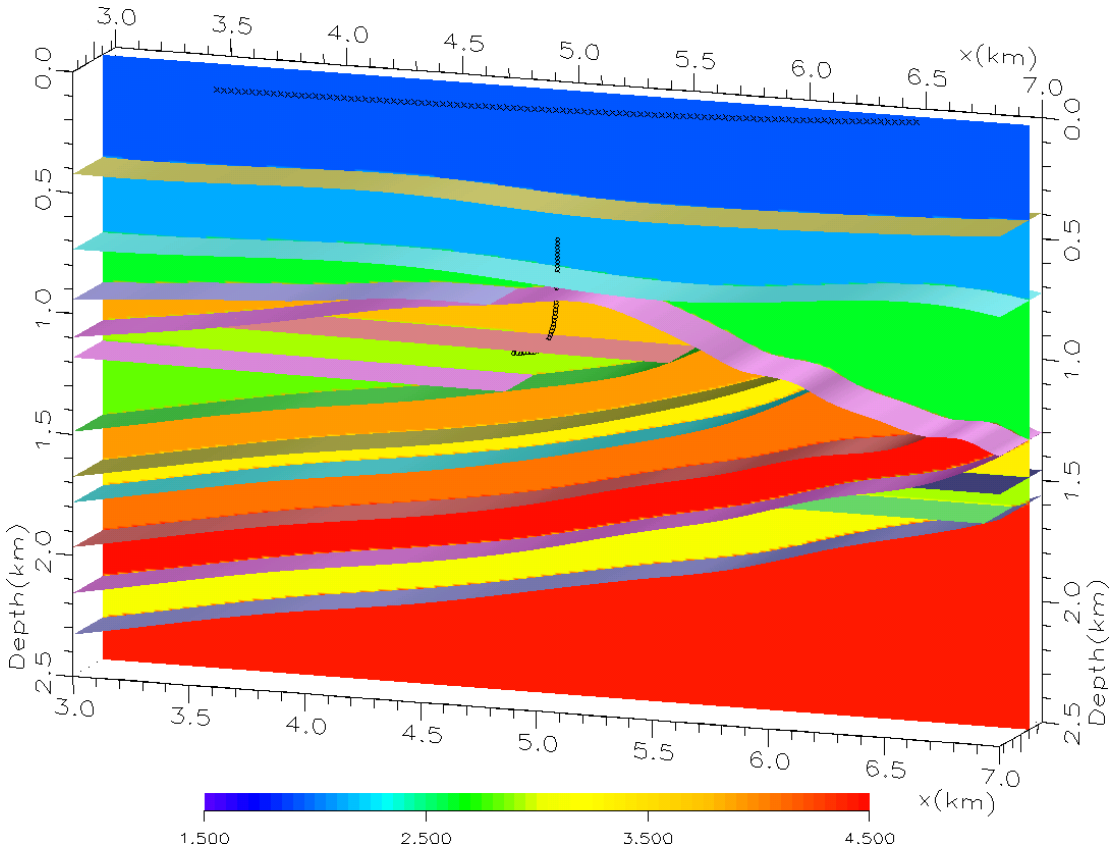

Figure 4.24: *Depth model and survey geometry used to generate seismic data.*

Then, an alternative way of generating synthetic seismograms was pursued by reverting to viscoelastic finite-difference modeling which is also part of the NUCLEUS software. It is capable to simultaneously model all wave modes including multiples, converted waves, diffractions and interbed multiples because the full wave equation enters into the calculations. For a preliminary

test of a new method this can be considered a negative aspect since I have no opportunity to selectively eliminate undesired events via a ray code. In Table 4.4 the most important information about the hereby simulated seismic data is compiled.

I additionally want to give an impression of how the shape of reflection events is different for

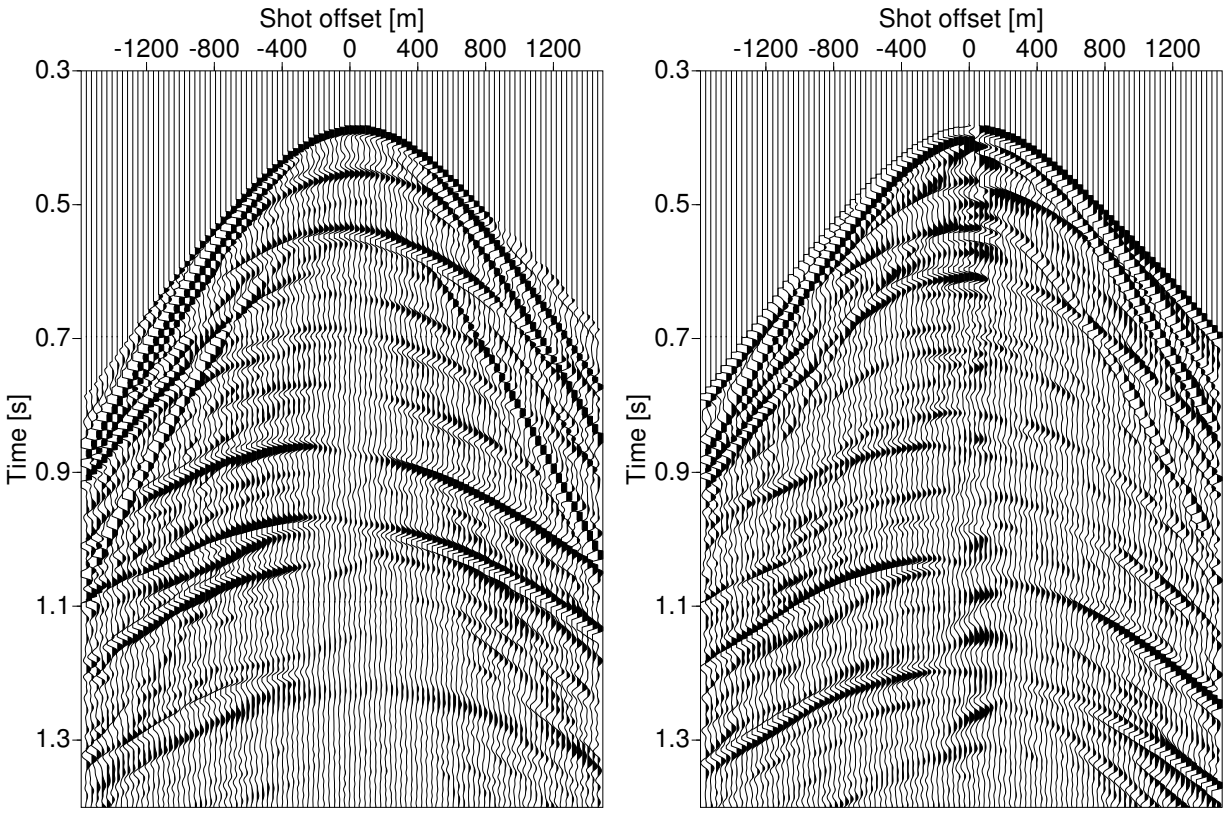

(a) V-component (b) H_1-component

Figure 4.25: *Common receiver gather at 800 m depth.*

a deviated well over a vertical well. The common-shot gathers provided in Figure 4.26 were generated by shots being placed 750 m from either side of the wellhead. For the lower receiver levels both gathers differ substantially in their arrival time because the deviated borehole points in direction of the positive offsets. One also can notice several kinks appearing along the reflection events at exactly the positions where two layers of the velocity model meet. These kinks will cause further complications for the coherence analysis in the first search step as will be explained in the next section. Furthermore I found it difficult to identify the first arrivals of the downgoing waves especially for the lower levels of the large-offsets gathers since reflected waves were traveling much faster and appeared earlier in the seismograms. An account of the inline two-component common-receiver gathers at a depth of 800 m is given in Figure 4.25. The asymmetry which was observed for the CS gathers does not transport over to the CR configuration and

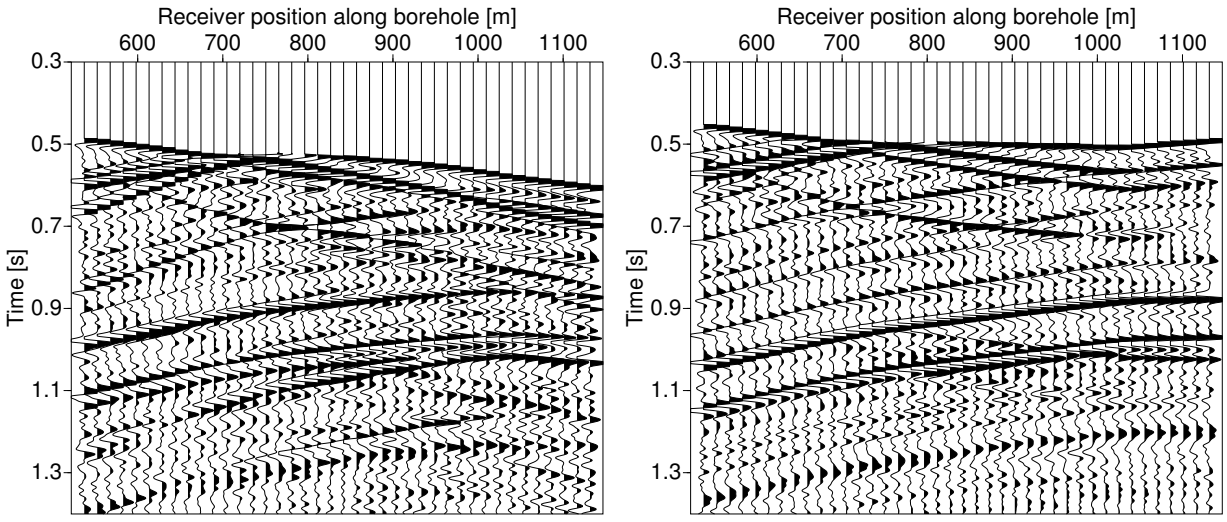

(a) V-comp. - shot offset −750 m (b) V-comp. - shot offset 750 m

Figure 4.26: *Two common-shot gathers from opposite sides of the walkover line.*

naturally, there are no kinks observable alongside of the reflection events. The near-offset area of the principal horizontal component shows a contamination by low-frequency reverberations which might be caused by my choice of a very narrow modeling space in crossline direction—thus, being artifacts which can be avoided in future modeling projects.

4.3.2 CRS-processing

A preprocessing of the synthetic data mainly aiming at the removal of downgoing and refracted energy had to be omitted, due to the lack of a suitable software to achieve this and limited amount of processing time towards the conclusion of my studies. In this way the CO CRS-based wavefield decomposition was not considered for this data but exceptional emphasis was placed on the recovery of a satisfactory, yet, preliminary imaging result for the V-component with respect to PP-reflections.

As a result of that, the data was divided into two subsets with respect to the upper and lower 25 receiver levels, resembling an almost vertical array for the shallow and a truly deviated array for the deep part. The central overlap by 10 receiver levels was chosen intentionally to later achieve a better correlation between results stemming from both imaging procedures. For fifty shot points being placed on either side of the walkover line and a similar bilinear relation being chosen as for examples **A** and **B** (see, Figure 4.1.3) the consequence would have been an inadequate illumination of the near-offset region. To avoid this a shot-receiver distribution as in Figure 4.27 was chosen for both subsets. Therefore, two neighboring shot positions share one receiver level

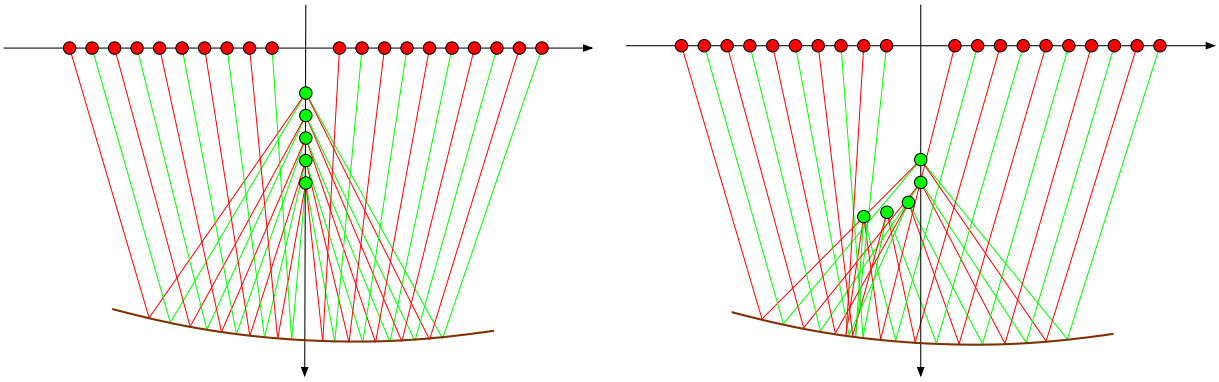

(a) Straight-well part. (b) Deviated-well part.

Figure 4.27: *Geometry map explaining the relation of the expansion points. The combination of source and receiver positions resembles a qCO geometry with two neighboring source points connecting to one receiver level.*

which of course quietly assumes another subdivision of each data by even and odd shot indeces. By following this subdivision the CO CRS workflow was exercised four times, altogether. Then, the subdivided results were merged again to form the final sets of stacked traces for the shallow and deep sub-array as shown in Figure 4.28. The temporal "stair-structure" introduced into the bilinear relation by connecting two shot points with one receiver does not affect the continuity of the reflection events too much but should be kept in mind. The processing was able to recover the reflectors situated below them in a very continuous manner with even two of the pinch out structure clearly visible. The more shallow events were, once again, moved to the outer flanks, are of much less quality, and mainly covered by noise from refracted energy.

A mayor difficulty throughout this processing was caused by the already-mentioned "kinks" being present across reflection events in CS gathers. Because of reflection events not being differentiable over a sufficiently wide aperture it was impossible to use the model-based (blue, dashed) curve for velocity calibration as shown in Figure 4.29. Its too resticted variation of the moveout curves during coherence analysis resulted in the CS search to mainly choose local edge-maxima and proved generally to be unstable. Two different velocity curves created on the basis of the original curve scaled by the factor 0.9 were calculated to counteract this problem. Firstly, a Bezier spline was fitted to the curve (magenta, dotted) and showed a much more stable behavior with still considerable control available over the search-limits. Secondly, the normal-moveout velocity for all depth levels was estimated (cyan, dashed-dotted). This curve was able to provide a more consistant stacking result in terms of energy even across the problematic ranges of the reflection events and served as a basis for the final CRS stacking result. Note, that the stacking parameters recovered from this analysis were of course are not suited to perform, e.g., a

wavefield decomposition, anymore. A subsequent rescaling towards the actual interval velocity is able to partially recover them, eventually.

4.3.3 Conclusions

Velocity models based on homogeneous layering are not particularly suited to verify approaches relying on coherence analysis, e.g., the CO CRS method, unless the recording array remains within the same layer. Sharp velocity contrasts causing indifferentiability along reflection events cause difficulties in any ray-based approach and should be treated with great care.
The choice of a larger shot interval compared to the receiver interval seems to have benefited the resolution of the central area but might as well be favored by the velocities chosen in the model. A look at the number of traces contributing to the stacking aperture of the shallow sub-array is provided in Figure 4.30 and suggests that the number of considered traces in the central area was too high. A more balanced design for the control of the aperture is desired.
The CRS-based wavefield decomposition and a comparison of Pre- and PostSDM can, once again, provide a good assessment of the performance of the method.

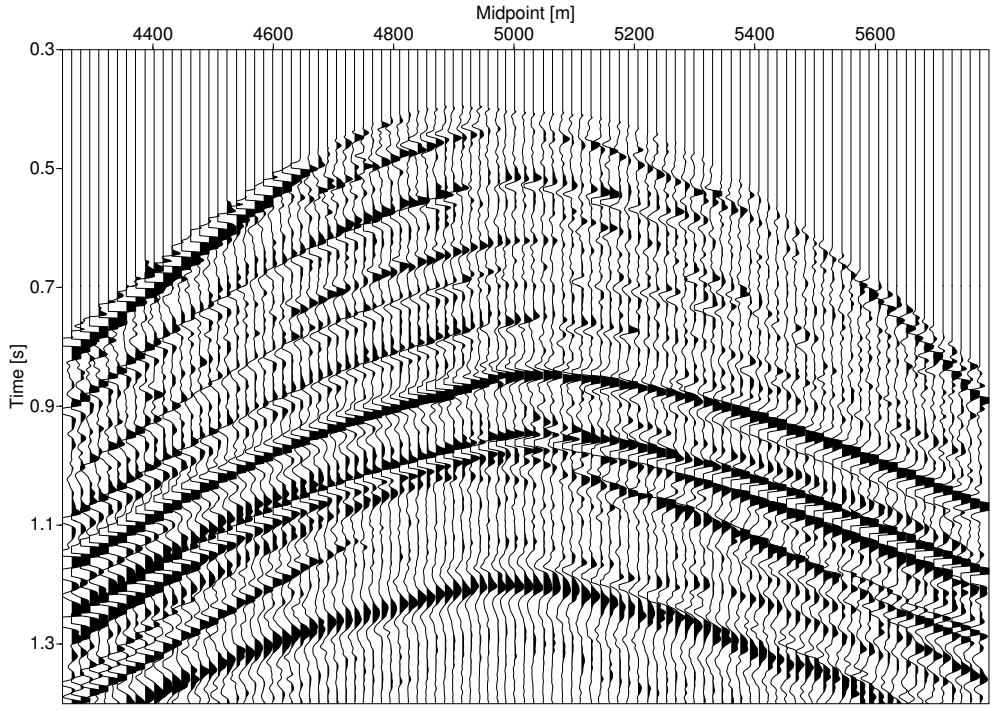

(a) Step 4: CRS stack according to Map 4.27(a).

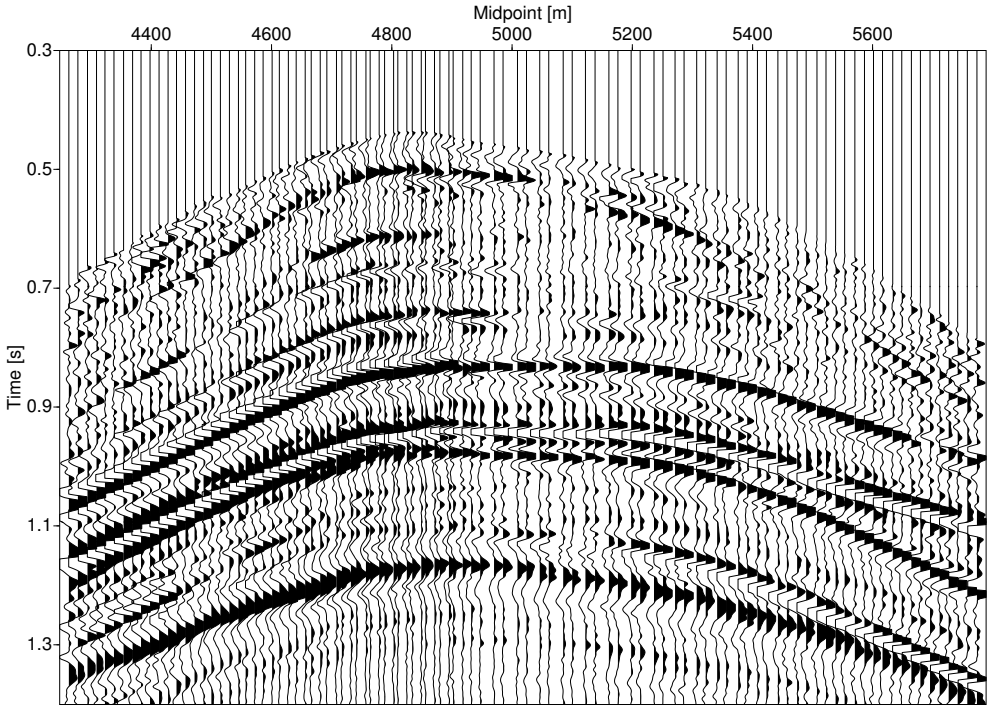

(b) Step 4: CRS stack according to Map 4.27(b).

Figure 4.28: *Result: qCO stacked traces for PP reflections. The estimation of the quintet of CRS attributes was performed on the raw vertical component of the data.*

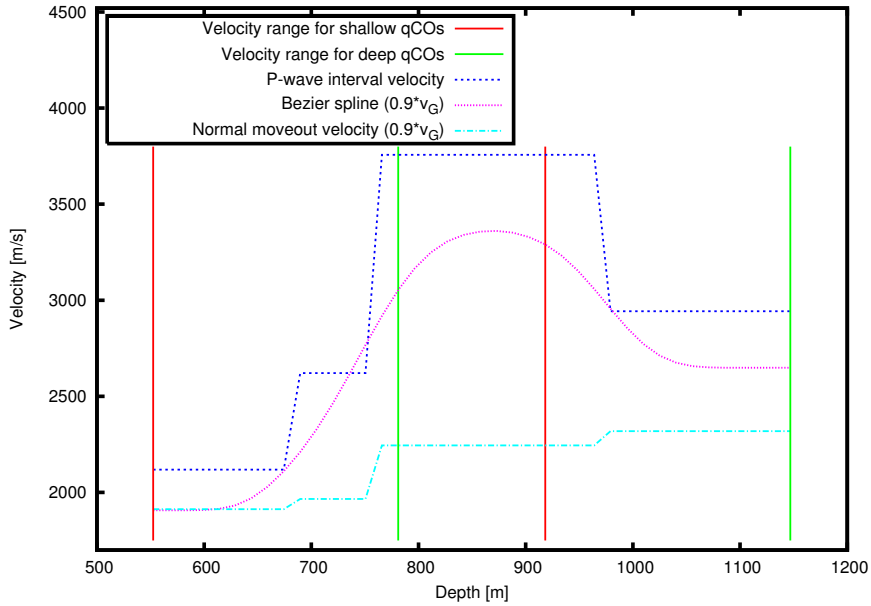

Figure 4.29: *Depth-velocity curves used for calibration.*

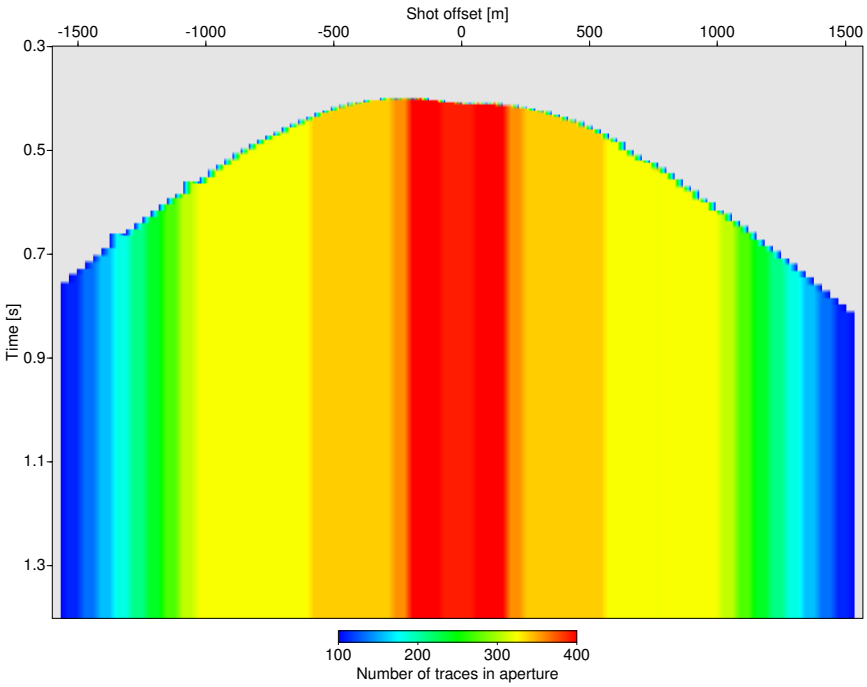

Figure 4.30: *Result: number CRS-stacked traces for the shallow sub-array.*

Chapter 5

Promising new directions

Throughout my work on the subject of developing a poststack imaging scheme the clearly defined goal was standing out at some distance but the path leading towards it was not clearly visible for most of the way. Progress was made by advancing stepwise, probing different directions, and choosing the more appropriate solutions. In some occasions the solutions I considered to be less suitable just appeared in the wrong place and time but have to be mentioned for future application.
Most of the observations were made for the special case of a borehole acquisition geometry but several also had implications when being transfered to other specialized geometries, e.g., surface seismics, OBC, OBS. Therefore, the spectrum of this thesis has become much wider than initially anticipated. Due to the lack of time I was not able to go into adequate detail regarding a definite exploitative value for many of the following "ideas", but nevertheless I strongly encourage their further investigation.

5.1 Surface seismics revisited

My current implementation of the CO CRS stack is not only capable of handling VSP walkaway data. With a little additional programming effort—mainly, with focus on the binning of the input data—I was able to extend it back towards the origin of the method, serving as an alternative imaging tool for surface seismic data. One might prematurely raise the question of signification since there has already been reported considerable research on this matter, being described in, e.g., Zhang (2003).
A first justification for returning to the subject is the combination of common-offset stacking with the handling of top-surface topography distorting the line of acquisition. The CRS traveltime

operator (3.6) being used now is significantly more universal than the ones chosen for earlier approaches. Having worked with complicated field data for some time now I see an even more important issue being circumvented by following the workflow introduced in section 3.4. The more complicated the data become the less suitable the binning in common-midpoint gathers will be. Complication in this case can either be caused by severe near-surface problems, i.e., topography or a heterogeneous weathering layer, or a complex stratigraphy with strongly-dipping interfaces. Eventually for those cases the CMP-assumption will not hold any longer. The traces shared by one and the same gather bear no more likeness from which a traveltime response could be recovered.

Returning to my approach based on the foundation of dividing the search steps in common-shot and common-receiver gathers I will now provide a short feasibility study. The field data being processed in this study was kindly provided by **Saudi Aramco** and is a life-like example of single-component onshore field-data under the presence of significant near-surface complications.

Context	Parameter	Value
Shot and receiver geometry	Number of shots	1315
	Shot interval	30 m
	Receiver interval	30 m
	Top-surface elevation	461…595 m
	Number of traces	306960
Midpoint and offset geometry	Number of CMP bins	2839
	Maximum CMP fold	120
	Full offset range	-3602…-72 m, 50…3607 m
Recording parameters	Recording time	2 s
	Sampling interval	4 ms
	Mean frequency	30 Hz
	Maximum frequency	60 Hz

Table 5.1: *Information on the prestack data, obtained from the trace-header information prior to processing.*

The total length of the seismic line was approximately 40 km, with some of the acquisition parameters being compiled in Table 5.1. The top-surface elevation fluctuates within a total of 150 m, which is not too much for such a long profile. But the elevation-changes are very acute indicating

several trenches carved by erosive forces making this data set a suitable candidate for the method. Unfortunately, I was unable to obtain any additional information on the conducted measurements, e.g., an estimate of weathering velocity along the profile. Furthermore, the data was delivered in its raw form, an remained that way during the CO CRS processing. The shot and receiver configuration was chosen in a way that the *full offset* distance in-between them measured $\approx 2300\,\mathrm{m}$. From looking at the prestack data I observed that the S/N ratio at this distance was high enough to qualify it for coherence analysis without further preprocessing. The ground roll cone was also not too influential in its tendency to cover the reflection events. For the sake of completeness and comparableness I found it necessary to perform the whole workflow individually for a positive and a negative offsets.

During the first search step it became evident that the calibration of each individual shot and receiver point to realistic near-surface velocities would have improved the stacking result, considerably. As a proof of this claim I present various stacked common-offset sections obtained after the initial common-shot search which are displayed in Figure 5.1 for positive and Figure 5.2 for negative offsets. The near-surface velocity was set constant at two arbitrary values (to $v_S = 800\,\frac{\mathrm{m}}{\mathrm{s}}$ and $v_S = 1600\,\frac{\mathrm{m}}{\mathrm{s}}$) serving as rough estimates of upper and lower bounds for which the search/stack still worked satisfactory. As can be seen the fitting calibration velocity at the right spot with a reasonable choice of search limits for angle and curvature yielded an improved stacking result over choosing an incorrect velocity. Arrows placed at various positions in Figures 5.1 and 5.2 indicate some very prominent improvements. As a first conclusion the ideal calibration velocity-curves for both shot- and receiver-searches should be chosen variable. A refraction-static analysis which is part of conventional processing will provide a good estimate for these curves.
Another thing can be observed very clearly, even by merely looking at the intermediate stacking result for equal calibration velocities, respectively. Positive and negative offsets ranges yielded different levels of detail for different regions despite of having an identical overall distance. In case of zero-offset imaging this duality is mostly eliminated an it remains more a matter of luck whether the additional information will be introduced into the final image.

Afterwards the full processing workflow was performed for both offsets at a fixed near-surface velocity of $v_S = v_G = 1600\,\frac{\mathrm{m}}{\mathrm{s}}$. Apart from the stacking parameter which will be of no further concern here, again, two CO CRS stacked images were obtained. I directly compared the result for positive offsets (see, Figure 5.3(b)) with the raw traces, as seen in Figure 5.3(a), which were extracted for this particular range directly from the prestack volume. Both section share many similar features but the stacked image largely dominates in terms of S/N ratio and removal of ambiguity. One also has to keep in mind that the velocity calibration was chosen suboptimal and an even better processing could be performed if more time was invested.
For the negative offsets' result a different benchmark for the assessment of its quality was chosen

which I consider even more striking than the previous. A *zero-offset* CRS stacking result created under specific consideration of the topography of the acquisition geometry as it was firstly presented by von Steht (2004) is displayed in Figure 5.4(a). Unfortunately, this image does not cover the whole extent of the profile. However, the illuminated regions should still correspond in their surface coordinate when being compared to CO CRS stacking result for negative offsets in Figure 5.4(b). Obviously, the images bear little resemblance but this must be naturally the case, since two totally different ray-configurations were simulated in the underlying processes. Both methods share the same disadvantage of an unknown near-surface velocity which was selected as a reasonable constant. An advantage in favor of the zero-offset stacked image is the underlying preprocessing which included spiking deconvolution, giving reflection events a higher frequency look. Apart from that, the performance of the CO CRS stack can be considered far superior over the zero-offset result. Reflector continuity is much better preserved even reaching across the three gaps which can be spotted in Figure 5.4(a) where the CMP-assumption obviously breaks down.

What remains missing from that point on is a depth migration of both of the common-offset images which would make it easier to rate the performance of this method with respect to exiting processing schemes. From the researcher's perspective, nevertheless, I believe that a further investigation of this subject is most justified.

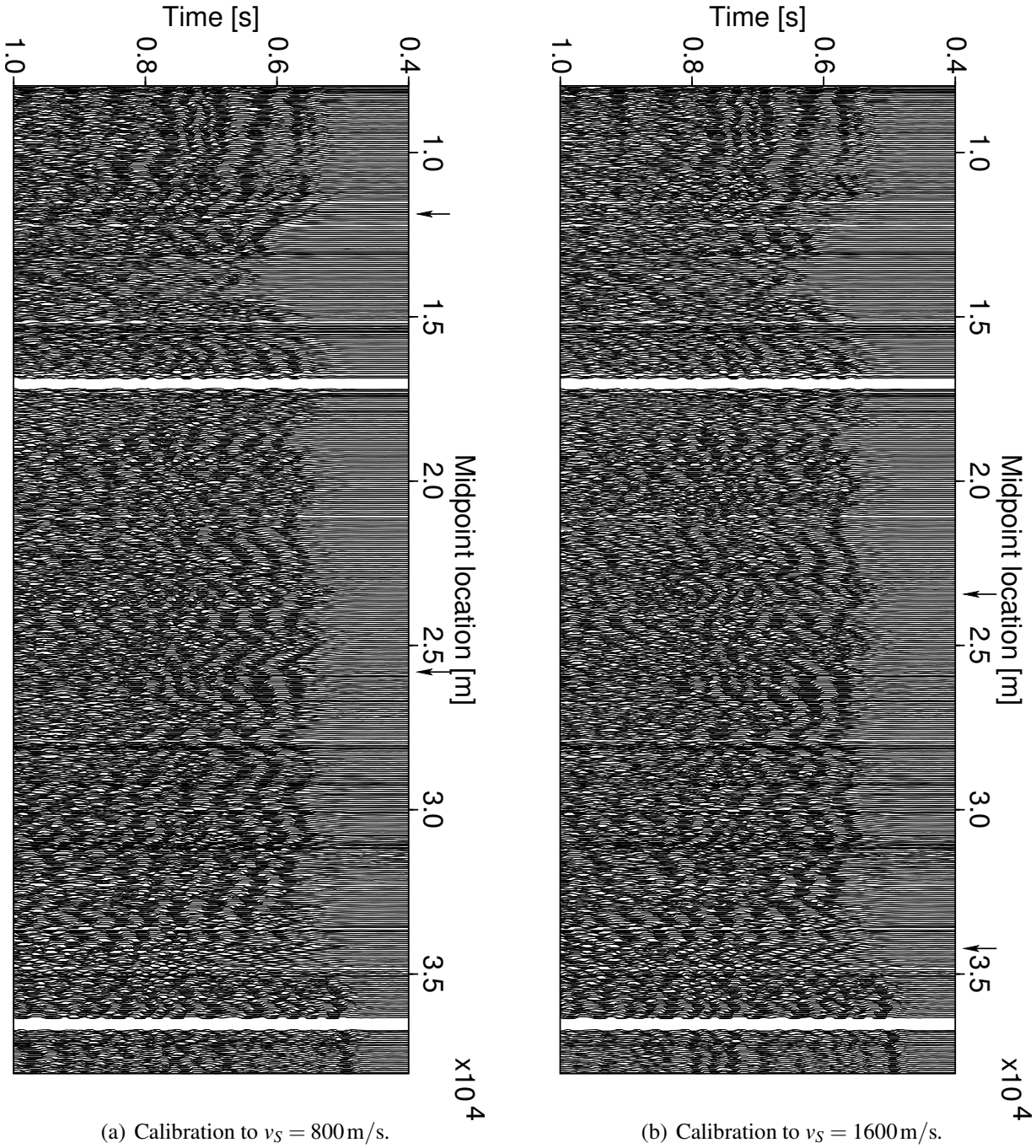

(a) Calibration to $v_S = 800\,\mathrm{m/s}$.

(b) Calibration to $v_S = 1600\,\mathrm{m/s}$.

Figure 5.1: *Surface seismic for topography - stacked CS gathers for common offsets* $\approx +2300\,\mathrm{m}$ *and two different calibration velocities* v_S.

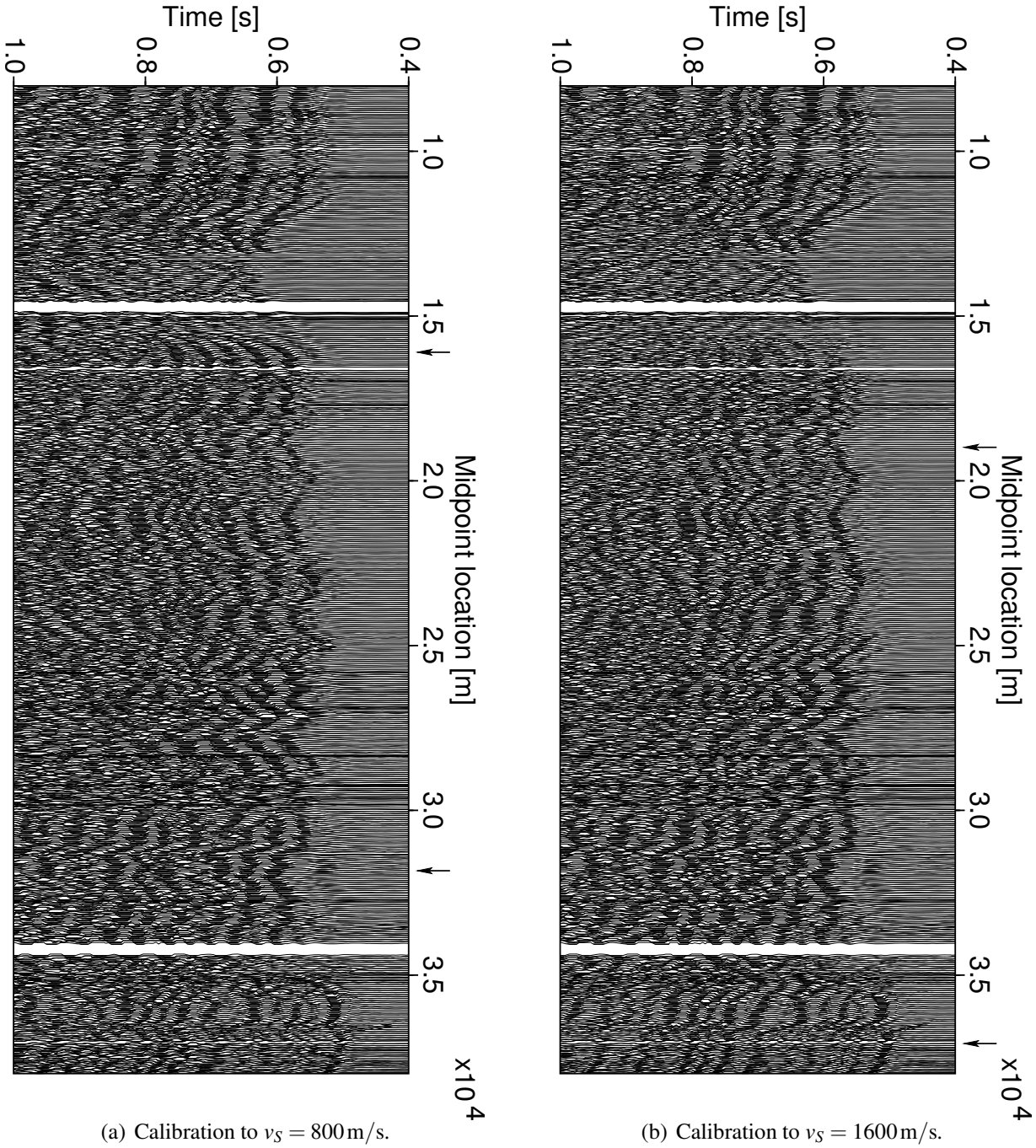

(a) Calibration to $v_S = 800\,\mathrm{m/s}$.

(b) Calibration to $v_S = 1600\,\mathrm{m/s}$.

Figure 5.2: *Surface seismic for topography - stacked CS gathers for common offsets* $\approx -2300\,\mathrm{m}$ *and two different calibration velocities* v_S.

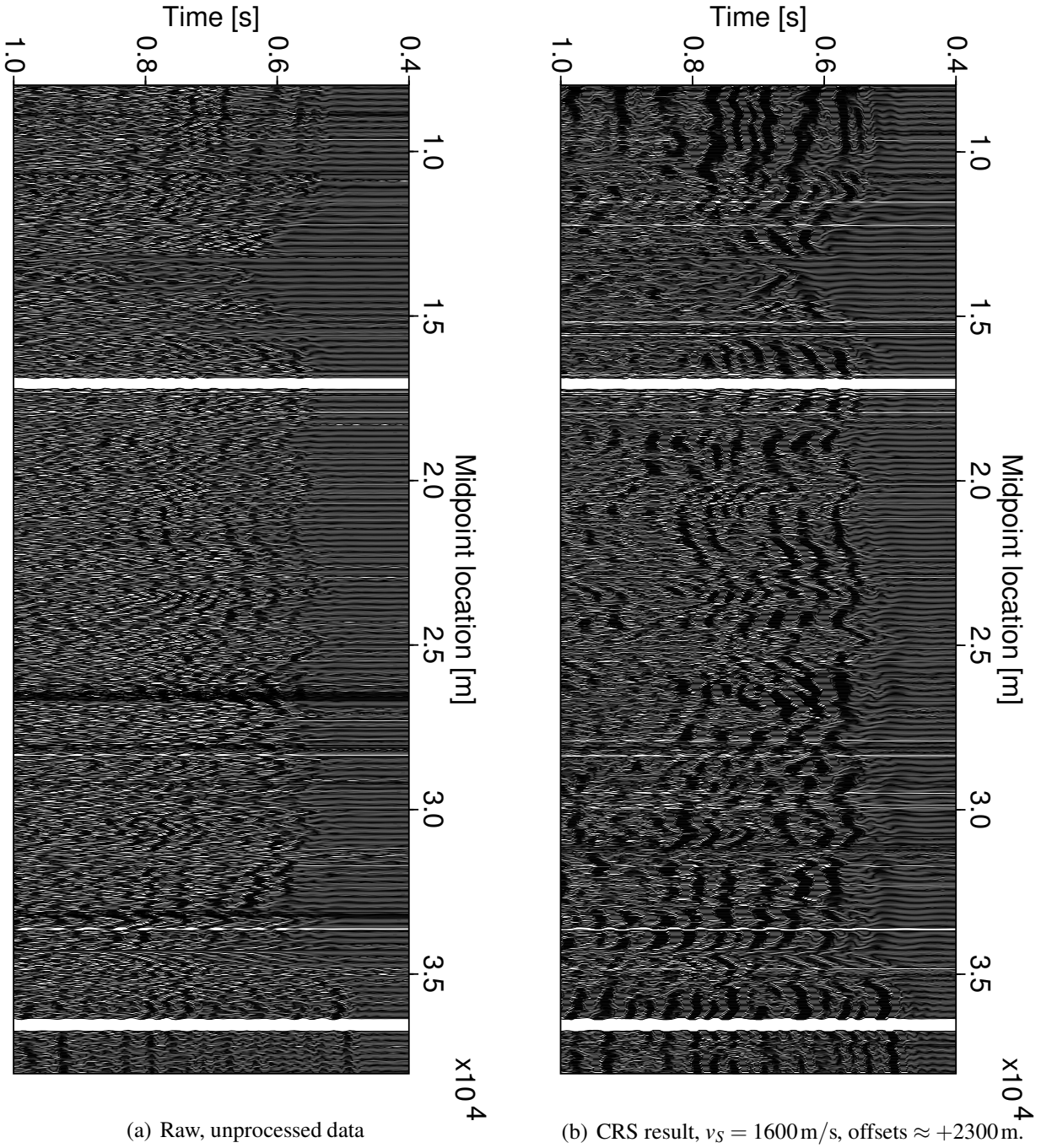

(a) Raw, unprocessed data

(b) CRS result, $v_S = 1600\,\mathrm{m/s}$, offsets $\approx +2300\,\mathrm{m}$.

Figure 5.3: *Surface seismic for topography - Raw data vs. CRS-stacked traces.*

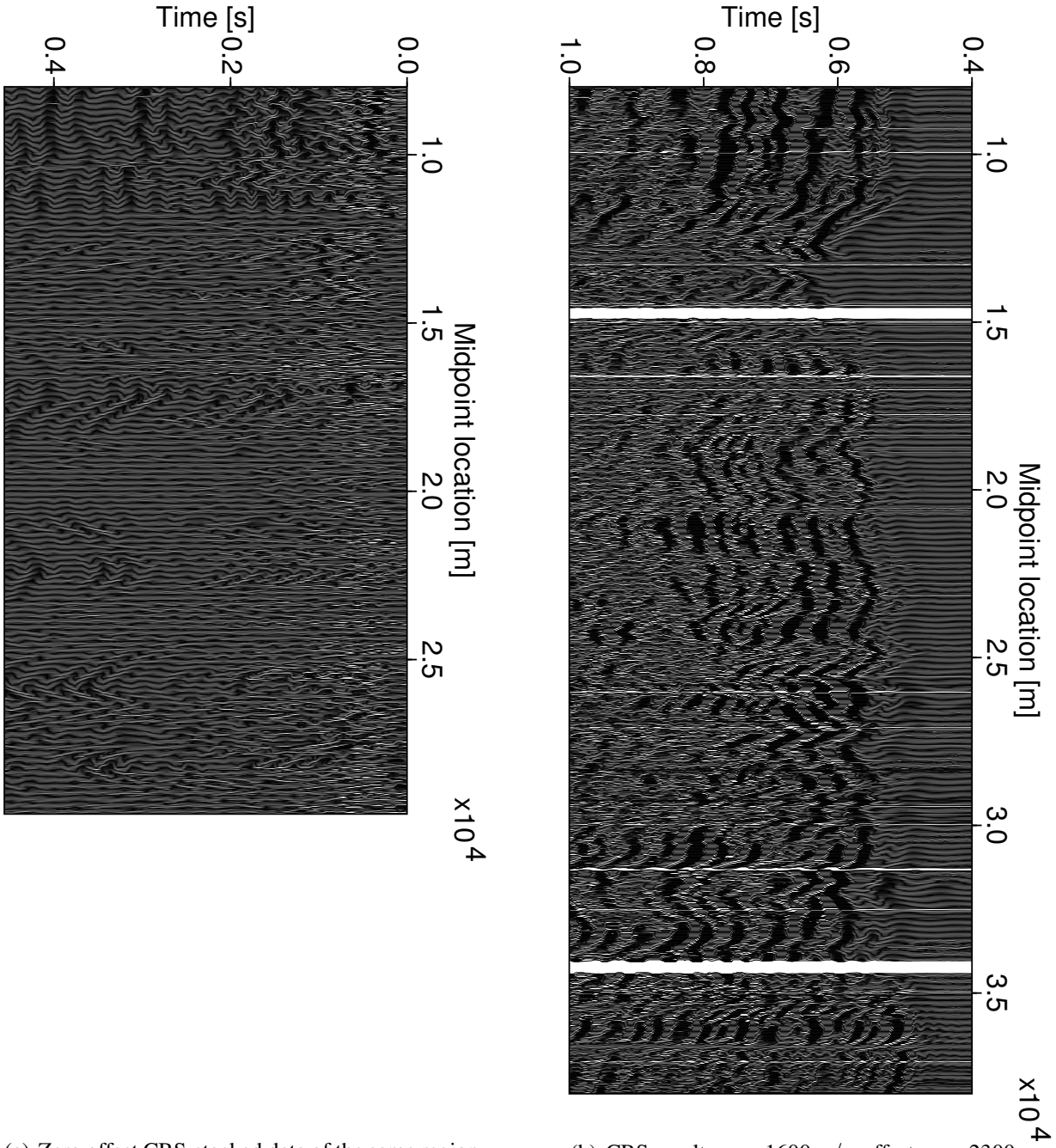

(a) Zero offset CRS-stacked data of the same region.

(b) CRS result, $v_S = 1600\,\mathrm{m/s}$, offsets $\approx -2300\,\mathrm{m}$.

Figure 5.4: *Surface seismic for topography - ZO CRS-stacked vs. CO CRS-stacked traces.*

5.2 CRS stack as a kinematic filter

In the previous section I suggested that choosing a more accurate calibration velocity would have benefited the final subsurface image. In this part I want to provide a short explanation for that assertion based on the concept of filters. As it is commonly known, a filter serves as a discriminator against some of the information entering it. The criteria for this attenuation are a manifold, e.g., frequency, amplitude, apparent velocity. But also coherence is a possible criteria.
From the above definition the whole CRS-based approach can be considered a high-resolution *hybrid filter* which incorporates coherence, moveout, and velocity discrimination, simultaneously. However, the velocity-calibration—yielding a similar effect as a τ-p filter—was never enforced insistently. This is because of the stacking parameters being able to partially compensate an incorrect near-surface velocity in every CRS operator. An effect being widely promoted as a benefit of the method under the catchphrase "independence of a macrovelocity model". It can be considered a benefit in situations where velocities cannot be reconstructed, e.g., surveys going back decades. For more recent field data geological probing will regularly exist along a whole profile and good estimates should be available.

The CO CRS search and stack is very attractive to serve as a filter operation because virtually any source-receiver pair can be synthesized from the input data as long as its coordinates fall within the survey. In this way, provided enough computational capacity is available, an whole new set of prestack data can be generated:

- Despite the velocity-calibration removing the independence of a macrovelocity model for the near-surface region the method remains to be data-driven and high-resolution because it works sample-wise.
- Attenuation of undesired shearwaves and the *groundroll cone* for near-offset traces is simplified. The ranges of possible moveout-surfaces are conveniently controlled by setting limits to the quintet of CRS attributes, i.e., angles and curvatures. I consider this ranging through calibration *more physical* than the specification of stacking velocities.
- Data can furthermore be regularized, removing gaps or establishing an equidistant spacing for shot and receiver points.

An illustration of some advantages gained through the knowledge of the near-surface velocity model is provided in Figure 5.5. The vertical component of a common-receiver gather extracted from the VSP field data of example **B** at a shallow level (≈ 900 ft) is displayed in Figure 5.5(a). The central region of the image is contaminated by groundroll and shearwave energy in such a way that a coherence analysis with respect to P-waves would produce unreliable results. Consequently, a wavefield decomposition for this gather towards a radial orientation (see, Figure 5.5(b))

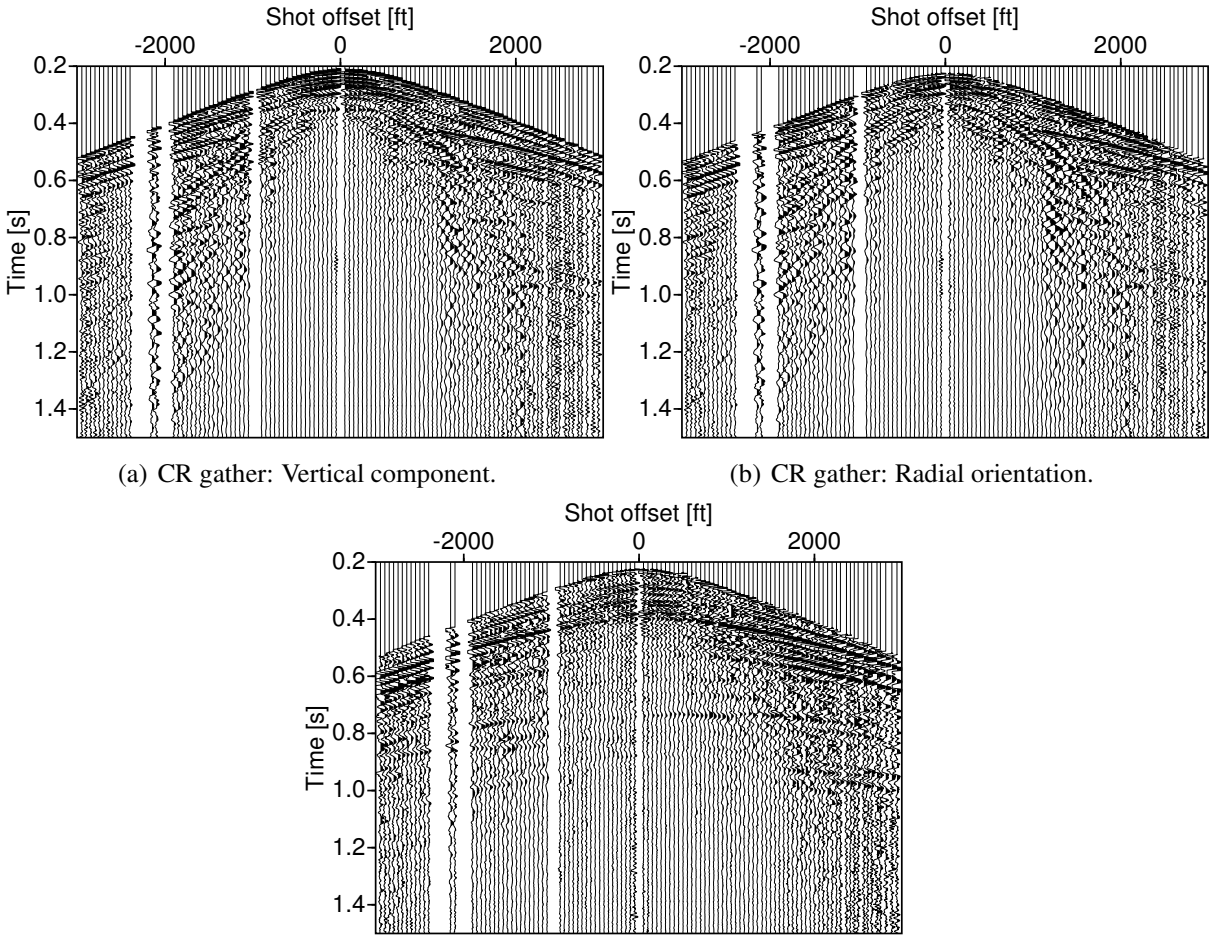

(a) CR gather: Vertical component.

(b) CR gather: Radial orientation.

(c) CR gather: from stacked CS gathers.

Figure 5.5: *Using CO CRS stacking as a kinematic filter.*

produces only minor improvements.

Once a whole common-receiver gather has been synthesized as it can be observed in Figure 5.5(c)—as a result of a common-shot search within the CO CRS workflow—the contamination has been attenuated on large scale. A subsequent common-receiver search performed in this newly created gather will provide a much more reliable set of stacking parameters.

5.3 Multicomponent data: Out-of-plane indicator

As it can be seen in example **A** the assumption of planar wave propagation can hardly be maintained for 3D heterogeneous models of the subsurface. For such a case a 2D acquisition is hardly qualified to produce a consistant imaging result. However, if three-component data is involved in an acquisition along a 2D profile, it becomes much easier to estimate the reliability of an event to be at the correct position.

In a similar way to the positioning of reflection events in time and depth, a wavefield decomposition suffers from inaccuracies, as soon a central ray leaves the global plane of acquisition. The present CO CRS-based approach makes no exception to this because the principal horizontal component of each recorded trace is rotated towards its respective source, designating it the *principal* component H_1. Its counterpart-component H_2 is *discarded*. As a consequence some reflection energy will always be lost for events occurring out-of-plane. It will remain missing during the rotation towards a particular orientation causing over- or undercorrection, even if a highly accurate emergence angle $\beta_G^{P/S}$ was used.

An entrance towards a possible solution, can be observed in Figure 5.6. The underlying prestack data was taken from example **A** and stems from the NS-walkover line based on acoustic raytracing. An initial common-shot search and stack was performed for the vertical component with the stacking result producing a common-receiver gather as shown in top figure with two reflections being recovered as expected. Then, the very same stacking operators within identical apertures were applied to both the principal and discarded horizontal component yielding two more sets of stacked traces (see, Figures 5.6(b) and 5.6(c)).
This stacking procedure provides a good estimate of the average residual energy present on both horizontal components as the misfit will be based on the vertical component. In this way, the energy which is collected for the H_2 component serves as an indicator for out-of-plane wave propagation. For a more qualitative measurement it now will be possible to recover the azimuth angle by employing a hodogram analysis. Yet, in the present case it proved sufficient to directly derive the azimuth angle from the relationship $\tan\theta_G = \mathrm{f}^{H_2}/\mathrm{f}^{H_1}$.

Figure 5.7(a) contains all the azimuth angles extracted for the example common-receiver gather introduced in Figure 5.6. Due to the nature of the tangens function, the range of distinct values is restricted to stay within $\pm 90^\circ$ with negative values being measured with respect to the negative part of the x_1-axis in the local Cartesian coordinate system. A polarity analysis working on a complete seismic wavelet would indicate the specific quadrant of the x_1x_2-plane in which an event was registered. This aspect, however, will be of no further concern.
As it was already expected from the results which I presented towards the end of example **A**, most central rays are significantly "out-of-plane" for this data. A final raytracing aiming at the

location of all reflection points in the depth-model is provided in Figure 5.7(b). The right-hand-side plot allows to follow the respective alignment of reflection points for distinct receiver levels of the walkover line quite well. If one connects the position of the well to such a collection of reflection points the expected azimuth angle can be measured with little effort. Even the S-shaped alignment across the second interface can be detected to a satisfying degree.

Concluding, one can say that any improvement of the CO CRS-based wavefield decomposition has to include a re-orientation of the principal horizontal component utilizing the recovered azimuth angle *prior* to any rotation towards radial or transverse orientation. Thus, a substantial amount of reflected energy which otherwise would have been lost can be recovered. The newly derived azimuth section itself can additionally serve as a supporting criteria for locating events in stacked images which were mispositioned due to a projection error.

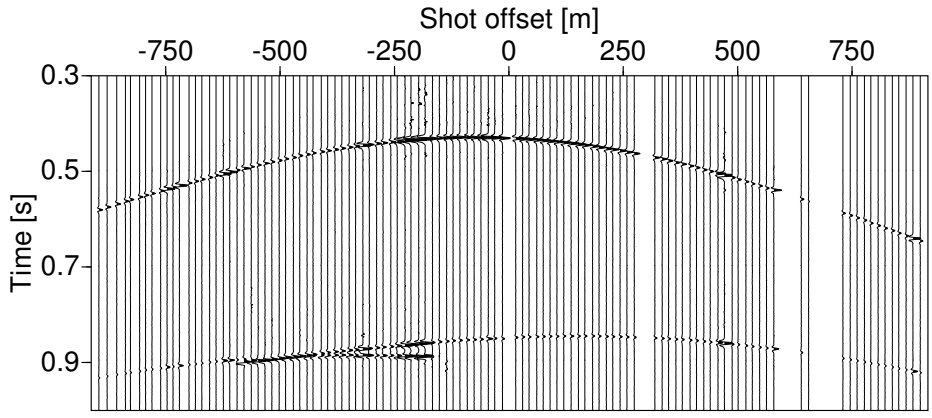

(a) Vertical component.

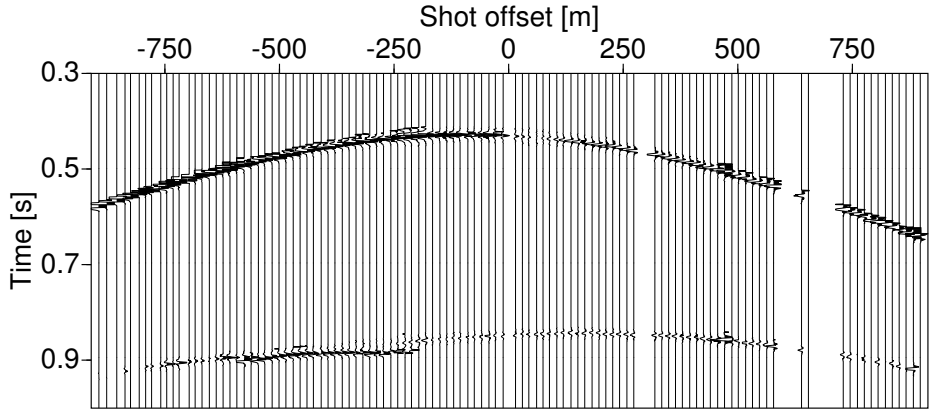

(b) Principal horizontal component H_1.

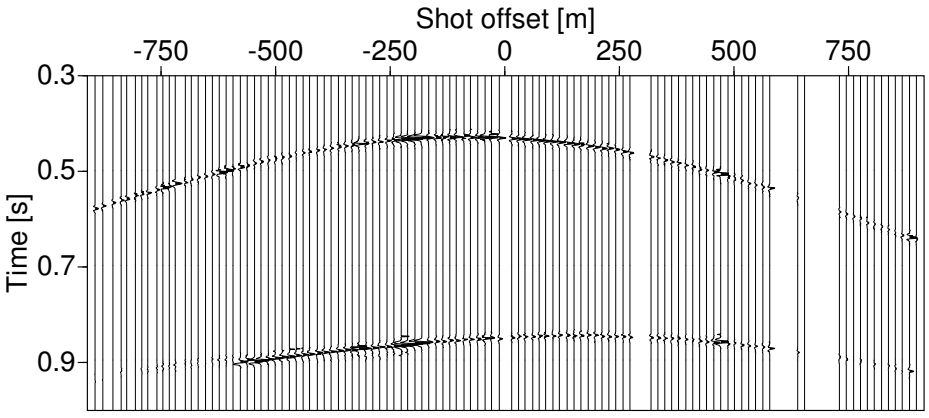

(c) Discarded horizontal component H_2.

Figure 5.6: *Stacking results of multicomponent CS gathers. The CO CRS attributes which are underlying the stacked traces from Figure 5.6(a) have been also applied to both horizontal components. Note, that the clip for the latter results was lowered and samples of low coherence were suppressed.*

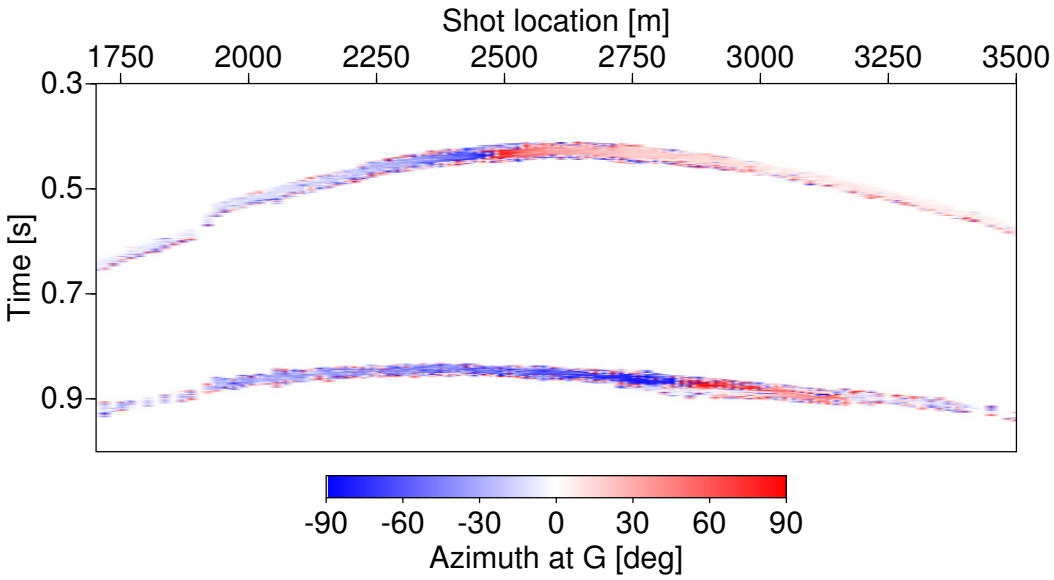

(a) Extracted azimuth angles from stacked inline and crossline horizontal component (see, Figures 5.6(b) and 5.6(c)).

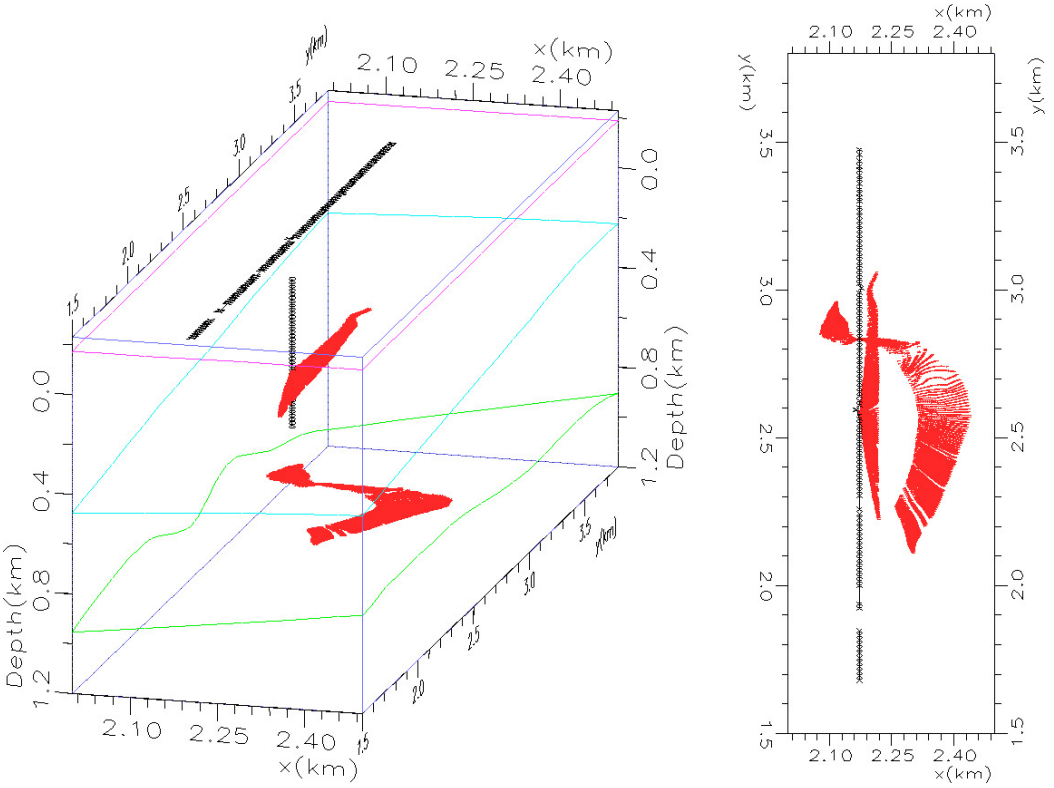

(b) Acoustic raytracing of reflection points in depth.

Figure 5.7: *Comparison of recovered azimuth angles and actual raypaths.*

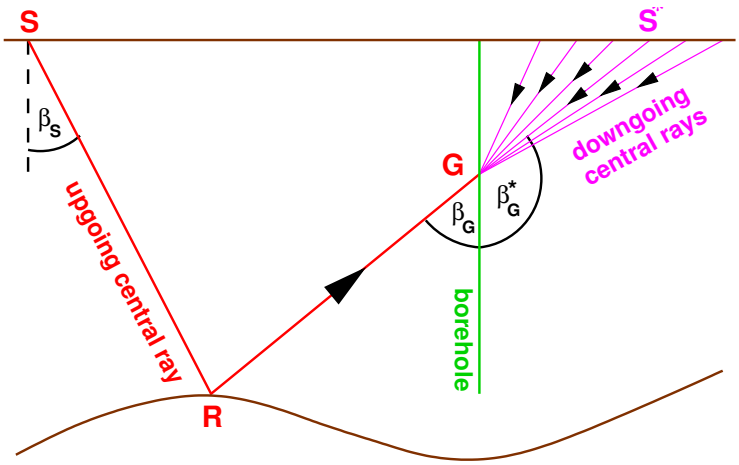

Figure 5.8: *For each upgoing reflection event detected by the CO CRS for VSP imaging the corresponding downgoing event from the opposite side of the walkover line is sought. The position of the newly constructed raypath SRGS* and its corrected traveltime are mapped to a trace which resembles a recording by a surface seismic survey.*

5.4 Mapping VSP data to surface seismic data

Raytracing is commonly used to perform a correction of near-offset VSP data to normal incidence time (see, Wyatt and Wyatt (1984)). The underlying velocity-depth model for this raytracing is estimated from known geology of the area, well-logs, previously acquired surface seismic in the area, or traveltime inversion of the VSP first-break arrivals. Usually, resolution of such a model will not be optimum to fit to the frequency content and geometry of VSP data subsequently yielding a flawed NMO correction.
There exists an alternative semblance-based approach to perform an NMO correction directly on 3D VSP walkaway data introduced by Gulati et al. (1997). It requires the reflection events to be corrected to a respective normal incidence time through a combination with the downgoing arrivals. For a heterogeneous velocity model, however, I expect this method to suffer from inaccuracies.

The simulation of surface seismic data from VSP data with the help of the CO CRS stack takes a similar course as the latter, but it is intended for complete walkover lines, only. Upon returning to example **A** one can observe the emergence angles for all direct arrivals at every receiver level being determined through semblance analysis in Figure 4.4. By the choice of an appropriate calibration velocity for all levels in the well, smoothly varying curves along the common-receiver configuration were produced (see section 4.1.2 for details). No further knowledge about medium properties *between* sources and receivers was required for this task. Upon exchanging the posi-

tions of sources and receivers—indicating a reverse-VSP survey—the emergence angles $\beta_G^\star$ can be considered as the take-off directions for meeting the virtual geophones placed on the surface at $S^\star$. The right side of Figure 5.4 illustrates this situation. As long as I can neglect anisotropy and severe inhomogeneities with respect to downgoing and upgoing events the calibration velocity for both types of events can remain equal. Analogously an arbitrary set of CO CRS stacked reflection events can be produced with the stacking parameter β_G being available alongside of

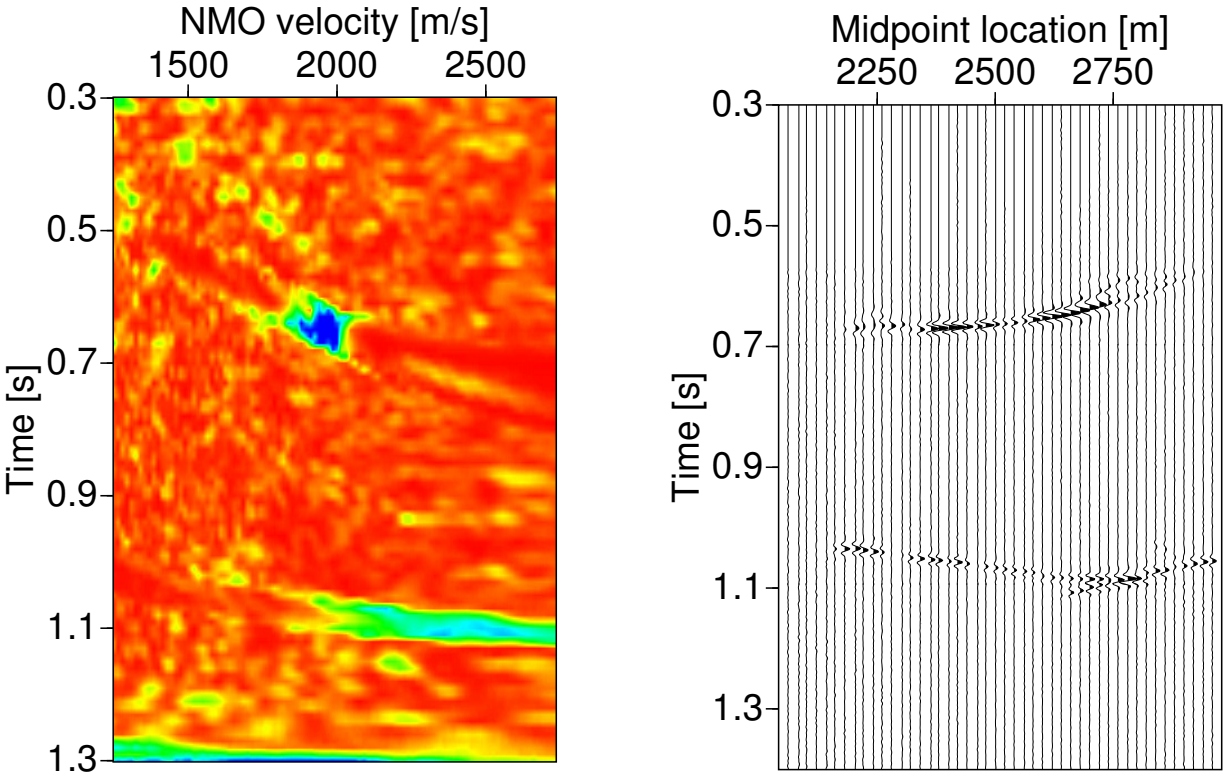

(a) Velocity analysis for synthesized CMP gather at $x = 2820\,\text{m}$.

(b) NMO-correction and subsequent stacking yields a ZO section.

Figure 5.9: *Conventional processing of remapped data: Velocity analysis, NMO-correction, and stacking is performed on data from example* **A**. *A zero-offset time-domain image is subsequently obtained.*

it. By combining reflection events and direct arrivals originating from opposite sides of the walkover line, I can convert G to be a transition point for a virtual surface seismic reflection with the raypath $\overline{SRGS^\star}$. In more particular detail, equation $\beta_G + \beta_G^\star = 180^\circ$ will be compared for all direct arrivals at a respective receiver level until at least one qualifying ray has been matched to the reflected ray under consideration. The reflection event's traveltime will be corrected by the first-break time of the qualifier, and the receiver position will be moved to $S^\star$. In a future implementation such a mapping should consider whole seismic wavelets during event detection and

a incorporate a certain Gaussian "smear" to distribute the reflected energy more evenly across neighboring traces.

As for now, a preliminary test on synthetic data from example **A** was performed for one constant receiver level of intermediately stacked data produced by the CS search already displayed in Figure 5.6(a). A set of surface seismic data was generated utilizing the above algorithm and then a binning to CMP gathers was performed. An subsequent investigation on the remapped data showed that it is even possible to perform conventional velocity analysis, NMO correction, and stacking yielding the results shown in Figure 5.9. The NMO-stacked image displayed in Figure 5.9(b) bears considerable similarities to the depth migration result from Figure 4.12(a). The encouraging first impressions gained by this study suggest, moreover, that an application of the 2D ZO CRS imaging workflow would be feasible on such a data. With this option at hand, a macro velocity model based of NIP tomography, specifically tuned to the frequency content of VSP data, can be generated. Consequently, PreSDM of the original walkover VSP data or PostSDM based on CO CRS stacked traces will become even more reliable and consistant.

Chapter 6

Conclusions and outlook

In the presented thesis I was able to establish a general data-oriented time domain imaging sequence which can serve various purposes. The theoretical considerations which were carried out are based on zero-order ray theory and paraxial ray tracing. The imaging sequence utilizes a general CRS operator derived from a even more general traveltime expression. One particular benefit of the newly introduced method is the flexibility in which it can handle virtually any type of survey geometry of present seismic acquisition. Analytic travetime surfaces described in this way follow a bistatic experiment — describing a common offset — and impinge interfaces in depth under non-normal angles of incidence. In this way not only reflection points but also conversion points can be imaged providing the investigated seismic data included considerable amounts of such energy.
Multicomponent seismic data which is conventionally supplied as a triplet of traces measuring towards each direction of Cartesian space is an ideal candidate for the CRS-based approach of imaging. Once a calibration of the stacking parameters by actual velocities for the vicinity of the source and receiver-side has been performed it becomes possible to decompose the data into separate wavemodes. These new data can subsequently be processed independently of each other yielding additional imaging results which can become very relevant for fluid detection and reservoir characterization.

An initial prototype for the above-mentioned processing scheme was developed under the limitation of planar wave propagation. From a computer scientific point of view I have to deal with a multidimensional optimization problem for five unknown parameters. The semblance criteria for normalized seismic time-series was chosen as the means to qualify a best-fitting traveltime operator. During my work emphasis was placed on the fast and stable determination of the associated stacking parameters by splitting up the CRS operator in three different search-domains and also by increasing the order of approximation. At first, the assumption of a locally plane wave is used

to determine the slowness related linear terms corresponding to angles of emergence at central source and receiver pair. Secondly, this assumption is dropped and a quadratic term is added into consideration which provides me with a second derivative of traveltime. Finally, I can perform a local optimization of the quintet of stacking parameters for the sake of increasing their accuracy. This solution to the problem can be regarded a very pragmatic and even drastic approach. Nevertheless coherence maxima proved to be located fairly easy in this manner.
Up to this point the imaging is carried out entirely in the time domain and may result in a set of stacked traces which are not fit for geological interpretation. As a final step it is recommended to perform a poststack depth migration of the results which is a commonplace process in the conventional seismic imaging toolbox.

The advantages of the CRS poststack strategy over conventional imaging centered in the prestack domain were pointed out and demonstrated in three data examples. Even though data acquired by VSP measurements can generally be regarded to be of very low fold at the receiver-side and therefore not very suited for data-driven strategies, I was able to show that the new strategy is performing well even under these circumstances. The results based on synthetic data in example **A** remained consistent with the underlying velocity-depth models after an external depth migration was performed. In the case of the field data shown in example **B**, it is hard to estimate how well the obtained results resemble the true subsurface structure. The conventional prestack depth migration which was carried out alongside of the CRS imaging showed reduced image quality especially for the target region. Accordingly, the wavefield decomposition into PP and PS events performed quite well and gave rise to more than double the amount of extracted information from both of the data. All of these highly satisfactory results lead me to the conclusion that the method will be a powerful addition to the available processing algorithms.

Synthetic example **C** remains in my thesis for the sole purpose of verifying the approach to be working for the case of a deviated well and was not carried out all the way to a depth image. This task has been accomplished to a satisfying extent. Another lesson learned from this investigation is that synthetic depth-velocity models for the VSP case should not contain “hard” boundaries intersecting the receiver levels since this leads to kinks in the traveltime data. Thus, synthetic seismograms should be generated based on smoothly varying, inhomogeneous velocity models.

In chapter 5 a couple of promising directions of future research have been compiled which I supported by preliminary processing results and illustrations. Most of them should require comparably little effort towards a final verification:

- A short excursion back to surface seismic field data disturbed by strong topography and a very inhomogeneous weathering layer shows promising preliminary results. Comparing these to conventional results of the same data found in literature I also suggest a more throughout investigation being pointed into this direction.

- The newly investigated field of wellbore seismic measurements in combination with the CRS methodology provides a multitude of open issues to attend to. The redatuming of VSP data in order to simulate surface seismic data is only one of them.
- Data regularization and filtering using the common offset CRS operator is another subject which should be observed with great detail. Removal of undesired shearwave or ground roll energy from prestack data by just using realistic near-surface velocities and search boundaries is a great benefit in support of conventional processing schemes.

Concerning the use of CRS attributes for complimentary tasks in seismic imaging apart from stacking and wavefield decomposition, I suggest to introduce them once more as an input for inversion algorithms. In his master's thesis Klüver (2004) showed that the attributes obtained by the common offset CRS stack can support the determination of smooth macro velocity models. The method he proposed is still waiting for an accurate approximation of the so-called *common-reflection-point* trajectory to be found in order to work as a stand-alone. Nevertheless, there should be no hindrance to supply already established inversion algorithms, e.g., *stereotomography* (Billette and Lambaré, 1998) with input of high resolution and quality instead of solely relying on picks from the prestack data itself.

The final challenge for the future will be the successful implementation of a 3D common offset CRS operator. A possible way to do so is to choose one of the 3D traveltime approximations I derived in chapter 3 as a first object of study which require comparably few stacking parameters to be determined simultaneously. The outlined search-strategy for the 2D case can be maintained and combined with the strategy for 3D ZO CRS imaging (see Bergler, 2004, for a comprehensive treatment). Once satisfying results in form of a case study have been achieved one can move towards the general operator (A.1) and will have to face less difficulties. Concluding, I hope my thesis will serve as one stepping stone in the right direction towards the completion of this task.

Appendix A

Examples for promising CRS operators

A.1 Common offset CRS operator for 3D wave propagation

Let me consider the two-point eikonal equation (2.96) for general coordinates in its parabolic expansion. By neglecting all components of the linear velocity gradient at the respective source and receiver positions as they appear in matrices $\mathsf{M}^{(y)}(G,S)$ and $\mathsf{M}^{(y)}(S,G)$ (see, expression (2.92)) and by introducing the sign-convention according to section 3.2 a very general traveltime operator can be derived which is composed of a multitude of terms. After applying a factorization it can be stated in a more transparent way which reads

$$\begin{aligned} T(G',S') = T_{\mathrm{CR}} &+ \frac{(\Delta x_G \cos\theta_G + \Delta y_G \sin\theta_G)\sin\beta_G - \Delta z_G \cos\beta_G}{v_G} \\ &+ \frac{(\Delta x_S \cos\theta_S + \Delta y_S \sin\theta_S)\sin\beta_S - \Delta z_S \cos\beta_S}{v_S} \\ &+ \frac{1}{2}\left(\mathtt{A}_G^2 \mathsf{M}_{11}^{(y)}(G,S) + 2\,\mathtt{A}_G \mathtt{B}_G \mathsf{M}_{12}^{(y)}(G,S) + \mathtt{B}_G^2 \mathsf{M}_{22}^{(y)}(G,S)\right) \\ &+ \frac{1}{2}\left(\mathtt{A}_S^2 \mathsf{M}_{11}^{(y)}(S,G) - 2\,\mathtt{A}_S \mathtt{B}_S \mathsf{M}_{12}^{(y)}(S,G) + \mathtt{B}_S^2 \mathsf{M}_{22}^{(y)}(S,G)\right) \\ &+ \mathtt{A}_G \mathtt{A}_S \mathsf{Q}_{2_{11}}^{-1} + \mathtt{B}_G \mathtt{A}_S \mathsf{Q}_{2_{12}}^{-1} - \mathtt{A}_G \mathtt{B}_S \mathsf{Q}_{2_{21}}^{-1} - \mathtt{B}_G \mathtt{B}_S \mathsf{Q}_{2_{22}}^{-1}, \end{aligned} \tag{A.1}$$

using the substitutes

$$\begin{aligned} \mathtt{A}_G &= (\Delta x_G \cos\theta_G + \Delta y_G \sin\theta_G)\cos\beta_G + \Delta z_G \sin\beta_G, \\ \mathtt{B}_G &= \Delta x_G \sin\theta_G - \Delta y_G \cos\theta_G, \\ \mathtt{A}_S &= (\Delta x_S \cos\theta_S + \Delta y_S \sin\theta_S)\cos\beta_S + \Delta z_S \sin\beta_S, \\ \mathtt{B}_S &= \Delta x_S \sin\theta_S - \Delta y_S \cos\theta_S. \end{aligned} \tag{A.2}$$

A.2 CO CRS operator for 2D using the vertical velocity gradient at G

For an arbitrary measurement configuration assuming planar wave propagation and the vertical velocity gradient at the receiver side to be explicitely known I obtain a similar traveltime operator as shown in equation (3.6) with five CRS attributes serving as coefficients:

$$\begin{aligned} T(G',S') &= T_{\mathrm{CR}} + \frac{\mathtt{D}_G}{v_G}\left(1 - \frac{1}{2\,v_G}\,\mathtt{D}_G\,\frac{\partial v_G}{\partial y_3}\right) + \frac{\Delta x_S \sin\beta_S}{v_S} - \frac{\Delta z_S \cos\beta_S}{v_S} \\ &\quad + \frac{1}{2}\,\mathtt{C}_G^2\,\mathtt{M}_{11}^{(y)}(G,S) + \frac{1}{2}\,\mathtt{C}_S^2\,\mathtt{M}_{11}^{(y)}(S,G) + \mathtt{C}_G\,\mathtt{C}_S\,\mathtt{Q}_{2_{11}}^{-1}\,. \end{aligned} \tag{A.3}$$

Again, for the sake of clarity three particular substitutes have been selected which read

$$\begin{gathered} \mathtt{C}_G = \Delta x_G \cos\beta_G + \Delta z_G \sin\beta_G\,, \quad \text{and} \quad \mathtt{D}_G = \Delta x_G \sin\beta_G - \Delta z_G \cos\beta_G\,, \\ \text{and} \quad \mathtt{C}_S = \Delta x_S \cos\beta_S + \Delta z_S \sin\beta_S\,. \end{gathered} \tag{A.4}$$

Deviating from showing the hyperbolic expansion as done in earlier sections I am here preserving the initial parabolic form as it involves no additional computational challenge to alter it and the paraxial slowness vectors are derived much easier in this way. I expect this operator to be promising and fruitfully from a research-related viewpoint as the velocity gradient in the borehole is easily accessible. Reflection events which were recorded in complicated settings — with reference to Example **C** — should fit much better to this type of analytic traveltime surfaces, therefore improve not only imaging results but also the attribute-based wavefield separation.

Appendix B

An alternative CO CRS processing strategy

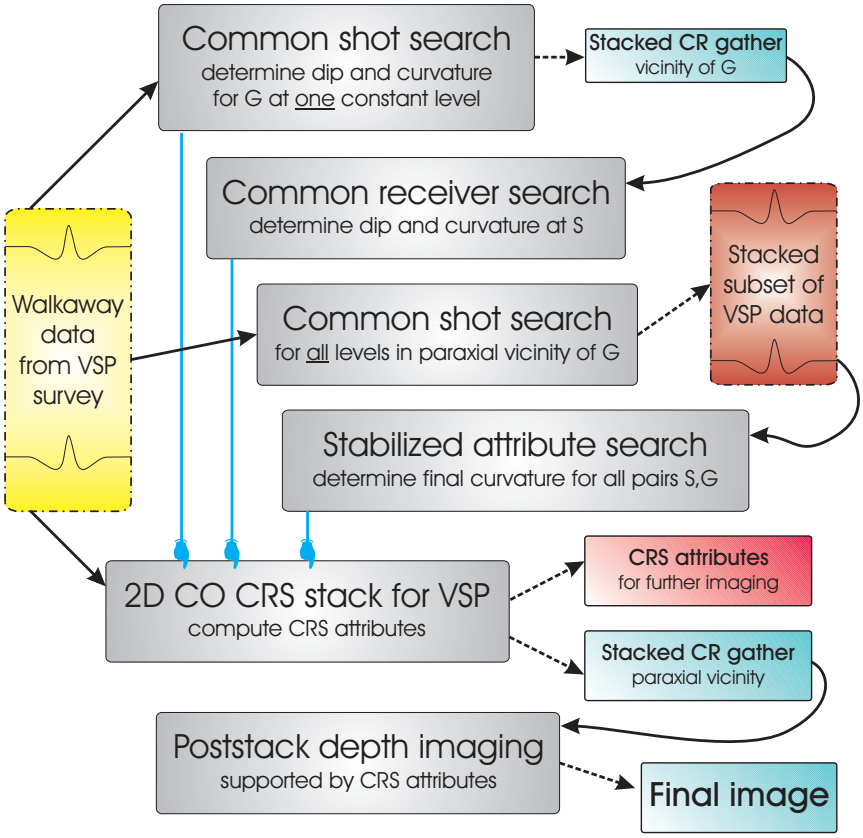

Figure B: *Improved CO CRS processing workflow.*

The processing workflow displayed in Figure B serves as an alternative to the established scheme which was introduced in chapter 3. I already pointed out that for the case of VSP data, the quasi-

CO configuration is recommended to be used to combine shot and receiver positions during the coherence analysis. But, while the resulting set of traces will provide an optimum illumination which covers an extensive part of each reflector, the area which lies close and shallow to the borehole is not imaged at all. For the future I expect the application of the CO CRS method to be oriented towards the investigation of several offsets for the same data set. The previously-mentioned disadvantage can be overcome by a redesign in the following manner.

Choosing the imaged traces to form a synthesized common-receiver gather as hinted in Figure B lets the original two composite searches remain mostly unaltered. The CR search simplifies in a way that it can be performed with the intermediately stacked traces produced by the CS search. A fifth stacking parameter still needs to be determined from a third configuration which has to be provided beforehand. In an additional step being introduced into the workflow several neighboring CR gathers with respect to the initial gather are synthesized. This is an analog treatment as for the CS search. The result will be a *kinematically*, i.e., CRS-filtered, set of prestack data (see, section 5.2). The enhanced S/N ratio and quality of such data will yield the missing stacking parameter in a final coherence analysis working on CRS supergathers. The CO CRS stack and PostSDM will be in accordance with Workflow 3.3.

Appendix C

Description of used hard- and software

1. - Coding and testing of CRS stack software:

- ANSI C++ using GNU compiler (GNU-license)
- Eclipse - programming environment (GNU-license)

2. - Processing of the data examples:

- CRS stack-based and related software (WIT Consortium)
- Seismic Unix v. 39.0 - package (Colorado School of Mines)
- ProMAX - processing environment (Landmark)
- Kirchhoff prestack depth migration - (P/GSI)

3. - Visualization of the data examples:

- Seismic Unix v. 39.0 - package (Colorado School of Mines)
- Gnuplot v. 4.0 - plotting utility (GNU-license)

4. - Thesis was generated using:

- Latex - package (GNU-license)

- Kile v. 1.9.3 - editor for Latex (GNU-license)
- CorelDraw v. 9.0 - graphics suite (Corel)

5. - Coding, testing, and processing carried out on:

- AMD Athlon XP with 1800+ CPU a.k.a. GPI_CRS5 - Suse Linux 9.0
- Intel Pentium 4 with 2800 MHz CPU a.k.a. GPI_LS1 - Suse Linux 9.0
- AMD Dual Opteron system a.k.a. GPI_LS3 - Suse Linux 9.0
- Intel Mobile Pentium 4 with 1400 MHz CPU a.k.a. SCHNICKSCHNACK - Suse Linux 10.0

List of Figures

Chapter 1 – Introduction **1**

1.1 Illustration of Kirchhoff depth migration 3

1.2 Motivation for the acquisition of VSP data 4

1.3 Multicomponent data: First impression 6

1.4 Multicomponent data: Hodogram analysis 6

1.5 First glimpse at seismic data from a VSP survey 6

Chapter 2 – Theory **9**

2.1 Taylor expansion of paraxial traveltimes 25

2.2 Local ray-centered Cartesian coordinate system 27

2.3 General Cartesian coordinate system 32

Chapter 3 – Implementation **35**

3.1 Sign convention for slowness vectors 37

3.2 Projection and local approximation by a parabolic shape 40

3.3 Sketch of 2D VSP acquisition geometry 44

3.4 Instrumented CRS processing workflow for qCO 45

3.5 Imaging spaces for VSP data 49
3.6 Schematic of wavefield separation 51
3.7 Wavefield separation based on CRS attributes 52

Chapter 4 – A: Synthetic seismic data—straight vertical well **55**

4.1 Survey map 56
4.2 Velocity models sliced along two directions 57
4.3 Depth-velocity curves 59
4.4 Emergence angles - contour plots 60
4.5 Model-derived vs. calibrated emergence angles 60
4.6 Result: Wavefield decomposition of NS line 61
4.7 Geometry map 63
4.8 Result: qCO stacked traces for PP reflections 66
4.9 Result: quintet of CRS attributes for PP reflections 67
4.10 Result: qCO stacked traces for PS reflections 68
4.11 Result: qCO versus qCMP domain imaging 69
4.12 Result: Kirchhoff depth migration of the NS-line 71
4.13 Contradiction to a central assumption 71
4.14 CS gather: V/H raw 72

Chapter 4 – B: Real field data—straight vertical well **72**

4.15 Checkshot velocities 74
4.16 CS gather: V/H preprocessed 75
4.17 Result: CS gather: R/T orientation 75
4.18 Result: PP CS/CR stack 77

4.19 Result: PP/PS CRS stack 78

4.20 Result: CS gather: β_G extrapolated 79

4.21 Result: PP CRS attribute 79

4.22 Result: VSP real data - post-CRS-stack depth migration 80

4.23 Result: VSP real data - prestack depth migration 80

Chapter 4 – C: Synthetic seismic data—deviated well **81**

4.24 Depth model and survey geometry 82

4.25 Sample CR gather of the data 83

4.26 Two sample CS gathers of the data 84

4.27 Geometry maps 85

4.28 Result: qCO stacked traces for PP reflections 87

4.29 Depth-velocity curves used for calibration 88

4.30 Result: number CRS-stacked traces 88

Chapter 5 – Surface seismics revisited **89**

5.1 Comparison of stacked CS gathers - positive offset 93

5.2 Comparison of stacked CS gathers - negative offset 94

5.3 Comparison of CO CRS stack vs. raw data 95

5.4 Comparison of CO CRS stack vs. ZO CRS stack for topography 96

Chapter 5 – CRS stack as a kinematic filter **97**

5.5 Using CO CRS stacking as a kinematic filter 98

Chapter 5 – Multicomponent data: Out-of-plane indicator **99**

5.6 Stacking results on multicomponent data 101

5.7 Comparison of recovered azimuth angles and actual raypaths 102

5.8 Illustration: Combining up- and downgoing rays 103

Chapter 5 – Mapping VSP data to surface seismic data **103**

5.9 Conventional processing of remapped data 104

Appendix **113**

B Improved CO CRS processing workflow 113

Bibliography

Aki, K. and Richards, P. G. (1980). *Quantitative Seismology – Theory and Methods*, volume 1. W. H. Freeman & Co.

Bergler, S. (2004). *On the determination and use of kinematic wavefield attributes for 3D seismic imaging*. Logos Verlag.

Bergler, S., Duveneck, E., Höcht, G., Zhang, Y., and Hubral, P. (2002a). Common-Reflection-Surface stack for converted waves. *Stud. Geophys. Geod.*, 46:165–175.

Bergler, S., Mann, J., Höcht, G., and Hubral, P. (2002b). The Finite-Offset CRS stack: an alternative stacking tool for subsalt imaging. In *Annual Meeting Abstracts*, pages 2058–2061, Session: SP 1.8. Soc. Expl. Geophys.

Billette, F. and Lambaré, G. (1998). Velocity macromodel estimation from seismic reflection data using stereotomography. *Geophys. J. Int.*, 135:671–690.

Biondi, B. L. (2007). *Concepts and applications in 3D seismic imaging*, volume No. 10 of *Distinguished Instructor Series*. Soc. Expl. Geophys.

Bleistein, N. (1984). *Mathematical methods for wave phenomena*. Academic Press Inc.

Boelsen, T. (2005). The Common-Reflection-Surface Stack for arbitrary acquisition geometries and multi-component data – Theory and Application. Master's thesis, Karlsruhe University, http://www.wit-consortium.de/Downloads.

Boelsen, T. and Mann, J. (2005). 2D CO CRS stack for multi-component seismic reflection data. In *Extended Abstracts*. 67th Annual Internat. Mtg., Eur. Assn. Geosci. Eng. Session: P063.

Bortfeld, R. (1989). Geometrical ray theory: Rays and traveltimes in seismic systems (second-order approximations of the traveltime). *Geophysics*, 48(3):1342–349.

Bullen, K. E. and Bolt, B. (1985). *An introduction to the theory of seismology*. Cambridge Univ. Press.

Červený, V. (2001). *Seismic Ray Theory*. Cambridge Univ. Press.

Červený, V., Klimeš, L., and Pšenčík, I. (1984). Paraxial ray approximation in the computation of seismic wavefields in inhomogeneous media. *Geophys. J. R. astr. Soc.*, 79:89–104.

Chapman, C. (2004). *Fundamentals of seismic wave propagation*. Cambridge Univ. Press.

Chira, P. and Hubral, P. (2003). Traveltime formulas of near-zero-offset primary reflections for curved 2D measurement surface. *Geophysics*, 68(1):255–261.

DiSiena, J. P., Gaiser, J. E., and Corrigan, D. (1984). Horizontal components and shear wave analysis of three-component VSP data. In Toksöz, N. and Stewart, R., editors, *Vertical Seismic Profiling, Part B-Advanced Concepts*, pages 177–188. Geophys. Press, London.

Doherty, F. (2004). How 3D VSP has become a practical proposition. *First Break*, 22(5):63–67.

Duveneck, E. (2004). Velocity model estimation with data-derived wavefront attributes. *Geophysics*, 69(1):265–274.

Farra, V. (1999). Computation of second-order traveltime perturbation by Hamiltonian ray theory. *Geophys. J. Int.*, 136:205–217.

Frehers, S., Gierse, G., Thiessen, J., and Weber, U. (2007). Sparse 3D acquisition - Simulation and optimisation by the CRS technique. In *Annual Meeting Abstracts*, pages 2605–2609, Session: SPNA 1.7. Soc. Expl. Geophys.

Gilbert, F. and Backus, G. E. (1966). Propagator matrices in elastic wave and vibration problems. *Geophysics*, 31(2):326–332.

Gulati, J. S., Stewart, R. R., Peron, J. F., and Parkin, J. M. (1997). 3C-3D VSP: Normal moveout correction and VSPCDP transformation. In *CREWES Research Report*, page Chp. 7. University of Calgary.

Hardage, B. A. (1983). *Vertical Seismic Profiling, Part A: Priciples*. Geophys. Press, London.

Hertweck, T., Schleicher, J., and Mann, J. (2007). Data stacking beyond CMP. *The Leading Edge*, 26(7):818–827.

Herzberger, M. (1958). *Modern Geometrical Optics*. Interscience.

Hinds, R. C., Anderson, N. L., and Kuzmiski, R. D. (1996). *VSP interpretive processing: Theory and practice*, volume No. 3 of *Open File Publications*. Soc. Expl. Geophys.

Höcht, G., de Bazelaire, E., Majer, P., and Hubral, P. (1999). Seismics and optics: hyperbolae and curvatures. *Journal of Applied Geophysics*, 42(3,4):261–281.

Höcht, G. and Ricarte, P. (2006). Parameter-oriented CRS imaging. In *Annual Meeting Abstracts*, pages 2966–2970, Session: ST 1.2. Soc. Expl. Geophys.

Hubral, P. (1979). A wave front curvature approach to computing ray amplitudes in inhomogeneous media with curved interfaces. *Stud. Geophys. Geod.*, 23:131–137.

Hubral, P. and Krey, T. (1980). *Interval velocities from seismic reflection traveltime measurements*. Soc. Expl. Geophys.

Ikelle, L. T. and Amundsen, L. (2005). *Introduction to petroleum seismology*, volume No. 12 of *Investigations in Geophysics*. Soc. Expl. Geophys.

Jäger, R. (1999). The Common-Reflection-Surface stack – Theory and application. Master's thesis, Karlsruhe University, http://www.wit-consortium.de/Downloads.

Keydar, S., Gelchinsky, B., and Berkovitch, A. (1996). Common shot-point stacking and imaging method. *Journal of Seismic Exploration*, 5:261–274.

Klüver, T. (2004). Seismic traveltime inversion using finite-offset kinematic wavefield attributes. Master's thesis, Karlsruhe University, http://www.wit-consortium.de/Downloads.

Klüver, T. (2007). *Velocity model building using analytic and model-based diffraction traveltime functions*. PhD thesis, Karlsruhe University, http://www.wit-consortium.de/Downloads.

Mann, J. (2002). *Extensions and applications of the Common-Reflection-Surface stack method*. Logos Verlag.

Müller, A. (2007). *Determination of interval velocities by inversion of kinematic 3D wavefield attributes*. PhD thesis, Karlsruhe University, http://www.wit-consortium.de/Downloads.

Müller, T. (1999). *The Common-Reflection-Surface stack method - Seismic imaging without explicit knowledge of the velocity model*. Der andere Verlag.

Popov, M. and Pšenčík, I. (1978). Computation of ray amplitudes in inhomogeneous media with curved interfaces. *Stud. Geophys. Geod.*, 22:248–258.

Schleicher, J., Tygel, M., and Hubral, P. (2007). *Seismic true-amplitude imaging*, volume No. 12 of *Geophysical Developments*. Soc. Expl. Geophys.

Taner, M. T. and Koehler, F. (1969). Velocity spectra - digital computer derivation and applications of velocity functions. *Geophysics*, 34(6):859–881.

Ursin, B. (1982). Quadratic wavefront and traveltime approximations in inhomogeneous layered media with curved interfaces. *Geophysics*, 47(7):1012–1021.

von Steht, M. (2004). The Common-Reflection-Surface Stack under Consideration of the Acquisition Surface Topography – Combined Approach and Data Examples. Master's thesis, Karlsruhe University, http://www.wit-consortium.de/Downloads.

von Steht, M. and Goertz, A. (2007). Imaging walkaway VSP data using the common-reflection-surface stack. *The Leading Edge*, 26(6):764–768.

Wyatt, K. D. and Wyatt, S. B. (1984). Determining subsurface structure using the vertical seismic profile. In Toksöz, N. and Stewart, R., editors, *Vertical Seismic Profiling, Part B: Advanced Concepts*, pages 148–176. Geophys. Press, London.

Yang, K., Wang, H. Z., and Ma, Z. T. (2005). An output imaging scheme of common-reflection-surface stack. *Journal of Seismic Exploration*, 14:131–154.

Zhang, Y. (2003). *Common-Reflection-Surface Stack and the Handling of Top Surface Topography*. Logos Verlag.

Zhang, Y. and Wu, R.-S. (2004). CRS stack and redatuming for rugged surface topography: A synthetic data example. In *Annual Meeting Abstracts*, pages 2040–2043, Session: SP 4.6. Soc. Expl. Geophys.

Acknowledgments

There are several different people and institutions which I would like to recognize for contributing to and influencing the course of the presented thesis:

- **Prof. Dr. Hubral**: thank you very much for allowing me to pursue my degree by accepting the supervision of my thesis, — despite well-deserved retirement claims. He granted me a huge amount of scientific leeway and an was an encouraging mentor throughout my studies.
- **Prof. Dr. Gajewski**: kind regards, for taking up the job as a co-supervisor of my thesis and for his constructive comments during various meetings.
- **Paulsson Geophysical Services Inc.**: for offering and funding a short-term visit to their premises in Brea, CA. Learning some essential details about the professional processing of VSP data provided a solid foundation for many aspects covered in my thesis. I also acknowledge their permission to use images from the Weyburn survey for my introduction.
- **Vaquero Energy**: for providing the VSP field data presented as example **B** in chapter 4.
- **Saudi Aramco**: for kindly letting me present their surface seismic field data displayed in chapter 5.
- the **German Federal Ministry of Education and Research (BMBF)**: for financial support through my involvement in the project "CO2CRS" focusing on the development of new technologies in support of the carbon capture and storage (CCS) approach (`www.geotechnologien.de`).
- **Baker Hughes Inc.**: for allowing me to display their illustrations for educational purposes as shown in chapter 1 (provided by `www.vsfusion.com`).
- the members of the **Wave Inversion Technology Consortium** and its sponsors for their continuing support.

My personal gratitude extends especially to the following people:

- **Dr. Alex Goertz** not only for his outstanding support during my visit to Brea and the mentoring while working on our joint article but also for the many fruitful discussions we had on the subject of VSP imaging. His personal assistance and interest kept me motivated throughout the time I spent on this subject. I hope we can uphold this friendly exchange for many years to come.
- **Dr. Jürgen Mann** is credited for his tireless commitment towards the allocation of funding to conduct our academic research. I also consider him an authority in many fields of applied geophysics and thank him for always being helpful in providing his scientific advice. Kind regards also for the valuable discussions on the matters of general physics during the preparations of my defense, his proof-reading, and for him introducing me to the "depth imaging community" through countless anecdotes and personal acquaintances.
- **Tim Boelsen** put tremendous work into his master's thesis from which my research inherited many ideas. I believe that he deserves a lot of credit for advancing the matter of coupling multicomponent data with CRS imaging into an close-to-feasible state. Hopefully, we can share a joint-publication in the future.
- **Dr. Yonghai Zhang and Dr. Steffen Bergler** with their work contributed significantly to the theoretical aspects, on which my studies were based on.
- **Dr. Miroslav Brajanovski** generously shared with me his philosophical, social, and scientific views while spending his time as researcher in Karlsruhe. I would like to thank him for his *excellent* friendship and for keeping me in good spirits.
- **Claudia Payne**: for her cheerful and optimistic attitude and her professional way of dealing with organizational problems.
- **Miriam, Alex, Tilman, Fabian, Beate, and last but not least Nico**: for being friendly colleagues and never refusing to offer advice or help by any means. I really enjoyed the conversations we had during lunch or coffee breaks and the extracurricular activities I shared with you guys.

... AND THE FINAL CREDITS ARE DEDICATED TO MY SWEETHEART HEIKE, MY PARENTS, GRANDPARENTS, AND FRIENDS AS ...

> Affection is responsible for nine-tenths of whatever solid and durable happiness there is in our lives.
>
> (C.S. Lewis - British scolar and novelist, 1898-1963)